



**FEASIBILITY ANALYSIS OF A COMPTON SPECTROMETER SYSTEM  
FOR IDENTIFICATION OF SPECIAL NUCLEAR MATERIAL**

THESIS

Chad C. Schools, Major, USA

AFIT/GNE/ENP/05-12

**DEPARTMENT OF THE AIR FORCE  
AIR UNIVERSITY**

**AIR FORCE INSTITUTE OF TECHNOLOGY**

**Wright-Patterson Air Force Base, Ohio**

APPROVED FOR PUBLIC RELEASE; DISTRIBUTION UNLIMITED

The views expressed in this thesis are those of the author and do not reflect the official policy or position of the United States Air Force, Department of Defense, or the U.S. Government.

AFIT/GNE/ENP/05-12

**FEASIBILITY ANALYSIS OF A COMPTON SPECTROMETER SYSTEM FOR  
IDENTIFICATION OF SPECIAL NUCLEAR MATERIAL**

THESIS

Presented to the Faculty

Department of Engineering Physics

Graduate School of Engineering and Management

Air Force Institute of Technology

Air University

Air Education and Training Command

In Partial Fulfillment of the Requirements for the

Degree of Master of Science (Nuclear Science)

Chad C. Schools, MS  
Major, USA

March 2005

APPROVED FOR PUBLIC RELEASE; DISTRIBUTION UNLIMITED

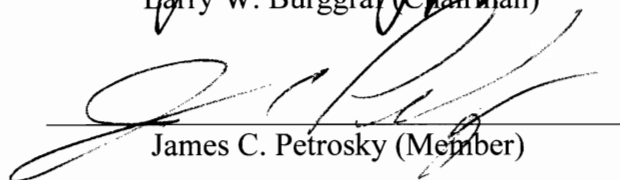
**FEASIBILITY ANALYSIS OF A COMPTON SPECTROMETER SYSTEM FOR  
IDENTIFICATION OF SPECIAL NUCLEAR MATERIAL**

Chad C. Schools, MS  
Major, USA

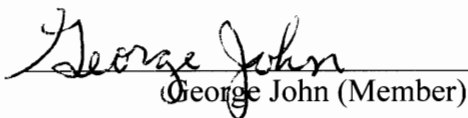
Approved:

  
Larry W. Burggraf (Chairman)

9 Mar '05  
Date

  
James C. Petrosky (Member)

9 Mar 2005  
Date

  
George John (Member)

9 March 2005  
Date

### **Abstract**

Current operational needs require the deployment of radiation detection equipment with the ability to accurately and reliably identify special nuclear materials and their byproducts without dependence on cryogenics. This requires a resolution of 0.5% or less over a range of 200 to 700 keV. The feasibility of a Compton spectrometer to achieve this resolution is examined.

The Compton spectrometer system used consists of two detectors. The Compton scatter event occurs in a CdTe detector where the Compton electron energy is collected. Gamma rays scattered out of the CdTe at an angle determined by a conical collimator, are collected in a NaI(Tl) detector. Coincidence electronics determine correlated events and allow the Compton electron and scattered gamma ray energy spectra to be collected.

Experimental and modeling techniques are used to evaluate the system's resolution and efficiency and provided reasonable agreement. Expected experimental results based on previous work were not reproduced and the source of the difference remains unknown. Results suggested strict requirements of collimation will make some low areal count rate applications impossible.

### **Acknowledgments**

I would like to thank Dr. Larry Burggraf, my thesis advisor and golf idol, for his support and mentorship throughout this project. I have truly enjoyed our long discussions in the laboratory about the intricacies of radiation detection and measurement and have learned a tremendous amount from his vast knowledge and experience. I would also like to thank Dr. George John and Dr. James Petrosky, my committee members, for being there for support and guidance throughout this project.

I also want to thank the individuals that helped pull the equipment and materials together to make this project possible. Eric Taylor's constant support throughout this research was instrumental in the assembly of electronics and detectors. The work horses of the AFIT Model Shop; Condi Inman, Russell Hastings and Jan LeValley, provided a professional service backed with impressive skills and knowledge that was called upon many times to create the components that held the detection system together.

Finally, I cannot express enough appreciation of my wife's unwavering support which has been crucial to my completion of this thesis and master's degree program as it has been throughout my military career.

Chad C. Schools

## Table of Contents

	Page
Abstract.....	iv
Acknowledgments.....	v
List of Figures .....	ix
List of Tables .....	xiv
I. Introduction .....	1
Background.....	1
Problem Statement.....	2
Scope .....	5
Investigative Questions .....	5
Order of Presentation.....	5
II. Theory .....	7
Chapter Overview.....	7
Fundamentals of Nuclear Physics and Radiation Detection.....	7
Photons Interactions with Matter .....	7
Attenuation and Probability of Interaction .....	12
Detector Response to Gamma Radiation .....	13
Detector Response Complications .....	17
Detector Resolution and Efficiency .....	18
Signal-to-Noise Ratio and Minimum Detectable Activity.....	23
The Compton Spectrometer.....	24
III. Equipment.....	29
Chapter Overview.....	29
Compton Spectrometer System .....	29
Detectors.....	30
Electron Energy Analyzer.....	30
Photon Energy Analyzer .....	33
Coincidence Electronics .....	34
Collimators .....	37
Radioactive Sources .....	37
IV. Methodology.....	39

Chapter Overview.....	39
Detector Testing and Characterization .....	39
System Housing Construction .....	42
Timing Pulse Alignment and Coincidence Method Evaluation .....	44
Compton Spectrometer Data Collection.....	45
Compton Spectrometer Simulation Code.....	46
V. Data Analysis and Results.....	49
Chapter Overview.....	49
CdTe Characterization.....	49
NaI(Tl) Characterization .....	58
Compton System Geometry Effects .....	60
Coincidence Electronics Evaluation.....	65
Experimental Compton Spectrometer Energy Spectra.....	70
Simulated Compton Spectrometer Energy Spectra .....	73
VI. Conclusions and Recommendations .....	82
Conclusions of Research .....	82
Recommendations for Action.....	83
Recommendations for Future Research.....	84
Appendix A: $^{239}\text{Pu}$ and $^{240}\text{Pu}$ Spectra.....	85
Appendix B: Summary of Previous Experimental Findings.....	88
Appendix C: Klein-Nishina Approximation Evaluation.....	91
Appendix D: Compton Relation Calculations .....	94
Appendix E: CdTe Detector Systems and Supporting Electronics.....	98
Appendix F: Attenuation Calculations.....	100
Appendix G: NaI(Tl) Detector and Supporting Electronics .....	101
Appendix H: Coincidence Electronics.....	102
Appendix I: Initial Collimator .....	104
Appendix J: Conical Collimator .....	105
Appendix K: Radioactive Sources .....	108



Appendix L: Sample Calculation of Activity Adjustment for Current Date .....	109
Appendix M: Simulated System Computer Code.....	111
Appendix N: CdTe Spectra.....	124
Appendix O: NaI(Tl) Spectra.....	126
Appendix P: CdTe Detector Diagram.....	128
Bibliography .....	130

## List of Figures

Figure	Page
1. Energy spectrum for $^{239}\text{Pu}$ showing 639 and 645 keV peaks of interest and the complicated spectrum requiring high resolution (INEE, 1999).....	4
2. Energy spectrum for $^{240}\text{Pu}$ showing 642 keV peak of interest (INEE, 1999).....	4
3. Relative importance of the three major types of gamma ray interactions based on photon energy and atomic number (Knoll, 2000:52).....	8
4. Compton scatter diagram; incident photon scattered at angle $\theta$ , Compton electron scattered at angle $\phi$ (Knoll, 2000:51).....	9
5. Polar plot of Klein-Nishina formula representing the probability of the incident gamma ray, of initial energy shown, scattering at an angle $\theta$ .....	11
6. Probability of gamma ray interaction between depths $x_1$ and $x_2$ expressed as the difference of attenuation at $x_1$ and $x_2$ .....	13
7. Various gamma ray interactions affecting detector response .....	15
8. Calculated Compton continuum and edge for a 662 keV photon in CdTe (full-energy peak not shown).....	16
9. Example of source-detector geometry effects on detector response.....	17
10. Example energy spectrum for full-width at half-maximum and full-width at tenth-maximum resolution calculations .....	18
11. Figure of Merit describes the ability of a detector to distinguish two energy peaks (Knoll, 2000: 680).....	21
12. Parallel planar detector-source geometry for calculation of solid angle subtended by detector from source (Tsoulfanidis,1995: 269).....	22
13. The Compton spectrometer consisting of the electron energy analyzer (EEA) and the photon energy analyzer (PEA).....	25
14. Demonstration of the partial-energy Compton electron spectrum collected in the EEA converted to the calculated full-energy gamma ray spectrum based on Compton relation; Improved resolution from 0.96% to 0.52% .....	27

15. Compton spectrometer configuration; 1. Isotropic sample, 2. Initial linear collimator, 3. EEA (CdTe detector), 4. Conical collimator, 5. PEA (NaI(Tl) detector) .....	30
16. CdTe hermetic detector housing (Amptek, 2002: 20) .....	31
17. PX2T Shaping Amplifier output with RTD inactive (Amptek, 2002: 21) .....	32
18. Energy spectrum with and without RTD active demonstrating the reduction in hole tailing (Amptek, 2002: 21).....	33
19. Amplitude walk, rise-time walk and jitter effects on pulse discrimination (Knoll, 2002: 659-661). .....	35
20. CdTe resolution and efficiency geometry .....	40
21. Sample $^{57}\text{Co}$ spectrum using CdTe detector (RTD on, Position 1) .....	40
22. Sample $^{57}\text{Co}$ spectrum using CdTe detector (RTD on, Position 2) .....	40
23. Modified PX2T for external power supply.....	41
24. NaI(Tl) resolution and efficiency geometry .....	42
25. Sample $^{137}\text{Cs}$ spectrum using NaI(Tl) detector in characterization geometry .....	42
26. Compton spectrometer housing .....	43
27. CdTe resolution vs. gamma ray energy .....	51
28. CdTe absolute peak efficiency plot, source-detector geometry shown in Figure 20 ..	53
29. CdTe peak intrinsic efficiency plot, source-detector geometry shown in Figure 20 ..	54
30. Inverse high voltage bias versus FWHM plot.....	56
31. Estimate of the FWHM contributions for the Amptek CdTe detector.....	57
32. NaI(Tl) FWHM versus gamma ray energy .....	59
33. Diagram of initial circular collimator and solid angle subtended by CdTe detector ..	61
34. Source distribution on CdTe 1 mm x 5 mm face from Position 2; white pixels represent largest distribution; black pixels represent smallest distribution .....	62

35. Active volume of CdTe detector based on conical collimator geometry; larger circles represent a larger number of paths through the conical collimator gap with the largest occurring at the apex of the conical collimator .....	63
36. CdTe crystal location and RTD evaluation; count rate from RTD and ICR as a function of the source alignment with CdTe graduated scale.....	64
37. RTD/ICR Ratio; determination of active RTD on detector volume .....	65
38. Oscilloscope output-SCA logic pulse generated from EEA and PEA energy pulses.	66
39. Oscilloscope output-LGSC logic pulse created by coincident EEA and PEA timing pulses .....	67
40. Oscilloscope output-ADC delayed linear gate alignment with LGSC output .....	68
41. Delay curve-counts versus adjustable delay to determine optimized alignment .....	69
42. Oscilloscope output using TAC method; time between CdTe and NaI(Tl) determines TAC output pulse height .....	70
43. 10-Hour Compton spectrometer spectrum- <sup>137</sup> Cs source using pulse-overlap method	71
44. 10-Hour Compton spectrometer spectrum- <sup>137</sup> Cs source using start-stop method .....	71
45. 74-Hour Compton spectrometer spectrum- <sup>22</sup> Na source using start-stop method .....	72
46. 13 point smoothed 74-Hour Compton spectrometer spectrum- <sup>22</sup> Na source using start-stop method.....	72
47. Simulated Compton spectrometer spectrum - conical collimator gap=1.0 mm.....	75
48. Simulated Compton spectrometer spectrum - conical collimator gap=0.5 mm.....	75
49. Simulated Compton spectrometer spectrum - collimator radius=0.25 mm .....	75
50. Simulated Compton spectrometer spectrum - detector width=0.3 mm .....	75
51. Simulated Compton spectrometer spectrum - detector location=2.0 mm.....	76
52. Simulated Compton spectrometer spectrum - detector location=-1.0 mm .....	77
53. Simulated Compton spectrometer - detector location=-4.0 mm.....	77
54. Simulated 1-hour Compton system spectrum using combined <sup>137</sup> Cs source showing counts versus energy .....	78

55. Simulated 1-hour Compton system spectrum using 60 $\mu$ curie $^{22}\text{Na}$ source showing counts versus energy .....	79
56. Simulated 662 keV spectrum with required resolution.....	81
57. $^{239}\text{Pu}$ Energy spectrum 0-400 keV, (INEE,1999) .....	85
58. $^{239}\text{Pu}$ Energy spectrum, 400-800 keV (INEE,1999) .....	86
59. $^{240}\text{Pu}$ Energy spectrum, 0-800 keV (INEE,1999) .....	87
60. One-hour single collimator Compton spectrometer spectrum, channel width 0.050 $\pm$ 0.002 inch (Williams, 2003: 80) .....	88
61. Plot of average FWHM from 100 keV peak using Compton spectrometer (Williams, 2003: 85) .....	89
62. Simulated wgPu spectrum using Compton spectrometer (Williams, 2003: 96) .....	89
63. Simulated rgPu spectrum using Compton spectrometer (Williams, 2003: 96) .....	90
64. Comparison plot of Klein-Nishina formula, an empirical formula (Massaro and Matt, 1986: 545-547) and XMuDat (Nowotny, 1998).....	93
65. Photograph of XR-100T-CdTe detector with housing removed.....	99
66. Photograph of PX2T-CdTe power supply and shaping amplifier .....	99
67. Photograph of NaI(Tl) detector.....	101
68. NaI(Tl) in detector housing inside lead cave .....	102
69. Photograph of start-stop coincidence electronics .....	102
70. Photograph of pulse overlap coincidence electronics.....	103
71. Photograph of hexagonal cross section collimator .....	104
72. Photograph of circular cross section collimator.....	104
73. Photograph of conical collimator with alignment grid in center .....	105
74. Photograph of conical collimator without center cone .....	106
75. Photograph of conical collimator inside cone with alignment grid .....	107
76. Dimensions of conical collimator .....	107

77. Code Simulation geometry .....	112
78. Example of incremental source areas. Radius pixel set to 3 and angle pixel set to 8. ....	113
79. Example of incremental EEA volumes. 5x5x1 mm <sup>3</sup> with proportional pixel set to 1. ....	113
80. Example of incremental areas of bottom conical collimator gap. Radius pixel set to 3 and angle pixel set to 12. ....	113
81. Example geometry used to calculate Compton electron energies and Compton scatter probabilities. ....	113
82. Example output of simulation showing Compton electron energy versus probability spectrum. ....	114
83. Example output of simulation showing Compton electron energy versus counts spectrum. ....	116
84. <sup>57</sup> Co spectrum using CdTe detector (RTD off, Position 1, Figure 20) .....	124
85. <sup>57</sup> Co spectrum using CdTe detector (RTD off, Position 2) .....	124
86. <sup>57</sup> Co spectrum using CdTe detector (RTD on, Position 1) .....	124
87. <sup>57</sup> Co spectrum using CdTe detector (RTD on, Position 2) .....	124
88. <sup>57</sup> Co spectrum using CdTe detector provided by Amptek (Amptek, 2004: 25) .....	124
89. <sup>137</sup> Cs spectrum using CdTe detector (RTD off, Position 1) .....	124
90. <sup>137</sup> Cs spectrum using CdTe detector (RTD off, Position 2) .....	125
91. <sup>137</sup> Cs spectrum using CdTe detector (RTD on, Position 1) .....	125
92. <sup>137</sup> Cs spectrum using CdTe detector (RTD on, Position 2) .....	125
93. <sup>137</sup> Cs spectrum using CdTe detector provided by Amptek (Amptek, 2004: 28) .....	125
94. Multinuclide (T108) spectrum using NaI(Tl) detector .....	126
95. NaI(Tl) detector characterization spectrum; <sup>57</sup> Co .....	127
96. NaI(Tl) detector characterization spectrum; <sup>137</sup> Cs .....	127
97. Photograph of Compton spectrometer in situ .....	129

## List of Tables

Table	Page
1. Calculated and Experimental Values for Compton Cross-Section (Nowotny, 1998) .	12
2. CdTe FWHM Analysis Data.....	50
3. CdTe Absolute Peak Efficiency Data .....	52
4. CdTe Peak Intrinsic Efficiency Data .....	54
5. Calculated Fano Factors from Figure 30 .....	56
6. NaI(Tl) Resolution Data .....	58
7. NaI(Tl) Absolute Efficiency Data.....	60
8. NaI(Tl) Intrinsic Efficiency Data.....	60
9. Spectral data from Compton spectrometer (Williams, 2003: 81).....	88
10. Compton electron energy as a function of incident gamma ray energy and scatter gamma ray angle (in radians).....	94
11. Compton Electron FWHM vs. Incident Gamma Ray FWHM ( $\gamma=200$ keV) .....	95
12. Compton Electron FWHM vs. Incident Gamma Ray FWHM ( $\gamma=300$ keV) .....	95
13. Compton Electron FWHM vs. Incident Gamma Ray FWHM ( $\gamma=400$ keV) .....	96
14. Compton Electron FWHM vs. Incident Gamma Ray FWHM ( $\gamma=500$ keV) .....	96
15. Compton Electron FWHM vs. Incident Gamma Ray FWHM ( $\gamma=600$ keV) .....	97
16. Compton Electron FWHM vs. Incident Gamma Ray FWHM ( $\gamma=700$ keV) .....	97
17. List of CdTe components.....	98
18. List of NaI(Tl) components .....	101
19. Electronics used for start-stop coincidence technique .....	103
20. Electronics used for pulse overlap technique.....	103
21. Radioactive sources .....	108

# **FEASIBILITY ANALYSIS OF A COMPTON SPECTROMETER SYSTEM FOR IDENTIFICATION OF SPECIAL NUCLEAR MATERIAL**

## **I. Introduction**

The Department of Defense (DoD) has many activities, such as nuclear treaty and counter-proliferation monitoring, that require deployable, high-resolution radiation detection systems. The primary focus of this research is the development of a system capable of achieving high resolution over a wide range of energies that is not dependent on resource intensive liquid nitrogen. The system analyzed in this research is based on the previous work of Captain Williams on the development of a Compton spectrometer system. The benchmark used to evaluate the system's performance is the difficult task of determining the isotopic ratio of a plutonium source, as needed for treaty monitoring. This application can easily be extended to other DoD radiation detection needs requiring similar energy resolutions over a wide range of energies.

## **Background**

As the face of world politics continues to change, the requirements for improved nuclear counter-proliferation and treaty verification techniques increases. "Today, the most important threat to US security is the proliferation of weapons of mass destruction (WMD) to...countries like North Korea, Iran and Iraq as well as to non-state actions such as terrorist and organized criminals" (Hays,1998: 2). The accountability of existing special nuclear material (SNM) and the detection of nuclear technology development are critical to providing security to our nation and stability to the world. A portable detection



system capable of identifying the presence and the isotopic makeup of SNM is needed for both of these missions.

“On May 24, 2002, the United States and Russia signed the Treaty on Strategic Offensive Reductions (also known as the Moscow Treaty), establishing a limit of 1,700 to 2,200 warheads in each party’s deployed strategic nuclear arsenal by 2012” (Graham, 2003: 1453). The accountability of weapon systems in this process is critical as they are moved to storage or decommissioning facilities. With this overwhelming burden on accountability, a considerable amount of time may elapse before a missing weapon system is noticed. With the possibility of “spoof” weapons, replacing a weapon’s physics package with non-weapons grade material, the missing weapon may never be identified. The ability to determine the isotopic ratios of the material with a portable system would facilitate Strategic Arms Reduction Treaties (START I & II) inspections and treaty verification.

The clandestine nuclear weapon programs of countries like North Korea and Iran pose a serious threat to the world and a difficult challenge to the intelligence community. The development of un-accounted nuclear weapons and SNM cannot be tolerated. The detection of such activities can be determined from their radioactive byproducts. Again, deployable and dependable detection systems with high resolution are required.

### **Problem Statement**

The grade of a plutonium sample is difficult to determine because of the complicated gamma ray energy spectra of  $^{239}\text{Pu}$  to  $^{240}\text{Pu}$  which is further complicated by the effects of shielding. The grade of plutonium is classified by the isotopic ratio of  $^{239}\text{Pu}$

to  $^{240}\text{Pu}$ . Weapons grade plutonium is identified as having over 90%  $^{239}\text{Pu}$  and less than 7%  $^{240}\text{Pu}$  (DTRA, 2001: 120, 135). The high spontaneous fission rate of  $^{240}\text{Pu}$  is undesirable for use in weapons because it leads to early initiation and reduced yield or device failure. Reactor grade plutonium is identified as having 15-25%  $^{240}\text{Pu}$ . The complete energy spectra of  $^{240}\text{Pu}$  and  $^{239}\text{Pu}$  are found in Appendix A. Although there are many characteristic gamma rays of both isotopes, the 639.99 keV and 645.9 keV  $^{239}\text{Pu}$  peaks and the 642.35 keV  $^{240}\text{Pu}$  peak are used for illustration. The spectra of  $^{239}\text{Pu}$  and  $^{240}\text{Pu}$  around these energies are shown in Figure 1 and Figure 2, respectively. These energies are chosen for two primary reasons. The first is the higher probability of escape from the nuclear weapon casing. Second is the availability of peaks from both isotopes in a narrow energy range. This limits the energy-dependent effects of scattering and absorption (Williams, 2003: 5-6). The ability to distinguish these peaks requires a full-width at half-maximum (FWHM) of approximately 2 keV. Although this resolution can be achieved with high purity germanium detectors (HPGe), their dependence on liquid nitrogen (LN) for cooling makes them less practical for field use.

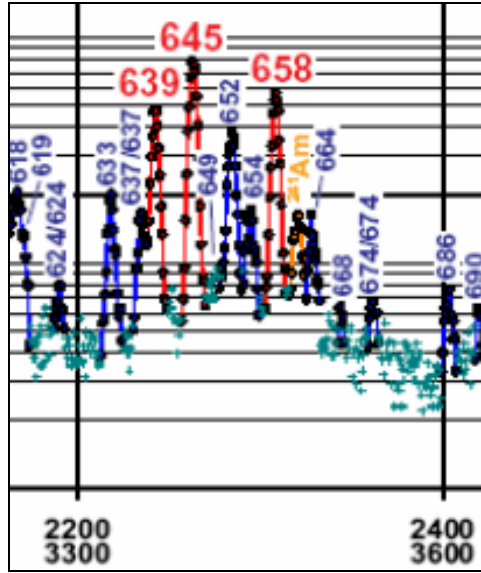


Figure 1. Energy spectrum for  $^{239}\text{Pu}$  showing 639 and 645 keV peaks of interest and the complicated spectrum requiring high resolution (INEE, 1999)

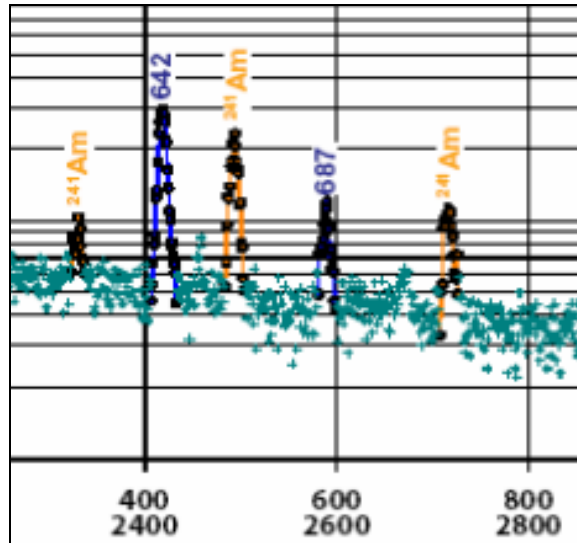


Figure 2. Energy spectrum for  $^{240}\text{Pu}$  showing 642 keV peak of interest (INEE, 1999)

## **Scope**

The goal of this research is to use the Compton spectrometer for plutonium isotopic ratio determination, continuing the work of Capt. Chris Williams in 2003. Capt. Williams determined that the Compton spectrometer showed the required resolution to separate the plutonium peaks of interest, see Appendix B. His research used an essentially mono-energetic  $^{137}\text{Cs}$  source.

The purpose of this research is to investigate the resolution and efficiency of the Compton spectrometer system over an energy range of 200-700 keV, with multi-energetic sources. The ultimate goal is to reconstruct an operational Compton spectrometer system, using the same detectors and collimators, with two major considerations in mind; the reproducibility of experimental geometry and the additional signal processing needed for multi-energetic sources. In addition to the experimental procedures, a simulation code was developed to evaluate experimental results and to assist with design modifications for follow on research.

## **Investigative Questions**

1. Can the previous results by Capt. Williams be reproduced?
2. How does the energy gating affect the Compton Spectrometer?
3. Can modeling the Compton spectrometer help with future design?

## **Order of Presentation**

The following chapters cover my research of the Compton spectrometer. Chapter II discusses the fundamental physics that makes the system possible and reviews some essential radiation detection measurement theory. The equipment used during this

research is described in Chapter III. Chapter IV covers the procedures used during this research. Chapter V presents the experimental and simulated results and analyses. The conclusions from the data analyses and recommendations for future research are covered in Chapter VI. Finally, Appendix A through P present detailed background information including tabulated data, computations, and diagrams.

## **II. Theory**

### **Chapter Overview**

The purpose of this chapter is to review the theory associated with this thesis. The chapter is divided into two sections. Section one covers the fundamental physics that make the Compton Spectrometer possible and some of the fundamentals of radiation detection. The topics include photon interactions with matter, detector response functions, detector resolution and efficiency, and attenuation. Section two covers the operation of the Compton Spectrometer and includes system configuration, advantages and disadvantages.

### **Fundamentals of Nuclear Physics and Radiation Detection**

#### **Photons Interactions with Matter**

There are many categories of photon interactions with matter. The three major interactions are photoelectric absorption, Compton scattering and pair production. As shown in Figure 3, which effect is most likely to occur can be generalized based on the energy of the incoming gamma ray and the atomic number ( $Z$ ) of the absorbing material. The line separating each region depicts the equal probability of the adjacent effects occurring. The photoelectric effect ( $\tau$ ) is dominant at low gamma ray energies and increases with higher  $Z$ . Compton scattering ( $\sigma$ ) is the dominant effect for low  $Z$  absorbers for a wide range on energies. Pair production ( $\kappa$ ) requires minimum gamma ray energy of 1.02 MeV and is not significant for energies below several MeV. This project deals with lower-energy photons, therefore pair production is not be discussed

further. Two detector materials used in this research, cadmium telluride (CdTe) and thallium doped sodium iodide (NaI(Tl)), have Zs of approximately 50 and 53 respectively. Figure 3 shows that for these materials the photoelectric effect and Compton effect are comparably efficient for gamma rays of 300 keV. Over the majority of the energy range of interest, 200-700 keV, the Compton effect is dominant.

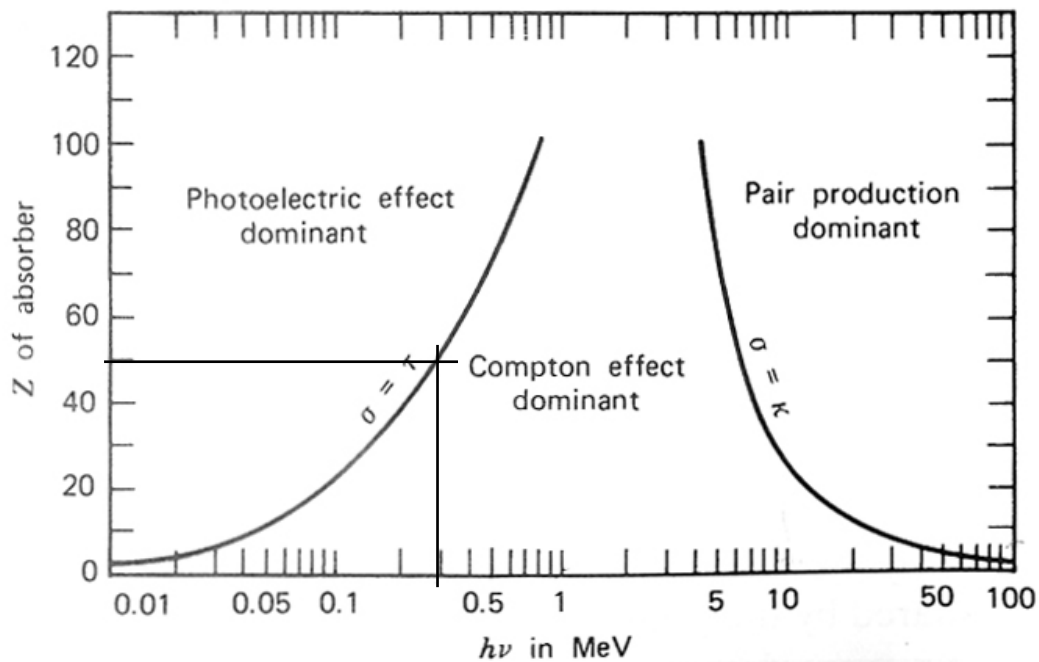


**Figure 3. Relative importance of the three major types of gamma ray interactions based on photon energy and atomic number (Knoll, 2000:52)**

### Photoelectric Effect

Photoelectric absorption is the process in which the incoming gamma ray is completely absorbed in an atom resulting in an electron being ejected. The photoelectron is isotropic and has the same energy of the incident gamma ray, less the binding energy

of the ejected electron. If there is sufficient energy, one of the tightly bound K-shell electrons can be liberated. Characteristic x-rays may then be emitted as outer shell electrons cascade down to fill lower shell vacancies. No simple formula for the probability of photoelectric absorption exists but can be generalized as  $\tau \propto Z^4/(h\nu)^3$ , where  $h\nu$  is the gamma ray energy (Turner, 1995:173).

### Compton Scattering

Compton scatter occurs when the incident gamma ray interacts with an electron in the absorbing material. As shown in Figure 4, the incident gamma ray of energy  $h\nu$  is scattered at an angle  $\theta$ , with a resulting energy of  $h\nu'$ , expressed as:

$$h\nu' = \frac{h\nu}{1 + \frac{h\nu}{m_0c^2}(1 - \cos\theta)} \quad (1)$$

where  $m_0c^2$  is the rest mass energy of the electron (511 keV) (Knoll, 2000:51).

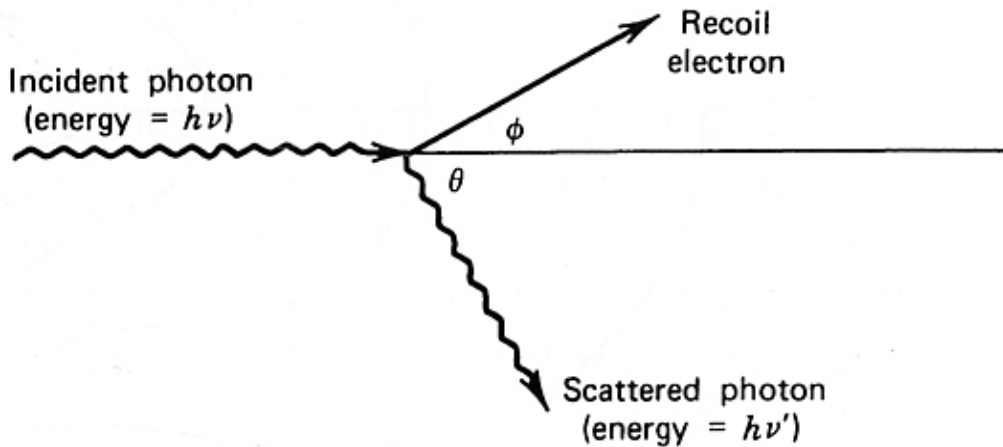


**Figure 4. Compton scatter diagram; incident photon scattered at angle  $\theta$ , Compton electron scattered at angle  $\phi$  (Knoll, 2000:51)**



The energy of the scattered electron, also known as the Compton electron, is equal to the incident gamma ray energy minus the scattered gamma ray energy and is given as (Turner, 1995:178):

$$T = h\nu \frac{1 - \cos \theta}{\frac{m_0 c^2}{h\nu} + 1 - \cos \theta} . \quad (2)$$

The Compton electron is scattered at an angle ( $\phi$ ) ranging from 0-90 degrees in the opposite direction from the scattered gamma ray in order to conserve momentum. The relation between  $\phi$  and  $\theta$  is given as (Turner, 1995: 178):

$$\tan \phi = \frac{\cot \frac{\theta}{2}}{1 + \frac{m_0 c^2}{h\nu}} . \quad (3)$$

The Klein-Nishina formula calculates the angular distribution of scattered gamma rays:

$$\frac{d\sigma}{d\Omega} = Zr_0^2 \left( \frac{1}{1 + \alpha(1 - \cos \theta)} \right)^2 \left( \frac{(1 - \cos^2 \theta)}{2} \right) \left( 1 + \frac{\alpha^2 (1 - \cos \theta)^2}{(1 + \cos^2 \theta)(1 + \alpha(1 - \cos \theta))} \right) \quad (4)$$

where  $\alpha = h\nu/m_0 c^2$  and  $r_0$  is the classical electron radius (Knoll, 2000:51). Figure 5 shows the Klein-Nishina formula plotted for varying incident gamma ray energies from 1 keV to 5 MeV. The higher-energy gamma rays clearly tend to forward scatter while very low-energy gamma rays have an equal probability of back scatter.

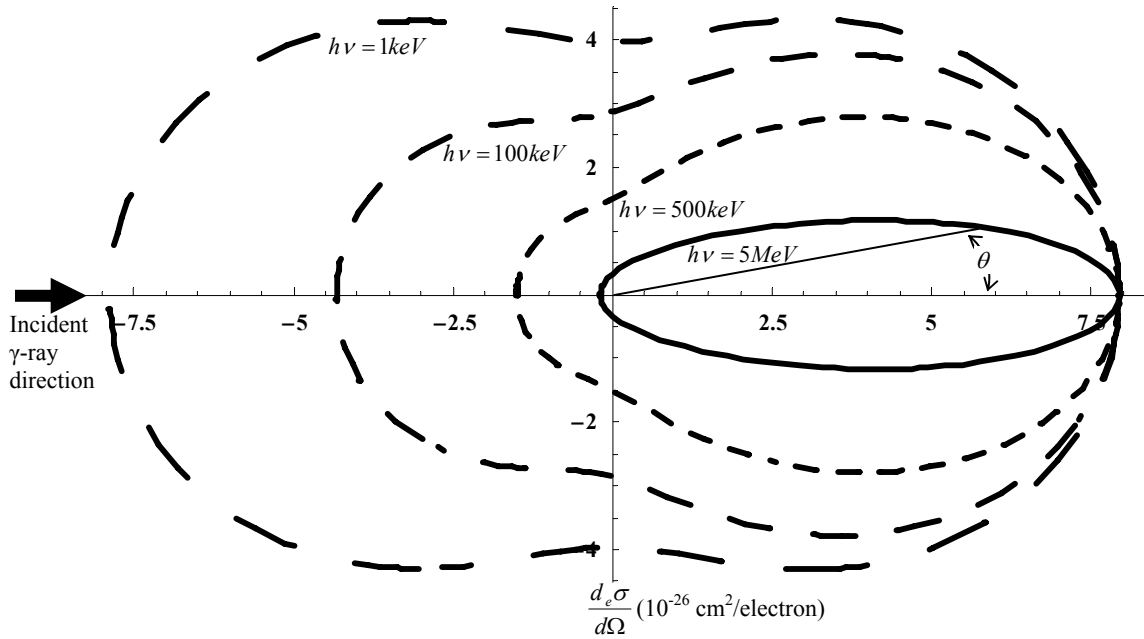


**Figure 5. Polar plot of Klein-Nishina formula representing the probability of the incident gamma ray, of initial energy shown, scattering at an angle  $\theta$**

Integrating the energy dependent Klein-Nishina formula over all solid angles gives the total Compton cross section. The formula assumes that the interaction is with free electrons and does not consider the bound state of the electrons. This assumption leads to larger Compton cross sections for lower-energy gamma rays. For CdTe, the relative error of the calculated value to experimental data range from 11.5% for 100 keV gamma rays to 1.1% for 700 keV gamma rays as shown in . The integration can also be conducted over a portion of the solid angle to determine the probability that the gamma ray will scatter into the solid angle of interest.

Table 1. Calculations are shown in Appendix C. The integration can also be conducted over a portion of the solid angle to determine the probability that the gamma ray will scatter into the solid angle of interest.

**Table 1. Calculated and Experimental Values for Compton Cross-Section (Nowotny, 1998)**

Incident $\gamma$ (keV)	Klein-Nishina (Centimeter <sup>2</sup> )	XMudat	Relative Error (%)
100	0.12360	0.11090	11.5
200	0.10200	0.09727	4.9
300	0.08868	0.08628	2.8
400	0.07946	0.07782	2.1
500	0.07256	0.07150	1.5
600	0.06712	0.06624	1.3
700	0.06268	0.06200	1.1

### Attenuation and Probability of Interaction

The attenuation of gamma rays can be expressed as a function of the linear attenuation coefficient ( $\mu$ ) and the thickness of absorber material ( $t$ ). The sum probabilities of the individual interaction processes gives  $\mu = \tau + \sigma + \kappa$ . Given an initial number of gamma rays emitted ( $I_0$ ) and a transmitted number of gamma rays ( $I$ ) the attenuation is expressed as (Tsoulfanidis, 1995: 159)

$$I = I_0 e^{-\mu t} . \quad (5)$$

The probability of an interaction occurring between the depths  $x_1$  and  $x_2$  as shown in Figure 6 can then be expressed as

$$P_{x_1-x_2} = \frac{I_{x_1} - I_{x_2}}{I_0} = e^{-\mu x_1} - e^{-\mu x_2}, \quad (6)$$

where  $I_{x_1}$  and  $I_{x_2}$  are the number of transmitted gamma rays at  $x_1$  and  $x_2$ , respectively.

To determine the probability of a Compton scatter occurring between  $x_1$  and  $x_2$ ,

Equation 6 is multiplied by  $\sigma/\mu$ .

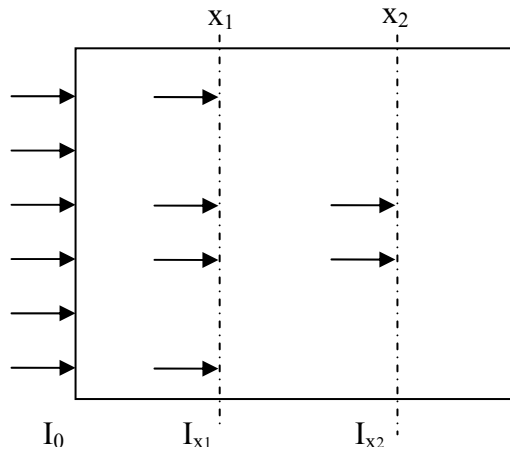


**Figure 6. Probability of gamma ray interaction between depths  $x_1$  and  $x_2$  expressed as the difference of attenuation at  $x_1$  and  $x_2$**

### **Detector Response to Gamma Radiation**

The response of a detector can be described by the probability that electrons and photons, “produced in interactions of the original gamma rays,” escape the detector volume before losing all of their energy (Knoll, 2000: 312). The electrons and photons are created from photoelectric and Compton interactions and include the photoelectrons, Compton electrons, Compton scattered gamma rays and bremsstrahlung radiation. The detector response and can be generalized in three size categories of small, intermediate

and very large (Knoll, 2000:312-317). The size refers to the detector's dimensions compared to the mean free path of subsequent electrons and photons. In a very large detector the mean free path is small compared to the detector dimensions and all energy is converted to information carriers. All interactions therefore correspond to counts under the "full-energy peak." In small detectors the dimensions are small compared to the mean free path of the electrons and photons and energy is lost when they escape. Therefore fewer information carriers are created and counts appear below the full-energy peak. In an intermediate size detector the probability of subsequent photons interacting before escape increases resulting in more information carriers created. This increases the number of counts closer to the full-energy peak.

The Amptek CdTe detector used has dimensions of  $1.0 \times 5.0 \times 5.0 \text{ mm}^3$  and generally displays small detector characteristics. In this research the gamma ray interaction of interest is a Compton event resulting in a scattered gamma ray of approximately 500 keV escaping the detector and a Compton electron of approximately 100 keV being collected in the detector. In CdTe the mean free path of a 500 keV gamma ray is 1.8 centimeters and the range of a 100 keV electron is 0.03 mm (Williams, 2004: 30). The relative size of the mean free paths to the detector dimensions shows that the scattered gamma ray has a high probability of escaping the detector volume while the Compton electron does not. Materials research continues to improve CdTe growth techniques but the technology for making larger CdTe detectors with good energy resolution does not yet exist. The current size limitation is one of the reasons this research is attractive and possible.

As shown in Figure 7, the incident gamma ray,  $\gamma(1)$ , Compton scatters in the detector with the scattered gamma escaping while the Compton electron is completely absorbed. Based on the Klein-Nishina formula and the Compton relation shown in Equations 2 and 3, a distribution of Compton scattered electron energies, called the “Compton continuum,” is characteristic of small detectors. The maximum energy deposited by a single Compton scatter corresponds to the gamma ray backscattering with  $\theta=\pi$  and is given as (Knoll, 2000:311):

$$E_C \equiv \frac{h\nu}{1 + 2h\nu/m_0c^2} \quad (7)$$

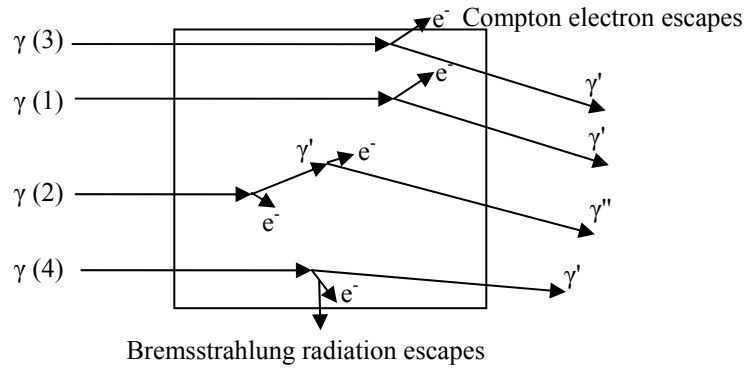


**Figure 7. Various gamma ray interactions affecting detector response**

This is known as the “Compton edge” and is shown in Figure 8. In intermediate size detectors, it is possible for multiple Compton scatters to occur, as illustrated with  $\gamma(2)$ , in Figure 7. This response leads to counts between the Compton edge and the full-energy peak.

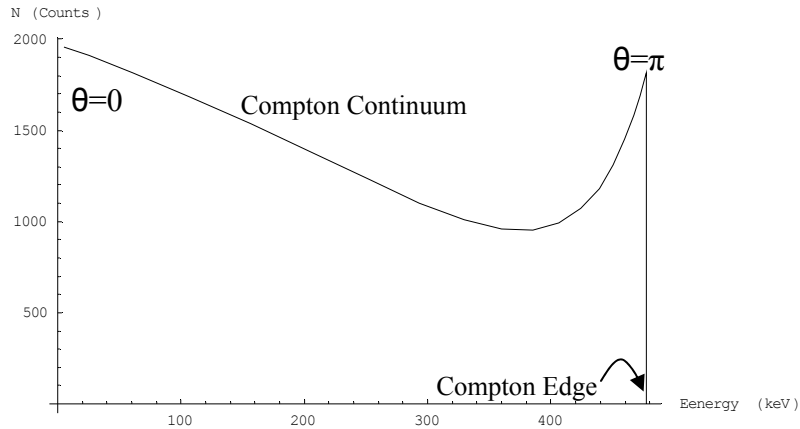


**Figure 8. Calculated Compton continuum and edge for a 662 keV photon in CdTe (full-energy peak not shown)**

Although the interaction of secondary gamma radiation as described above is unlikely in a small detector it can be more prevalent based on the source-detector geometry. Figure 9 shows two source-detector geometries. The dashed arrows represent a typically forward scattered gamma ray emitted from a Compton scatter event at a specific angle and the mean free path of the scattered gamma ray. Because of the larger angle created by the position of Source A, scattered gamma ray  $\gamma'_{1A}$  must travel farther through the detector material than  $\gamma'_{2A}$ ,  $\gamma'_{1B}$ , or  $\gamma'_{2B}$  to escape the detector volume. Therefore the Source A-detector geometry has a higher probability of producing multiple Compton scatter events than the Source B-detector geometry.

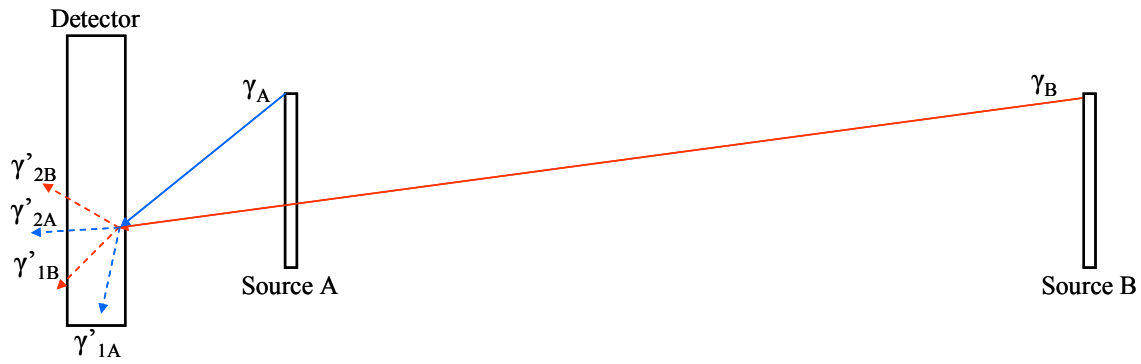


**Figure 9. Example of source-detector geometry effects on detector response**

### **Detector Response Complications**

The expected detector response can also be distorted because of secondary electrons or bremsstrahlung radiation escaping the detector volume before being absorbed as shown by  $\gamma$  (3) and  $\gamma$  (4), in Figure 7. In small size detectors the possibility of the secondary electrons leaking from the detector surface increases. Electron loss also increases for higher-energy incident radiation because the secondary electrons generally have higher energy and therefore longer range in the detector. This leakage results in the Compton spectrum to be altered favoring lower energies. Bremsstrahlung radiation is electromagnetic radiation created as the secondary electrons lose energy in the detector. Turner expresses the ratio of bremsstrahlung (radiative) to collisional stopping powers for an electron of energy  $E$  (MeV), in a material of atomic number  $Z$  as

*Radiative/Collisional*  $\cong ZE/800$  (Turner, 1995: 143). In CdTe the stopping power ratio for 662 and 100 keV electrons is .04 and .006 respectively. It is clear that bremsstrahlung is not a significant factor in the response of the detector.



## Detector Resolution and Efficiency

Detector resolution describes how well a detector can distinguish an energy peak of a given incident radiation and is quantified using the full-width at half-maximum (FWHM) divided by the peak centroid energy  $H_0$ . Similarly the resolution can also be described using the full-width at tenth-maximum (FWTM) divided by the peak centroid energy  $H_0$ . These standards are based on a Gaussian shaped peak. Figure 10 shows an example spectrum for 88 keV photons and the values used to calculate resolution.

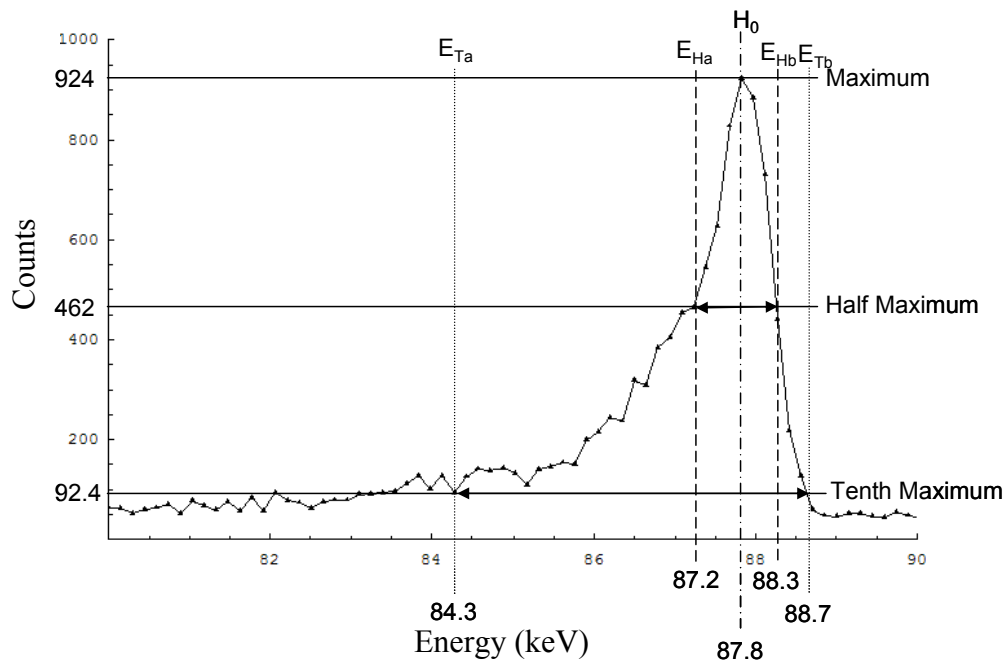


**Figure 10. Example energy spectrum for full-width at half-maximum and full-width at tenth-maximum resolution calculations**

$$\begin{aligned}
R_{FWHM} &= \frac{FWHM}{H_0} = \frac{E_{Hb} - E_{Ha}}{H_0} \\
R_{FWTM} &= \frac{FWTM}{H_0} = \frac{E_{Tb} - E_{Ta}}{H_0}
\end{aligned} \tag{8}$$

The calculated values from Figure 10 for  $R_{FWHM}$  and  $R_{FWTM}$  are 1.3% and 5.0%, respectively. The large difference in FWHM and FWTM of this example is characteristic for some semiconductor detectors. The asymmetric peak is caused by incomplete information carrier collection or secondary electron and bremsstrahlung escape from the detector (Knoll, 2000: 434-435). Consequently careful consideration of the detector system and application must be taken when choosing a resolution calculation method.

Knoll describes three factors that contribute to the FWHM ( $W_T$ ) in semiconductor detectors; charge carrier statistics ( $W_D$ ), charge carrier collection ( $W_X$ ) and electronic noise ( $W_E$ ) (Knoll, 2000: 417-419). The sum of the squared factors gives the squared total FWHM as follows

$$W_T^2 = W_D^2 + W_X^2 + W_E^2. \tag{9}$$

The first factor is due to the statistical fluctuation in charge carriers created and is calculated as

$$W_D^2 = (2.35)^2 F \varepsilon E, \tag{10}$$

where  $F$  is the Fano factor,  $\varepsilon$  is the energy needed to create an electron-hole pair, and  $E$  is incident gamma ray energy. The Fano factor is used to correct for observed deviations from Poisson statistics and ranges from unity for scintillation detectors to less than 0.1 for small germanium detectors (Knoll, 2000: 115-116). The Fano factor for CdTe is 0.15 and  $\varepsilon$  is 4.5 eV (Takahashi, 2000: 2).

The second contribution,  $W_X$ , is due to incomplete charge carrier collection which occurs when charge carriers are trapped or recombine before being collected. The effects of incomplete charge collection increase with larger detector volumes and lower electric fields. The contribution can be found experimentally by conducting FWHM measurements while varying the electric field. The assumption is that the effects of incomplete charge collection are insignificant when an infinitely large electric field is applied (Knoll, 2000: 417).

The last factor,  $W_E$ , is due to electronic components following the detector. It is measured directly by finding the FWHM of the spectrum produced by a precision pulse generator connected to the preamplifier. A parallel test point is often provided for this measurement (Knoll, 2000: 418).

The ability to distinguish two closely spaced peaks is essential to determining the isotopic ratio of a plutonium sample and is quantified using the figure of merit,  $M$ , shown in Figure 11. The figure of merit is given as

$$M = \frac{X}{W_a + W_b}, \quad (11)$$

where  $W_a$  and  $W_b$  are the FWHM of each peak and  $X$  is the difference between the peaks' centroids. Generally, a minimum value of one for  $M$  is needed to distinguish two peaks, and larger values are preferred.

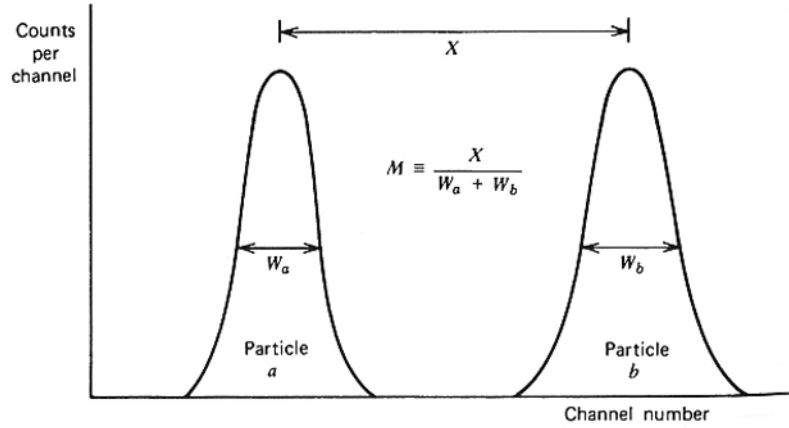


**Figure 11. Figure of Merit describes the ability of a detector to distinguish two energy peaks (Knoll, 2000: 680)**

Detector efficiency describes the ratio of pulses created by the detector to a number of radiation quanta emitted from a source and is critical in low count rate applications such as treaty monitoring. Absolute efficiency considers the total number of quanta emitted from a source while intrinsic efficiency considers only the radiation quanta incident on the detector volume. For an isotropic source they are related as  $\varepsilon_{\text{int}} = \varepsilon_{\text{abs}}(4\pi/\Omega)$ , where  $\Omega$  is the solid angle from the source subtended by the detector. The solid angle depends on the source-detector geometry. For parallel planar source and detector geometry, see Figure 12, the solid angle is calculated as

$$\Omega = \frac{\int \int (dA_s / 4\pi r^2) dA_d (\hat{\mathbf{n}} \cdot \mathbf{r} / r)}{A_s} \quad (12)$$

where  $A_s$  and  $A_d$  are the source and detector areas respectively,  $dA_s$  and  $dA_d$  are the differential source and detector areas respectively,  $\mathbf{r}$  is the vector from  $dA_d$  to  $dA_s$  with

magnitude  $r$ , and  $\hat{n}$  is a unit vector normal to detector surface (Tsoulfanidis, 1995: 268-269).

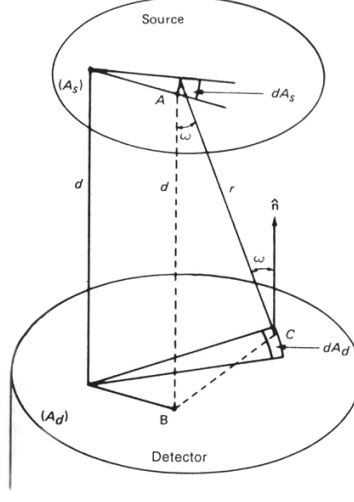


**Figure 12. Parallel planar detector-source geometry for calculation of solid angle subtended by detector from source (Tsoulfanidis,1995: 269)**

Tsoulfanidis presents a solid angle approximation for disk source and rectangular detector geometries:

$$\begin{aligned} \Omega = \frac{\omega_1 \omega_2}{4\pi} & \left[ 1 - \frac{3}{4} \psi^2 - \frac{1}{2} (\omega_1^2 + \omega_2^2) + \frac{1}{8} (5\psi^4 + 3\omega_1^4 + 3\omega_2^4) + \frac{5}{4} \psi^2 (\omega_1^2 + \omega_2^2) \right. \\ & - \frac{35}{64} \psi^6 + \frac{5}{12} \omega_1^2 \omega_2^2 - \frac{35}{16} \psi^4 (\omega_1^2 + \omega_2^2) - \frac{7}{32} \psi^2 (9\omega_1^4 + 9\omega_2^4 + 10\omega_1^2 \omega_2^2) \\ & \left. - \frac{7}{16} \omega_1^2 \omega_2^2 (\omega_1^2 + \omega_2^2) - \frac{5}{16} (\omega_1^6 + \omega_2^6) \right] \quad (13) \end{aligned}$$

where  $a$  and  $b$  are the rectangular detector dimensions,  $d$  is the source distance above the detector,  $R_s$  is the source radius,  $\omega_1 = a/d$ ,  $\omega_2 = b/d$ , and  $\psi = R_s/d$ . This approximation is valid for geometries where  $\omega_1$ ,  $\omega_2$ , and  $\psi$  are less than one (Tsoulfanidis, 1995:276-275).

Gotoh and Yagi used inverse trigonometric functions to determine the solid angle subtended by a rectangle at an arbitrary point  $(x_p, y_p, z_p)$ :

$$\Omega = \tan^{-1} \left( \frac{(x_2 - x_p)(y_2 - y_p)}{z_p [(x_2 - x_p)^2 + (y_2 - y_p)^2 + z_p^2]^{\frac{1}{2}}} \right) - \tan^{-1} \left( \frac{(x_1 - x_p)(y_2 - y_p)}{z_p [(x_1 - x_p)^2 + (y_2 - y_p)^2 + z_p^2]^{\frac{1}{2}}} \right) \\ - \tan^{-1} \left( \frac{(x_2 - x_p)(y_1 - y_p)}{z_p [(x_2 - x_p)^2 + (y_1 - y_p)^2 + z_p^2]^{\frac{1}{2}}} \right) + \tan^{-1} \left( \frac{(x_1 - x_p)(y_1 - y_p)}{z_p [(x_1 - x_p)^2 + (y_1 - y_p)^2 + z_p^2]^{\frac{1}{2}}} \right) \quad (14)$$

where the rectangular detector is enclosed by the four lines  $x = x_1$ ,  $x = x_2$ ,  $y = y_1$ , and  $y = y_2$  (Gotoh, 1971: 485).

### Signal-to-Noise Ratio and Minimum Detectable Activity

“Noise is any undesired fluctuation that appears superimposed on a signal source” (Knoll, 2000: 629). Noise affects the resolution of all detector systems but becomes critical when the noise variance is of the same or larger order of magnitude of the source variance. Generally, noise affects scintillation detectors less than semiconductor detectors. Where, in the signal chain the noise occurs, significantly affects the final magnitude of the noise. Noise at the beginning is amplified the same as the true signal therefore electronic noise often focuses on the preamplifier and its input stage. The signal to noise ratio can be quantified as  $S/N = N_S/N_B$ , where  $N_S = N_T - N_B$  is the counts attributed to the source,  $N_T$  is the total counts recorded, and  $N_B$  is the counts attributed to background noise.

The minimum detectable amount (MDA) represents the minimum measurable activity based on the detection system to provide a desired level of certainty that

radioactive materials are truly present. Equation 15 is often called the “Curie Equation” and gives the minimum number of counts  $N_D$  to ensure less than 5% false-negative counts and 5% false-positive given  $\sigma_{N_B} = \sqrt{N_B}$  (Knoll, 2000: 94-96).

$$N_D = 4.653\sigma_{N_B} + 2.706 \quad (15)$$

A minimum detectable activity ( $\alpha$ ) can then be calculated using the radiation yield per disintegration ( $f$ ), the absolute detection efficiency ( $\varepsilon$ ) and the counting time ( $T$ ) and is given as (Knoll, 2000: 96)

$$\alpha = \frac{N_D}{f\varepsilon T} \quad (16)$$

### **The Compton Spectrometer**

The Compton spectrometer consists of two detectors operating in a coincidence mode as shown in Figure 13. The incident gamma rays enter the first detector where they interact according to the linear attenuation coefficient as discussed above. Compton scatter events produce Compton electrons that are collected in the detector, referred as the electron energy analyzer (EEA). A fraction of the Compton scattered gamma rays will reach the second detector referred to as the photon energy analyzer (PEA). Because of the short distances traveled, the electron and photon pulses created are essentially coincident events. Associated electronics determine which events are true coincidence and the energy spectra of both detectors are collected. The EEA spectrum will consist of Compton scattered electron energies given by Equation 2 with  $\theta$  ranging from  $\theta_{\min}$  to  $\theta_{\max}$ . Similarly, the PEA spectrum consists of the scattered gamma ray energies given by

Equation 1 with  $\theta$  ranging from  $\theta_{\min}$  to  $\theta_{\max}$ . Some variation in  $\theta_{\min}$  and  $\theta_{\max}$  will occur due to the point of interaction in the EEA.

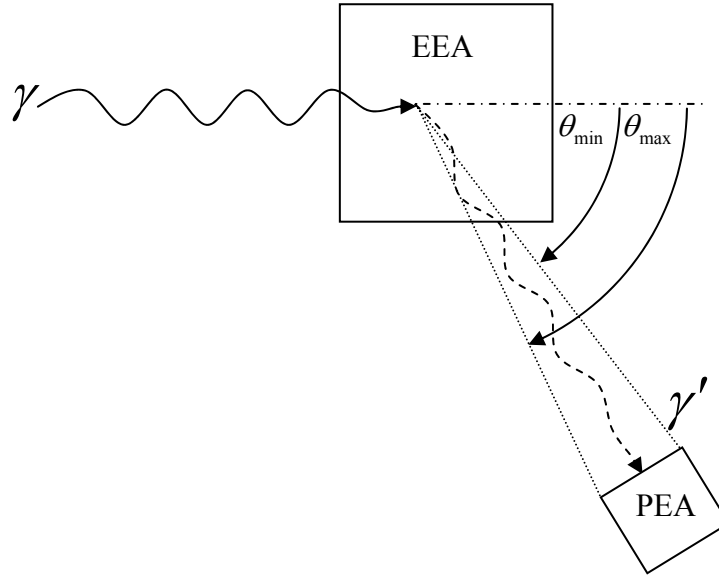


**Figure 13. The Compton spectrometer consisting of the electron energy analyzer (EEA) and the photon energy analyzer (PEA)**

The spectra collected in both the EEA and PEA are affected by the characteristic efficiency and resolution typical of those detector types. The coincidence requirement of the system significantly reduces background counts and therefore should increase the S/N ratio. Based on the expected incident gamma ray energies, the EEA is selected to provide the best resolution while maximizing the number of Compton scatter events. As previously discussed, the Compton cross section dominates for a wide range of energies especially in low Z materials. The PEA is selected for high efficiency, while resolution is less of a concern.



There are several advantages and disadvantages associated with the Compton spectrometer. The advantages include an improved S/N ratio from reducing background counts and better resolution from collecting the forward scattered and lower-energy Compton electron. As previously mentioned, the background radiation is expected to be significantly reduced because of the coincidence requirements. Similarly, the spectral artifacts such as backscatter peaks and x-ray escape peaks are also reduced because of the coincidence requirements. The improved S/N ratio is expected to significantly reduce the noise contribution to the FWHM. The collection of the Compton electron versus the photoelectron also reduces the energy-dependent contributions to the FWHM.

The  $W_x$  and  $W_d$  contributions to the FWHM increase with the amount of energy deposited in the detector, therefore the lower-energy Compton electrons are collected at a higher resolution. The Compton electrons generated from incident gamma rays are always lower in energy than the photoelectrons generated from the same gamma rays. For small gamma ray scatter angles the Compton electron energy can reach an order of magnitude less than the photoelectrons. The higher resolution Compton electron spectrum collected in the EEA can then be used to produce an incident gamma ray spectrum based on the non-linear Compton relation as demonstrated in Figure 14. In the example spectra, the 100-keV Compton electron peak has a resolution of 0.96%, which is reasonably attainable for this energy. The calculated 662-keV incident gamma ray peak has a resolution of 0.52%. This resolution is difficult to achieve without cryogenics. Calculations and further analysis of the Compton relations are found in Appendix D. Also an advantage of collecting the Compton electrons is their predominance of

scattering in the forward direction from 0-90 degrees (Turner, 1995: 178) resulting in less probability of the electrons escaping small detector volumes before complete energy collection.

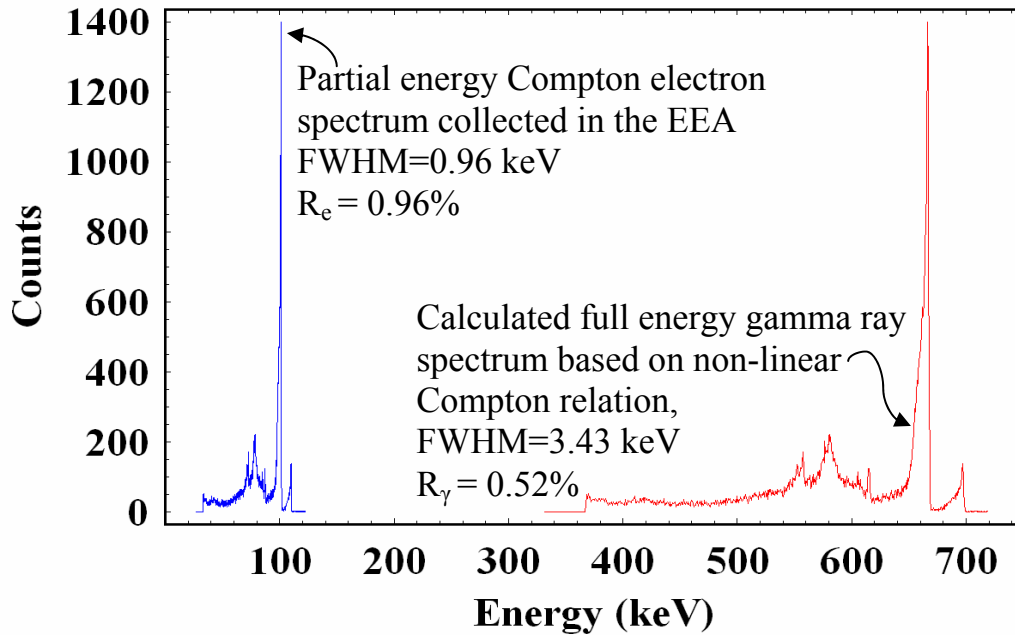


**Figure 14. Demonstration of the partial-energy Compton electron spectrum collected in the EEA converted to the calculated full-energy gamma ray spectrum based on Compton relation; Improved resolution from 0.96% to 0.52%**

The main disadvantage of the system is efficiency. The *total* Compton cross section in CdTe is predominant over the 300 to 700 keV gamma ray energy range. In the Compton spectrometer the solid angle subtended by the PEA is only a small portion of the  $4\pi$  steradians used to determine the *total* Compton cross section. Therefore, only a small portion of the *total* Compton cross section is utilized. For example, the *total* Compton cross section for a 662-keV photon in CdTe is  $6.4 \times 10^{-2} \text{ cm}^2/\text{gram}$  while the Compton cross section utilized in the Compton spectrometer is  $1.9 \times 10^{-4} \text{ cm}^2/\text{gram}$ . This

is nearly two orders of magnitude less than the photoelectric cross section of  $1.2 \times 10^{-2}$   $\text{cm}^2/\text{gram}$  for the same photon energy. The efficiency problem is further compounded by strict source collimation requirements. To maintain a reasonable resolution in the Compton electron spectrum, the source must be collimated to the EEA to minimize the scatter angle deviations. Collimation and alignment considerations of the system play a significant role in the effectiveness of the system.

### **III. Equipment**

#### **Chapter Overview**

The purpose of this chapter is to describe the equipment used in this thesis. The chapter is divided into five sections covering the complete system configuration, detectors, electronics, collimators and radioactive sources. First, an overview of the system configuration is discussed. Then the Amptek XR-100T-Cadmium Telluride (CdTe) and Bicron Model 3M3/3 thallium-doped sodium iodide (NaI(Tl)) detectors and their associated pulse-processing electronics are reviewed. Next, the purpose and general characteristics of the nuclear instrument module (NIM) pulse-processing electronics used for coincidence determination and spectrum collection are covered, followed by an examination of the materials and dimensions of the linear and conical collimators. Finally, the radioactive sources used are outlined.

#### **Compton Spectrometer System**

The Compton spectrometer system used in this thesis is based on the design used by Capt. Williams shown in Figure 15 (Williams, 2004: 44-46). The gamma rays originate at position 1 from a typically isotropic sample. As they move through position 2, the gamma rays are collimated to the EEA (CdTe) at position 3 and more importantly, they are aligned normal and centered on the conical collimator at position 4. The gamma rays interact in the EEA and some scatter out through the conical collimator to the PEA (NaI(Tl)) at position 5. When coincidence pulses occur in the pulse-processing

electronics the energy data of the EEA and PEA are sent to the spectrum-collection electronics.

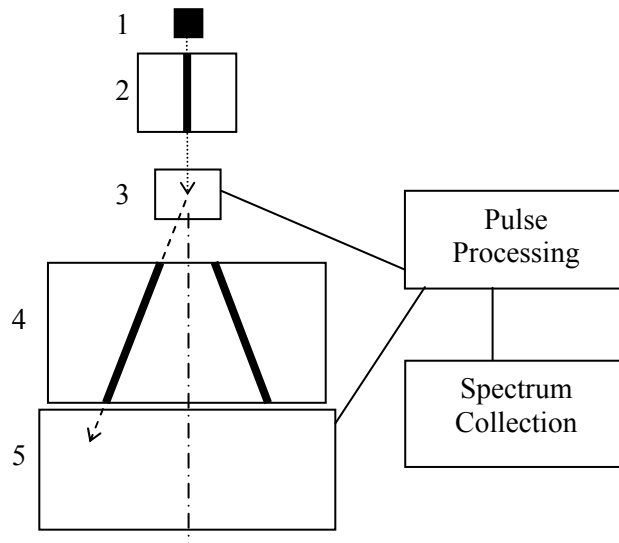


**Figure 15. Compton spectrometer configuration; 1. Isotropic sample, 2. Initial linear collimator, 3. EEA (CdTe detector), 4. Conical collimator, 5. PEA (NaI(Tl) detector)**

## Detectors

### Electron Energy Analyzer

The EEA consists of the Amptek Model XR-100T-CdTe detector and the Model PX2T power supply and amplifier which are pictured and tabulated in Appendix E. The 5x5x1 mm<sup>3</sup> CdTe crystal is mounted on a thermoelectric cooler as shown in Figure 16. The cooler maintains the detector crystal, the field-effect transistor (FET), and feedback components at approximately -30 degrees Celsius, which can be monitored through connections at the PX2T (Amptek, 2002: 20).

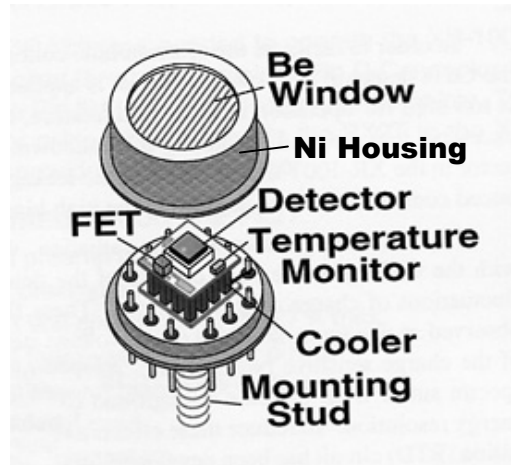


**Figure 16. CdTe hermetic detector housing (Amptek, 2002: 20)**

The detector housing is designed for gamma rays to enter through a 10 mil beryllium window incident on the  $5 \times 5 \text{ mm}^2$  CdTe crystal face. In the Compton spectrometer configuration, the gamma rays enter through the 10-mil thick, nickel wall of the detector housing to strike the  $1 \times 5 \text{ mm}^2$  edge of the CdTe crystal. The difference in gamma ray attenuations for nickel and beryllium has minimal effect on the system as shown in Appendix F. The output of the FET is sent to the Amptek A250 charge sensitive preamplifier. The negative preamplifier signal is sent to the PX2T. The PX2T provides the +400 volt detector bias, the  $\pm 8$  volt preamplifier power, the +8 volt temperature monitor power and the 0-3 volt cooler power. The PX2T also includes a triangular pulse-shape amplifier, output shown in Figure 17, and a rise-time discriminator (RTD). The RTD reduces the characteristic “hole tailing” of the energy spectrum created by inefficient hole collection which degrades energy resolution as shown in Figure 18. Essentially the RTD discards pulses that originate from interactions farther into the

detector from where the holes must travel a large portion of the detector width before being collected.

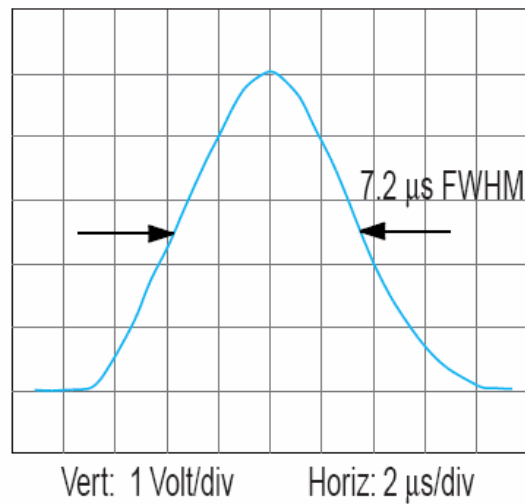


**Figure 17. PX2T Shaping Amplifier output with RTD inactive (Amptek, 2002: 21)**

This longer travel time increases the probability of recombination resulting in lower-energy pulses recorded. The improvement in resolution with the RTD active is at the cost of efficiency since the active volume of the detector is decreased. The RTD is activated at the PX2T, and the sensitivity can be adjusted internally at R22. To evaluate the decrease in efficiency the PX2T provides a rear panel input count rate (ICR). A lower level discriminator is set just above the noise level creating a short output pulse for all events regardless of energy-collection time. This count rate can then be compared with the count rate from the RTD to determine a relative efficiency. In the characterization of the detector a Canberra Model 3125 high voltage power supply (HVPS) is used to provide the variable bias voltage for the CdTe detector.

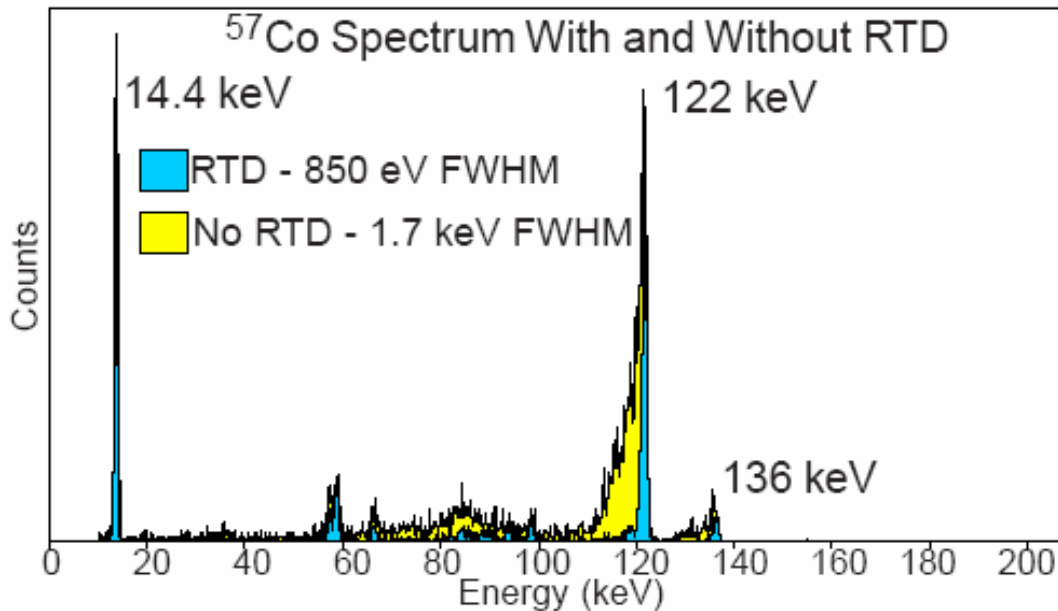


**Figure 18. Energy spectrum with and without RTD active demonstrating the reduction in hole tailing (Amptek, 2002: 21)**

### **Photon Energy Analyzer**

The PEA consists of the Bicron Model 3M3/3 thallium-doped sodium iodide (NaI(Tl)) scintillation detector and pulse-processing electronics pictured and specified in Appendix G. The NaI(Tl) crystal has a 3 inch diameter and 3 inch depth resulting in a 21.2 inch<sup>3</sup> volume. “NaI(Tl) produces the highest signal in a photomultiplier tube (PMT) per amount of radiation absorbed in the crystal of all presently known scintillators” (Bicron, 2002: 1). The Bicron PA-14 preamplifier connects directly to the 14-pin output of the PMT and provides gain balance (G) and focus (F) potentiometers for fine adjustments in pulse height and resolution. The detector is operated at a bias voltage of approximately +900 volts, and is provided by a computer-controlled Canberra 9645 HVPS. The -24-volt power required for the PA-14 is a standard output on ORTEC



amplifiers. Both the ORTEC Model 672 Spectroscopy Amplifier and ORTEC 579 Fast Filter Amplifier were used to process the NaI(Tl) energy pulses. The 672 provided more shaping options and better energy resolution with less stable timing characteristics (ORTEC, 2004: 3.46-3.49). On the other hand, the 579 provides a fast rise time and better timing characteristics (ORTEC, 2004: 3.36-3.39) while sacrificing energy resolution. Bicron quoted specification for the NaI(Tl) detectors is  $7.0 \pm 0.2\%$  resolution, resulting in a FWHM of less than 50 keV for 662 keV gamma rays.

### **Coincidence Electronics**

Two methods for determining the coincidence of the EEA and PEA pulses were used; the pulse start-stop technique using a time-to-amplitude converter (TAC) and the pulse overlap technique using a slow coincidence unit. The equipment used for both methods is specified in Appendix H.

In both methods the first step is to discriminate the timing of a pulse's arrival. This process is complicated by amplitude and rise-time walk and jitter as shown in Figure 19. A timing pulse is generated when a trigger level is crossed, but the timing of two true coincident events can be different based on the pulse shapes. Most ORTEC electronics use a trailing-edge constant-fraction method to minimize the effects of amplitude walk but are still susceptible to variations in pulse shapes.

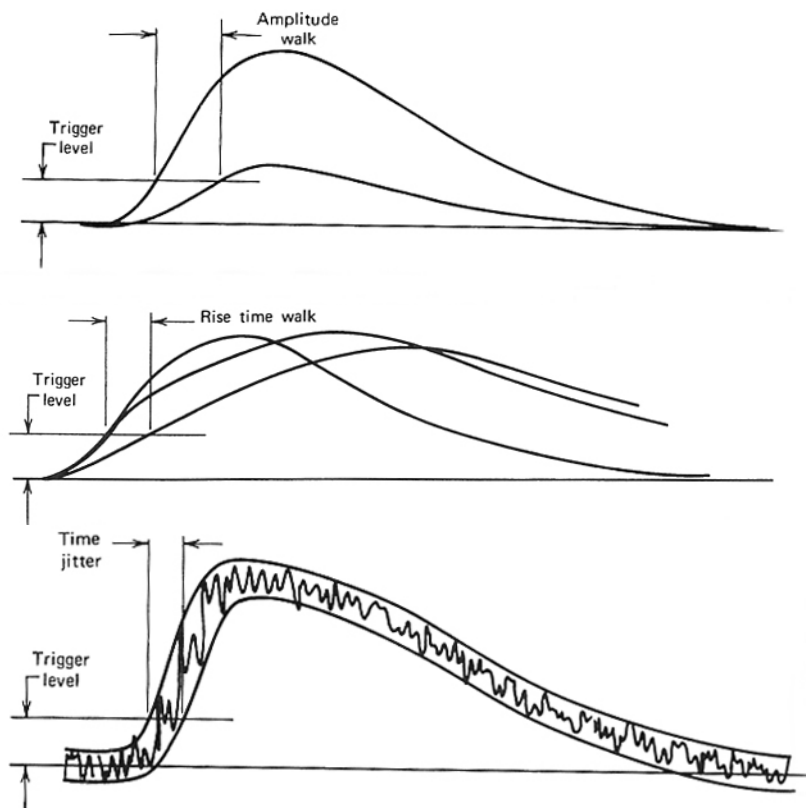


**Figure 19. Amplitude walk, rise-time walk and jitter effects on pulse discrimination (Knoll, 2002: 659-661).**

The ORTEC Model 551 Timing Single-Channel Analyzer (T-SCA) and Model 552 Pulse-Shape Analyzer (PSA)/T-SCA were used to derive the timing signals. Both modules use ORTEC’s “patented trailing-edge constant-fraction (CF) timing technique” (ORTEC, 2004: 4.9) with optional rear panel connectors providing standard leading edge timing. The main difference between the modules is the 551’s CF is set at 50% while the 552 provides an A and B channel output both with separate CF settings. This allows information about the pulse-shape to be obtained. Each module can provide positive or negative NIM-standard output pulses (ORTEC, 2004: 4.7-4.11).

While using the TAC method, the fast-negative timing pulses from the PSA/T-SCAs are sent directly to the ORTEC Model 566 TAC. The TAC provides a square output pulse with amplitude proportional to the time between the start and stop pulses. To limit dead-time associated with receiving a second start pulse before a stop pulse, the higher-count-rate output of the NaI(Tl) is connected to the stop gate. The output spectrum from the TAC should show a “prompt coincidence peak” associated with true coincidence on top of a chance coincidence continuum (Knoll, 2002: 666-667). A SCA is then used to select the prompt coincidence peak.

Operating in the pulse overlap method, square logic pulses are required at the input of the ORTEC Model 409 Linear Gate and Slow Coincidence (LGSC) unit. The narrow T-SCA outputs are sent to ORTEC Model 416A Gate and Delay Generators (GDG) to adjust the delay, width, and amplitude of the gating pulses (ORTEC, 2004: 11.8). The LGSC uses the simple AND gate producing a logic gate pulse anytime the coincidence inputs overlap. The coincidence alignment and resolving times are determined by the delay and pulse width, respectively, from the adjustable GDGs.

The logic gate produced from the LGSC or the TAC-SCA combination is then sent to the Canberra Model 9633 Analog-to-Digital Converters (ADC) parallel to the energy pulses of the EEA and PEA. The ADC processes only those energy pulses with coincident gate pulses, assigning each pulse to an energy bin as established with the Canberra Genie 2000 software. The data is then transferred through the Canberra Model 5556A Acquisition Interface Module (AIM) to a PC running the Genie 2000 software. A

single AIM is capable of connecting multiple ADCs to a single PC and the system was established to collect both the EEA and PEA energy spectra simultaneously.

## **Collimators**

The Compton spectrometer requires an initial linear collimator from the source to the EEA and a conical collimator from the EEA to the PEA as shown in Figure 15. Two different initial collimators, shown in Appendix I, were used; one with a circular cross section of radius 1.5 mm and the other with a hexagonal cross section with internal radius of 1.5 mm. The circular collimator is made of lead and was drilled by the AFIT model shop. A source holder was centered on the hole and attached to facilitate consistent system setup. The hexagonal collimator is the original collimator used by Capt. Williams (Williams, 2004: 45). The conical collimator was constructed of AIM70, a lead-bismuth alloy with a melting point of 70° Celsius, by Capt Williams (Williams, 2004: 122-123) and its dimensions and diagrams are located in Appendix J. The angle of the cone is 0.53 radians, which corresponds to a 100-keV Compton-scattered electron from an incident 662 keV gamma ray. The inside cone is parallel to the outside cone and by adjusting its height relative to the outside cone changes the collimator gap size. Spacers are used to select different gap sizes.

## **Radioactive Sources**

Many radioactive sources were used throughout this thesis and a tabulated list is located in Appendix K.  $^{57}\text{Co}$ ,  $^{137}\text{Cs}$ ,  $^{152}\text{Eu}$  and multinuclide sources were all used for energy calibration and detector characterization. The  $^{22}\text{Na}$  511keV annihilation gamma

rays were used for aligning the EEA and PEA pulses for coincidence.  $^{137}\text{Cs}$  was the primary isotope used to evaluate the Compton spectrometer. All three available  $^{137}\text{Cs}$  sources were combined to provide an activity of approximately 25  $\mu\text{Ci}$ . The adjusted activity of the combined source ignored self-absorption. Adjusted activity calculations are demonstrated in Appendix L.

## **IV. Methodology**

### **Chapter Overview**

This chapter outlines five key actions taken during this thesis research and their purpose: 1. test and characterize the CdTe and NaI(Tl) detectors individually, 2. construct system housing to facilitate a reproducible geometry with improved component alignment, 3. establish EEA and PEA timing pulse alignment and assess both coincidence methods described above, 4. collect Compton spectrometer data for system analysis and 5. develop and assess a computer simulated Compton spectrometer to further understand the geometric relations and interaction probabilities of the system.

### **Detector Testing and Characterization**

To best evaluate the Compton spectrometer's performance, the individual detectors' resolution and efficiency were determined first. First, the CdTe resolution and efficiency were determined using the geometry shown in Figure 20. The system was evaluated with the rise time discriminator (RTD) on and off, with  $^{137}\text{Cs}$  and  $^{57}\text{Co}$  in positions one and two. Sample  $^{57}\text{Co}$  pulse-height spectra for each geometry are shown in Figure 21 and Figure 22.

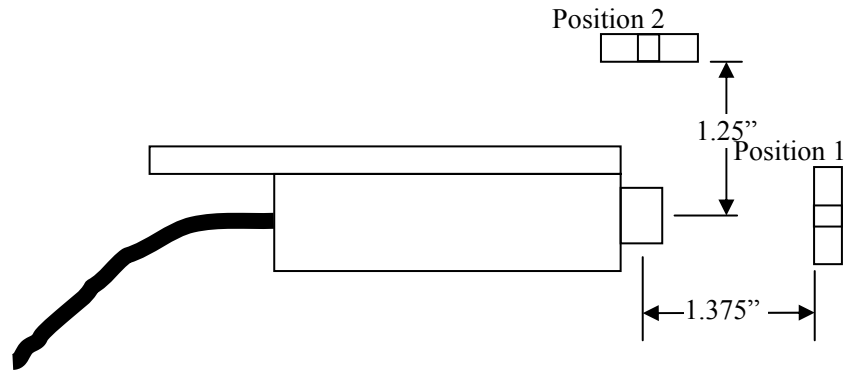


**Figure 20. CdTe resolution and efficiency geometry**

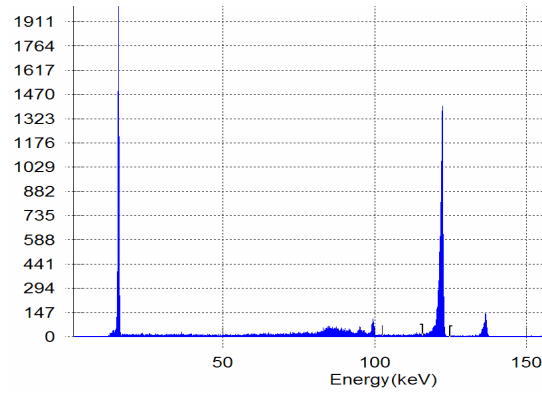


**Figure 21. Sample  $^{57}\text{Co}$  spectrum using CdTe detector (RTD on, Position 1)**

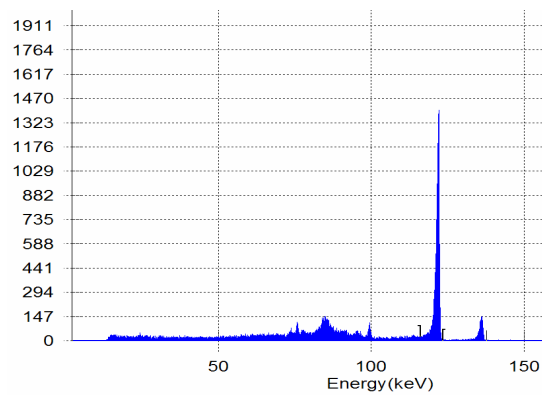


**Figure 22. Sample  $^{57}\text{Co}$  spectrum using CdTe detector (RTD on, Position 2)**

A separate experiment was conducted as described in Knoll to determine the  $W_E$ ,  $W_D$ , and  $W_X$  components of the FWHM (Knoll, 2000: 416-419). The FWHM was determined for six gamma ray energies from  $^{57}\text{Co}$ ,  $^{152}\text{Eu}$  and  $^{137}\text{Cs}$  while increasing the detector bias. A modification to one CdTe system, as shown in Figure 23, was performed to facilitate an external variable power supply while the PX2T performed all of its other power and amplification tasks. The maximum bias voltages applied was 775 volts based on the manufacturer's guidance not to exceed 800 volts. The FWHM was also determined with an ORTEC precision pulser. FWHM were determined for pulser amplitudes equivalent to 100, 200 and 350 keV for each bias setting.



**Figure 23. Modified PX2T for external power supply.**

Next, the NaI(Tl) detector resolution and efficiency were evaluated using the geometry shown in Figure 24. Energy spectra were collected for 10 minutes using two sources,  $^{137}\text{Cs}$  and  $^{57}\text{Co}$ . A sample spectrum is shown in Figure 25. The resolution was also evaluated at four positions of the focus adjustment on the PA-14 and the optimized



setting was recorded and used throughout the remainder of the thesis research. Efficiency calculations included peak and total efficiencies for both absolute and intrinsic measurements.

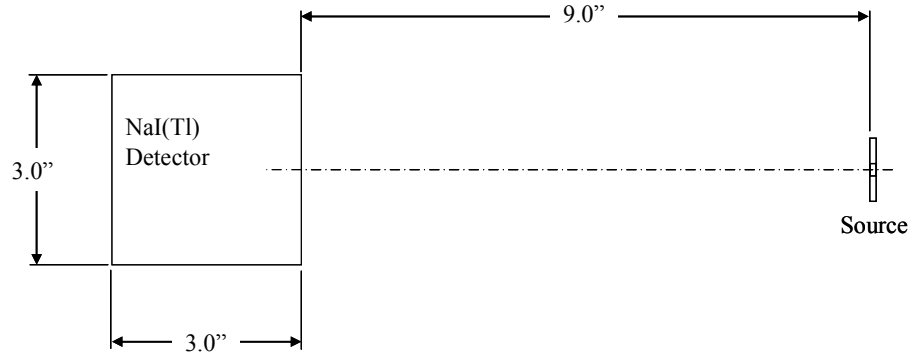


**Figure 24. NaI(Tl) resolution and efficiency geometry**

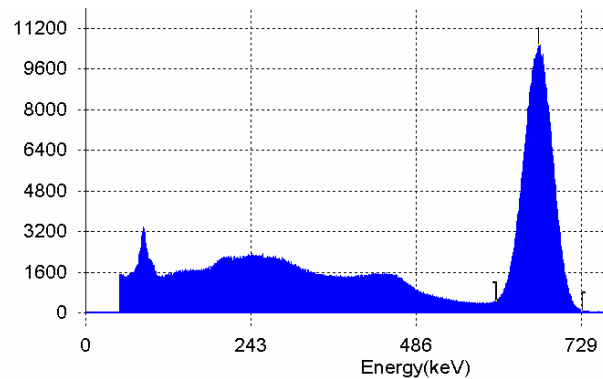


**Figure 25. Sample  $^{137}\text{Cs}$  spectrum using NaI(Tl) detector in characterization geometry**

### System Housing Construction

Alignment of the source, linear collimator, EEA, and conical collimator presented a problem to establishing the Compton spectrometer. Independent movement of the linear collimator and the EEA relative to the conical collimator is needed to evaluate

alignment and to provide reproducible geometries. A wooden structure shown in Figure 26 was created to facilitate this requirement. The structure holds the PEA flush against a Plexiglas sheet the conical collimator rested on. This maximizes the PEA detector volume in line with the cone path. The linear collimator rests on a Plexiglas stage over the conical collimator and EEA, allowing the independent adjustment of the linear collimator and EEA needed. Component alignment techniques included the use of a laser and a solid rod. Both were directed through the initial collimator for alignment with conical collimator, and then the EEA was moved into position without disturbing the collimators.



**Figure 26. Compton spectrometer housing**

## **Timing Pulse Alignment and Coincidence Method Evaluation**

Once the characterization of the detectors and the physical geometry of the Compton spectrometer were complete, the timing electronics were established and evaluated. Both the T-SCA and PSA/T-SCA were used to produce timing pulses from the EEA and PEA energy pulses and tested for timing variation due to amplitude walk. A pulser signal was sent through the amplifiers of the detectors to produce simulated energy signals similar to those created when a gamma ray interacts in the detectors. Timing pulses were created for these simulated energy pulses using the T-SCA and PSA/T-SCA. Variations in the timing of the original pulser signal and the timing discriminator signal were measured using the oscilloscope measurement tools over a wide range of pulser amplitudes. Variations were attributed to the effects of amplitude walk.

The pulser was then used to align the EEA and PEA timing pulses with each other for the pulse overlap coincidence method. The alignment was adjusted using the built in variable-delays of the pulse discriminators, visually established using the oscilloscope, and verified by counting the number of coincidence events over a set time. The pulser operates at 60 Hz therefore any variation in that rate showed the coincidence method operating improperly. The PA-14 did not provide a test pulse input, and the pulser amplification started after the PEA's preamplifier. A  $^{22}\text{Na}$  source was placed between EEA and PEA and delay curves were created to identify the optimal pulse alignment. Similarly, the pulser was used to test the coincidence of the TAC method. The output of the TAC was monitored in the Genie software to verify proper operation. Again, a pulse rate of 60 Hz was expected under the prompt coincidence peak and variations indicated

improper operation. Using the built in variable-delays of the pulse discriminators, the shift of the prompt coincidence peak in the Genie software was verified. A  $^{22}\text{Na}$  was then placed between the EEA and PEA to further evaluate the TAC method.

Both coincidence methods produce a logic pulse when the system determines there is a true coincident event. The triggering of this logic pulse depends on the method used but is always delayed with reference to the energy pulses. The energy pulses are sent through delay amplifiers for alignment with the logic pulses at the input to the ADCs. The ADCs, when operating in the coincidence mode, process only the energy pulses that have a corresponding logic pulse.

### **Compton Spectrometer Data Collection**

The energy spectra from the EEA and PEA were collected for varying conical collimator gap widths using both coincidence methods and both initial collimators. Because the spectra were expected to have a significant dependence on the alignment of the system components, graduated scales were printed and affixed to the EEA and the top of the conical collimator as shown in Appendix E and Appendix J. The graduated scales were used to determine the location of the CdTe crystal in the detector housing, to evaluate the effects of the RTD on the active detector volume and to reproduce component alignments.

The location of the CdTe crystal and the effects of the RTD were determined by systematically moving the EEA through a collimated  $^{137}\text{Cs}$  beam and comparing the count rate from the ICR to the count rate from the RTD. One-hour counts were

conducted for eight locations along the graduated scale on the EEA. The location corresponding to the maximum RTD count rate was used as the alignment point for the EEA throughout the remainder of the experiments.

The Compton spectrometer energy spectra from the EEA and PEA were collected for ten hours using  $^{137}\text{Cs}$ . The alignment of the initial collimator and the conical collimator were adjusted and analyzed for five positions using the graduated scale on the conical collimator. The alignment process was done in two steps. First, the initial collimator was aligned with a specific grid location on the conical collimator graduated scale. Then the EEA was moved into position and aligned using the graduated scale location corresponding to the maximum RTD count rate. Finally, a 74-hour count was collected using  $^{22}\text{Na}$ .

### **Compton Spectrometer Simulation Code**

A program was written to simulate the Compton spectrometer in order to assess the effects of varying geometric parameters on the resolution and efficiency of the system. The geometric parameters that can be changed include the dimensions and relative locations of the initial collimator, the EEA detector and the second collimator. The program divides the source into equal incremental areas, the EEA into incremental volumes and the gap at the bottom of the conical collimator into equal incremental areas. This creates a finite number of three-“point” combinations consisting of a source area, an EEA volume and a conical collimator area. All possible combinations are analyzed by

performing four main calculations as outline below. The *Mathematica* code and a detailed description of its function are given in Appendix M.

The first main calculation determines if the three-point combination is “geometrically possible.” The program uses basic geometric and algebraic equations to answer two questions. First, does the source gamma ray pass through the hole at the bottom of the initial collimator before reaching the EEA? Second, does the scattered gamma from the EEA pass through the gap of the conical collimator to the PEA? If both answers are positive, the three-point combination is “geometrically possible” and the remaining four calculations are performed.

Since the source gamma passed through the initial collimator hole and reached the EEA, the next question is, at what probability does the isotropic point source emit gamma rays into the top surface of the incremental detector volume? This probability is described as the solid angle subtended by the incremental detector volume from the source point. The program’s second calculation uses Equation 14 to determine this probability.

The source gamma has now reached the incremental detector volume and must Compton scatter at a specific range on angles to pass through the conical collimator gap. The third calculation determines the probability that this scatter will occur in two steps. First it performs the solid angle integration of the Klein-Nishina formula, Equation 4, over the specific scatter angles needed to determine the Compton scatter cross section for

that three-point combination. This cross section is used in Equation 6 to determine the probability of interaction through the depth of the incremental detector volume.

The fourth calculation “bins” the product of the above calculated probabilities according to the Compton electron energy associated with the three-point combination. The energy is found by using the average scatter angle in the Compton relation described in Equation 2. The program continues to sum the probabilities in the energy channels until all three-point combinations have been examined. The result is an energy spectrum showing the probability of that energy occurring. This spectrum can then be used to evaluate different designs or for comparison with experimental data.

## **V. Data Analysis and Results**

### **Chapter Overview**

This chapter covers the experimental and simulated data collected during this research and is divided into five sections following the methodology of Chapter IV.

1. CdTe and NaI(Tl) detector characterization including resolution and efficiency.
2. The effects of the Compton system geometry on detector efficiencies.
3. Analysis of the start-stop and pulse overlap coincidence timing methods.
4. Analysis of experimental energy spectra from the Compton system.
5. Analysis of simulated energy spectra.

### **CdTe Characterization**

The experimental procedures began with the evaluation of the CdTe detector resolution and efficiency. Eight energy spectra were taken using the geometry described in Figure 20 and are located in Appendix N. The resolution data is summarized in Table 2 and Figure 27. Generally, the detector performed above the expected standards given by the manufacturer and I am confident it is operating properly.

Both the 1.1 keV FWHM at 122 keV and the 5.27 keV FWHM at 662 keV with the RTD active were better than the Amptek's specification of 1.239 keV (Amptek, 2004: 2) and 5.9 keV (Amptek, 2004: 28) respectively. No specifications were given for the RTD inactive, but Figure 18 shows that an increase in FWHM is expected. The 10.21 keV FWHM at 662 keV in Position 2 with the RTD active is larger than expected. Poorer resolution was found for all readings from Position 2 except for the 662 keV,



inactive RTD reading. One factor for this general trend is the additional scattering caused by the nickel detector housing in Position 2 versus the beryllium window in Position 1. The additional scatters create a distribution of photon energies which causes an increase in the FWHM.

**Table 2. CdTe FWHM Analysis Data**

RTD	Position	Energy (keV)	FWHM (keV)	$\sigma$ (FWHM) (keV)	Resolution (%)	$\pm\sigma$ (Resolution) (%)
On	1	122.0	1.07	0.01	0.88	0.01
		136.3	0.98	0.04	0.72	0.03
		661.7	5.27	0.15	0.80	0.02
	2	121.8	1.16	0.02	0.95	0.02
		136.0	1.16	0.06	0.85	0.04
		662.7	10.21	0.22	1.54	0.03
Off	1	121.9	1.41	0.03	1.16	0.02
		136.6	1.13	0.07	0.83	0.05
		661.4	25.52	1.5	3.86	0.23
	2	122.4	1.55	0.04	1.27	0.03
		136.7	1.4	0.08	1.02	0.06
		661.6	20.91	0.5	3.16	0.08
Quoted resolution from Amptek						
RTD	Position	Energy (keV)	FWHM (keV)		Resolution (%)	
On	1	122.0	1.24		1.02	
On	1	662.0	5.9		0.89	

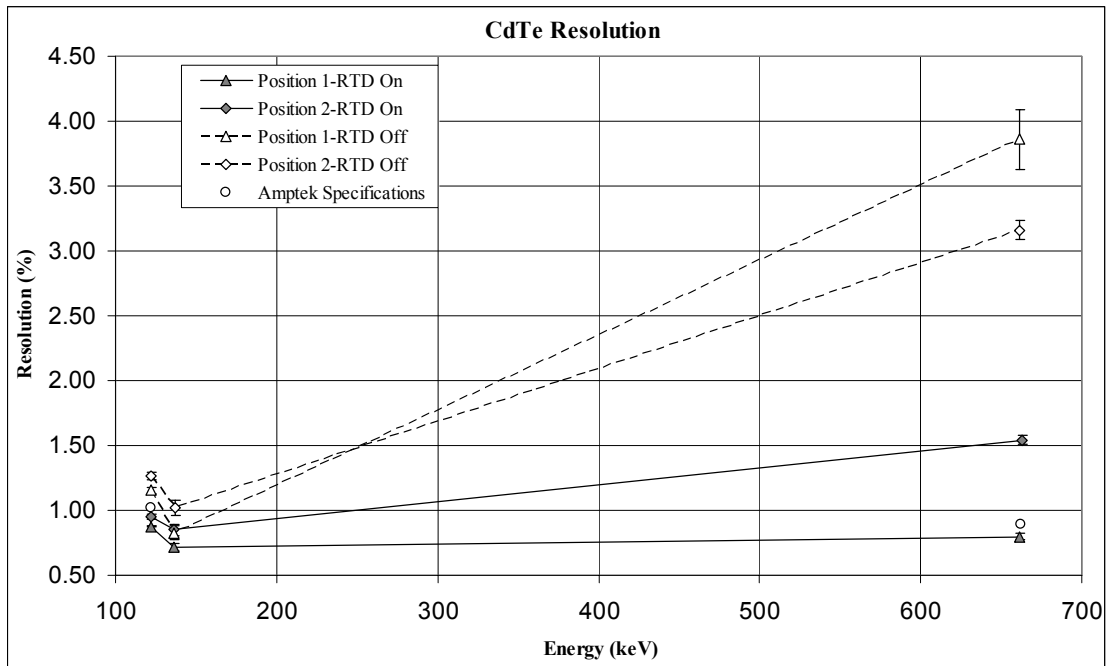


**Figure 27. CdTe resolution vs. gamma ray energy**

Using the same energy spectra from above the absolute and intrinsic peak efficiencies were calculated. The absolute peak efficiencies are summarized in Table 3 and Figure 28 and the intrinsic peak efficiencies are summarized in Table 4 and Figure 29. The effects of the RTD on and off and in Position 1 and 2 depend on the energy of the gamma ray. As expected the absolute efficiency for the low-energy gamma rays was greater in Position 1 than Position 2 with the RTD both on and off. The greater interaction probability associated with the depth advantage achieved in Position 2 is not significant for low gamma ray energies. This is further demonstrated by the fact that there is only a fractional increase in the efficiency with the RTD switched from on to off for low-energy gamma rays entering from Position 1. The high-energy gamma ray efficiencies behave differently. High-energy gamma rays entering from Position 1

experience over 530% increased efficiency with the RTD switched from on to off. The efficiency with the RTD on also increased over 210% from Position 1 to Position 2, demonstrating the increased significance of the depth advantage in Position 2 with higher energies.

**Table 3. CdTe Absolute Peak Efficiency Data**

<b>RTD</b>	<b>Position</b>	<b>Energy (keV)</b>	<b>Net Peak (Counts)</b>	<b>Net Area Uncertainty (Counts)</b>	<b>Absolute Efficiency (%)</b>	<b>Absolute Eff. Uncertainty (%)</b>
<b>On</b>	<b>1</b>	122	7740	504.8	2.08E-02	6.68E-04
		136	680	57.8	1.56E-02	7.52E-04
		662	15656	153.4	9.01E-05	8.83E-07
	<b>2</b>	122	6720	646	9.23E-03	2.99E-04
		136	567	73.8	7.41E-03	3.83E-04
		662	9670	105.4	1.94E-04	2.12E-06
<b>Off</b>	<b>1</b>	122	8170	1056.9	2.48E-02	8.34E-04
		136	744	64	1.66E-02	1.04E-03
		662	44729	286.3	4.80E-04	3.07E-06
	<b>2</b>	122	7830	917.3	1.29E-02	4.31E-04
		136	849	60.9	9.96E-03	5.71E-04
		662	59802	293	3.23E-04	1.58E-06

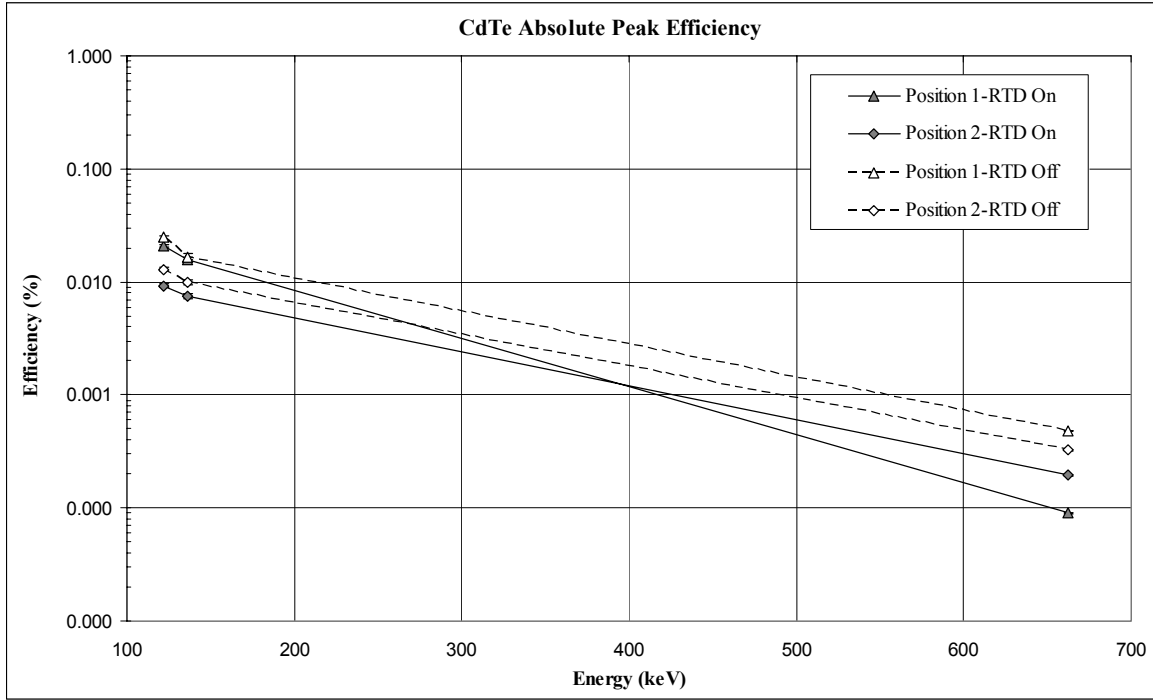


**Figure 28. CdTe absolute peak efficiency plot, source-detector geometry shown in Figure 20**

The intrinsic efficiency calculations take into consideration the solid angle subtended by the detector and the decrease in detector width experienced with the RTD active. Position 2 intrinsic efficiencies are greater because of the significant decrease in the solid angle subtended from Position 1 (5mm x 5mm) to Position 2 (1mm x 5mm) and the increased interaction depth of Position 2. An estimated decrease in detector width of 70% was used based on the ratio of counts from the RTD to the ICR found when determining the location of the crystal inside the detector housing. The highest intrinsic efficiency of 77% was found from Position 2 with the RTD active.

**Table 4. CdTe Peak Intrinsic Efficiency Data**

RTD	Position	Energy (keV)	Solid Angle (Steradians)	Intrinsic Efficiency (%)	Int. Eff. Uncertainty (%)
On	1	122	0.0206	12.688	0.407
		136	0.0206	9.516	0.459
		662	0.0206	0.055	0.001
	2	122	0.0015	77.325	2.505
		136	0.0015	62.078	3.209
		662	0.0015	1.625	0.018
Off	1	122	0.0206	15.128	0.509
		136	0.0206	10.126	0.634
		662	0.0206	0.293	0.002
	2	122	0.0040	40.527	1.354
		136	0.0040	31.290	1.794
		662	0.0040	1.015	0.005

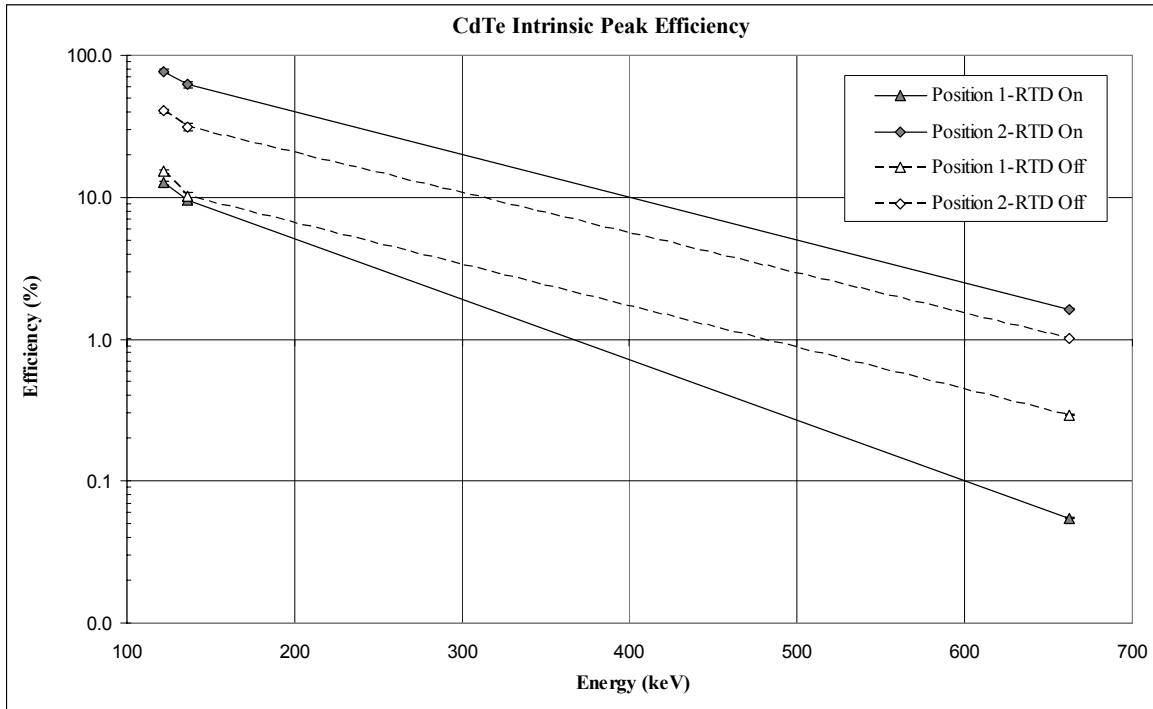


**Figure 29. CdTe peak intrinsic efficiency plot, source-detector geometry shown in Figure 20**

To further characterize the CdTe detector an experiment to determine the contributions to the FWHM was conducted. As shown in Figure 30, the plot of the  $\sqrt{W_T^2 - W_E^2}$  versus the inverse high voltage showed that the CdTe does not behave in the same way the Si(Li) detector described by Knoll does (Knoll, 2000: 418-419). The expected plot would show a decreasing  $W_X$  contribution to the FWHM as the high voltage increased. The data then could be extrapolated to an infinite voltage where the contributions of  $W_X$  would be minimal. The remaining contribution would be contributed only to  $W_D$ . The y-intercept of the extrapolated lines representing the expected contributions of  $W_D$  to the FWHM and an estimated Fano factor are shown in Table 5. A large range of Fano factors from 0.007 to 1.61 was found. Fano factors range from greater than zero to one and are typically less than 1/3 for semiconductors. Only the Fano factor for the 59 keV gamma ray of 0.25 was of the expected order of magnitude. Because the HVPS was not increased past the 775 volts, based on the manufacturer's warning, it is unclear if a high enough voltage was not reached or if as Knoll warns, the carrier velocity became saturated at the higher voltages used. Because the crystal dimensions are small the resulting electric field is approximately  $7.75 \times 10^5$  volts/meter. Another factor that affects the validity of this method is the pulse selection from the RTD. The Fano factor describes the improvements seen from expected Poisson statistics. If the RTD is preferentially selecting pulses the data no longer represents the complete system and the statistics are affected. The RTD selection is expected to give an even greater improvement from the Poisson statistics resulting in a lower Fano factor.

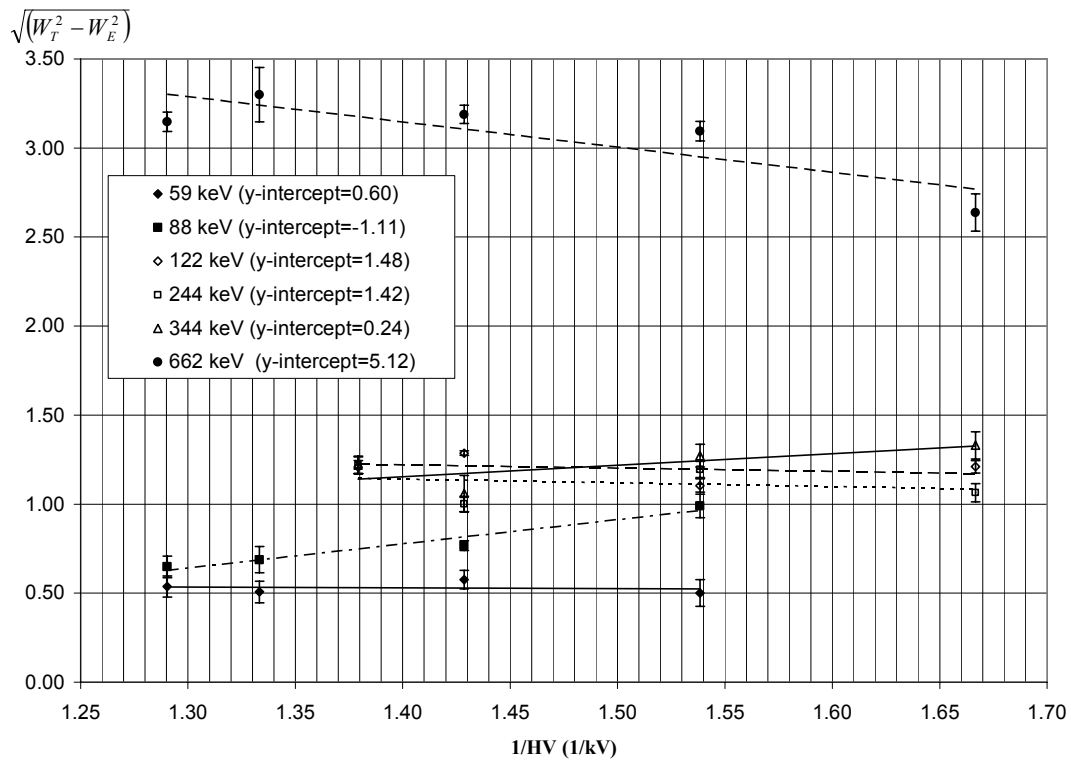


**Figure 30. Inverse high voltage bias versus FWHM plot**

**Table 5. Calculated Fano Factors from Figure 30**

Energy (keV)	Y-Intercept	Fano Factor
59	0.60	0.25
88	-1.11	NA
122	1.48	0.73
244	1.42	0.34
344	0.24	0.007
662	5.12	1.61

Knoll's description of the contributions of the FWHM for a lithium-drifted silicon detector, Si(Li), (Knoll, 2000: 466-467) was also used to describe the CdTe detector FWHM contributions. A linear response of the  $W_T^2 - W_E^2$  for gamma energies from 59 keV to 344 keV suggested that the contribution of  $W_D^2$  was dominant in this range. Fano factors were calculated for each series resulting in an average Fano factor of 0.205. The resulting contribution of  $W_X^2 = W_T^2 - W_E^2 - W_D^2$  is shown in Figure 31. The leakage current and incomplete charge collection contribution to the FWHM at 662 keV is approximately 2.8 keV.

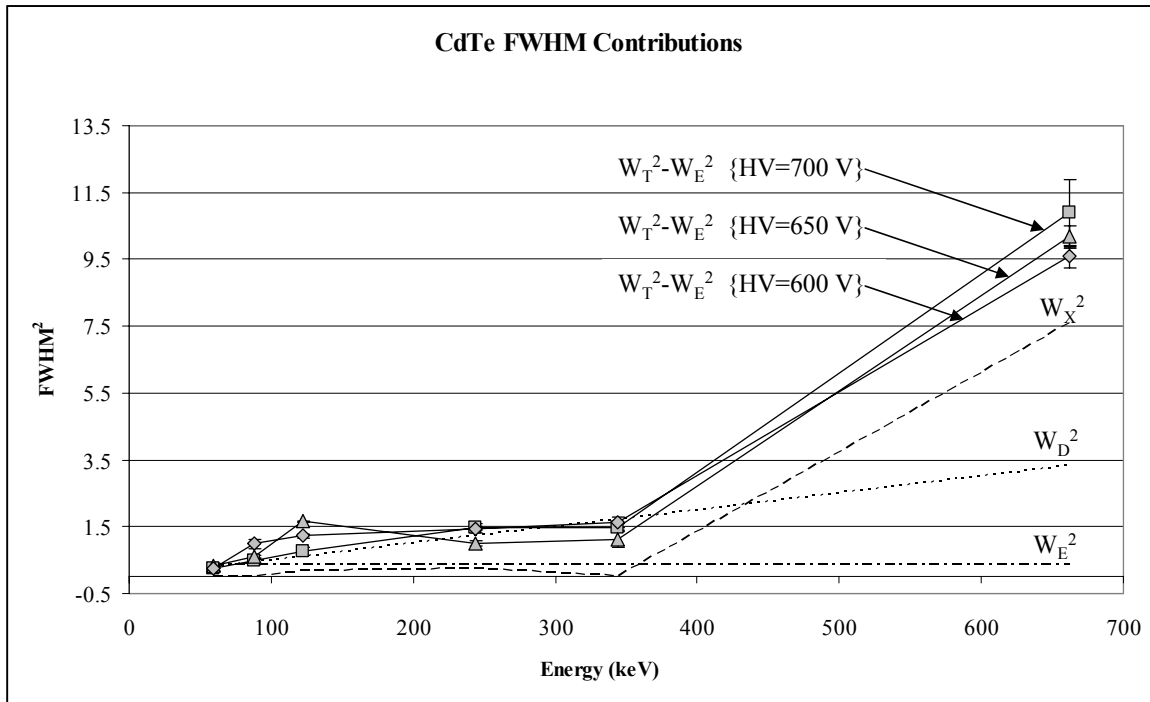


**Figure 31. Estimate of the FWHM contributions for the Amptek CdTe detector**



## NaI(Tl) Characterization

The NaI detector performance exceeded the manufacturer's specification. The resolution data is shown in Table 6 and Figure 32. A resolution of 6.7% at 662 keV was achieved using multinuclide source T108. The energy spectrum is located in Appendix O.

**Table 6. NaI(Tl) Resolution Data**

<b>Nuclide</b>	<b>Energy (keV)</b>	<b>FWHM (keV)</b>	<b><math>\sigma</math>(FWHM) (keV)</b>	<b>R (%)</b>
Co57	122.80	11.01	0.23	9.0
Ce139	165.91	15.08	0.44	9.1
Hg203	282.85	24.00	1.01	8.5
Sn113	382.18	30.19	1.51	7.9
Sr85	514.47	37.29	0.71	7.2
Cs137	661.76	44.18	0.18	6.7

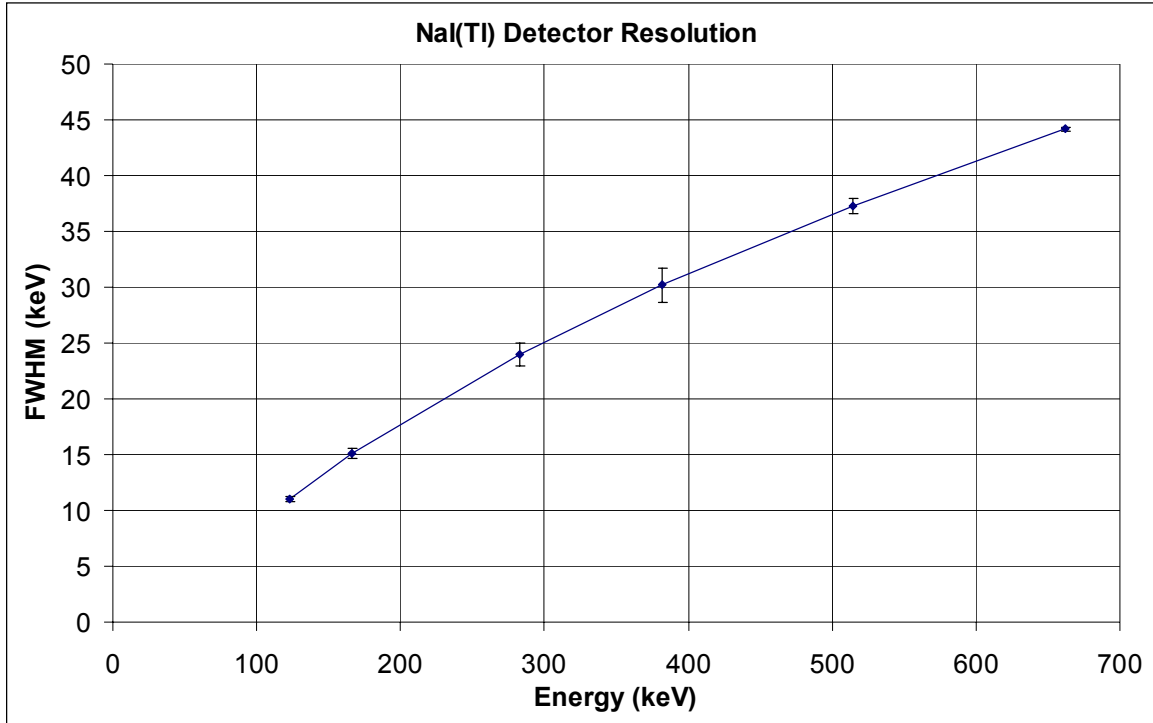


**Figure 32. NaI(Tl) FWHM versus gamma ray energy**

For an accurate measurement of the absolute and intrinsic efficiencies, the nearly mono-energetic sources of  $^{57}\text{Co}$  and  $^{137}\text{Cs}$  were used in the geometry shown in Figure 24. The absolute efficiency data is found in Table 7. The intrinsic efficiency data is found in Table 8. The intrinsic total efficiencies of 96.5% and 59.6% for 122 keV and 662 keV gamma rays respectively, were lower than shown in Knoll of 100% and 86% (Knoll, 2000: 337). These values are very dependent upon source-detector geometry and it is suspected that the values from Knoll consider additional factors such as the detector window material and source self-attenuation increasing the reported efficiencies. The 662 keV peak-to-total ratio of 0.42 was found to be reasonable compared to a reference value of 0.5 (Knoll, 2000: 338), further confirming the proper operation of the detector.

**Table 7. NaI(Tl) Absolute Efficiency Data**

<b>Energy (keV)</b>	<b>Total Absolute Efficiency (%)</b>	<b>Total Abs. Eff. Uncertainty (%)</b>	<b>Total Peak Efficiency (%)</b>	<b>Total Peak Eff. Uncertainty (%)</b>
122	1.00	3.2E-05	0.49	1.5E-05
662	0.62	1.5E-06	0.26	6.2E-07

**Table 8. NaI(Tl) Intrinsic Efficiency Data**

<b>Energy (keV)</b>	<b>Total Intrinsic Efficiency (%)</b>	<b>Total Int. Eff. Uncertainty (%)</b>	<b>Peak Intrinsic Efficiency (%)</b>	<b>Peak Int. Eff. Uncertainty (%)</b>
122	96.46	3.1E-03	46.89	1.5E-03
662	59.56	1.4E-04	24.99	4.1E-05

### **Compton System Geometry Effects**

The system was setup in the same configuration as used by Capt. Chris Williams (Williams, 2003: 117). A complete system drawing and labeled photograph is found in Appendix P. This section analyzes the effects of the geometry and clarifies any changes from the previous experimental work.

The effects of the initial collimator on the system resolution have been found to be significant and required detailed analysis. As shown in Figure 33, the 1.5mm radius collimator solid angle opens up at the detector to a field of view larger than the entire detector. It is important to understand the distribution of the source on the detector based on this geometry. The initial version of the *Mathematica* code discussed earlier, created the distribution shown in Figure 34. It was created by summing the solid angle subtended for each detector point by all points on the source. If the source was blocked by the

initial collimator, the detector point was not seen and no solid angle was added. As expected, the center of the detector is seen by all source points and has the largest distribution (white). The far corners of the detector are not seen by the entire source and therefore have the smallest distribution (black). This shows that the initial collimator, although not ideal, still provides some reduction in the angle variance between the source and the detector. It also reduces the scattering off nearby materials into the detector which add to the background noise. A smaller collimator hole would improve the desired alignment of the source and detector at the cost of further reducing efficiency.

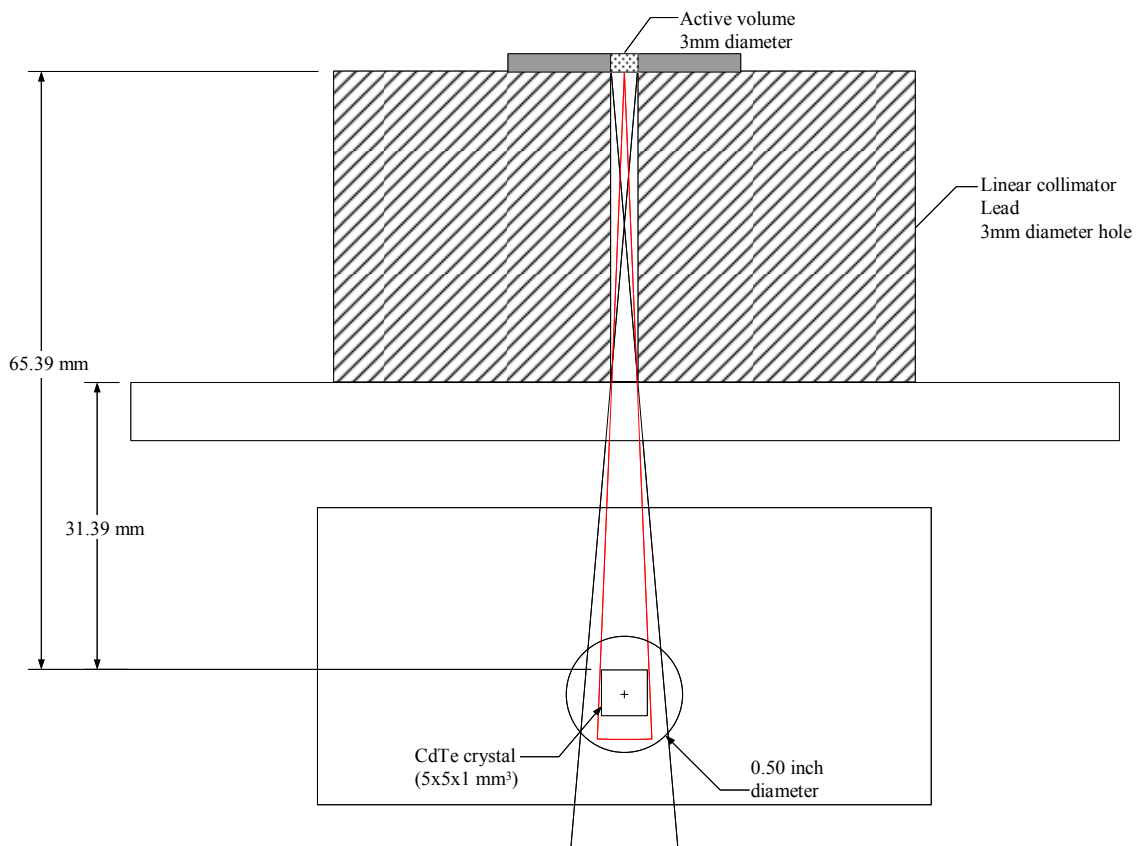


**Figure 33. Diagram of initial circular collimator and solid angle subtended by CdTe detector**

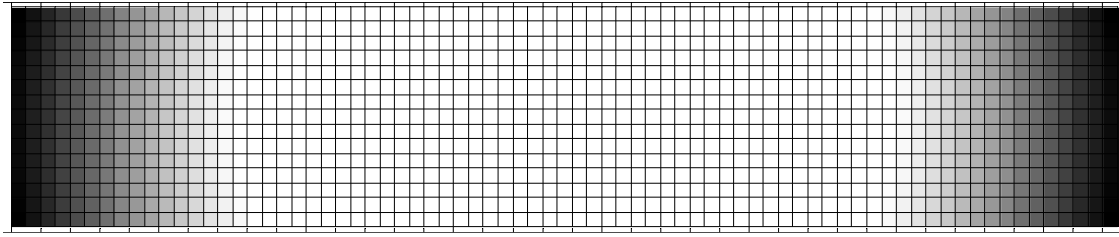


**Figure 34. Source distribution on CdTe 1 mm x 5 mm face from Position 2; white pixels represent largest distribution; black pixels represent smallest distribution**

Reduction in the conical collimator gap also affects the efficiency of the system by reducing the active detector volume in the CdTe. For the Compton spectrometer system to work, the conical collimator must be able to select only those gamma rays scattered at the desired angle. Using a similar iterative process as with the initial collimator calculations, the program analyzed every point in the detector to determine if it passed through the conical collimator gap to a point on the bottom plane of the collimator within the gap. Figure 35 shows the three dimensional output of the program representing the  $5 \times 5 \times 1 \text{ mm}^3$  detector volume. The larger points represent locations where there are a greater number of possible paths through collimator. As would be expected, a region in the detector that intersects with the apex of the collimator gap would have the most possible paths through.

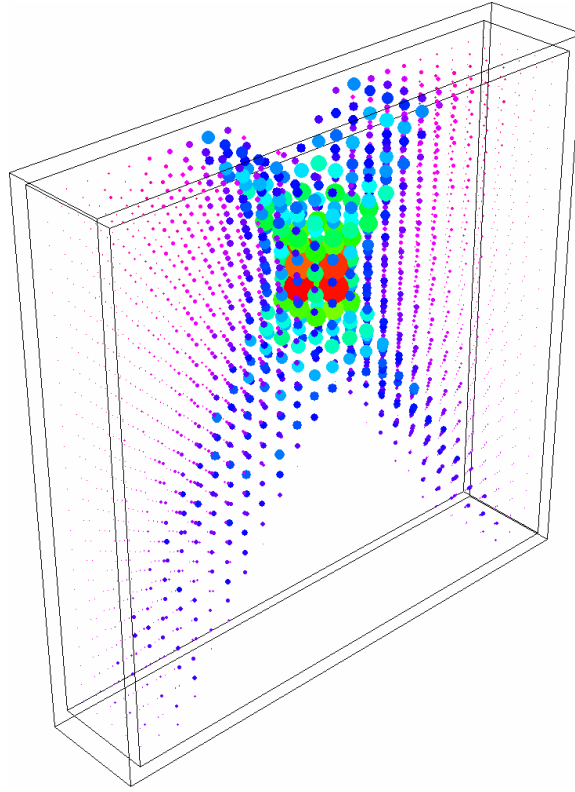


**Figure 35. Active volume of CdTe detector based on conical collimator geometry; larger circles represent a larger number of paths through the conical collimator gap with the largest occurring at the apex of the conical collimator**

The ratio of the number of points in the detector volume that can make it through the conical collimator to the total number of points in the detector is a good approximation to the active volume. In Figure 35 there are 2336 points that make it through, out of the 3125 total points giving a 74.8% usage of the active volume. The more refined the pixels of the detector and the pixels of the collimator, the more accurate the calculation will be.

Figure 35 suggests that the alignment of the conical collimator apex with the EEA detector volume will have significant affects on the Compton system. In order to

improve alignment and the consistency of experimental set up, the location of the CdTe crystal inside the detector housing was determined experimentally. A graduated scale attached to the detector housing was used to produce the count versus position graph shown in Figure 36. The detector, with the RTD on, was tested at eight locations each 1/32 inch (0.8 mm) apart. A collimated  $^{137}\text{Cs}$  beam with a 3 mm diameter was used. Based on the data, position 6 was taken as the detector location and used for the remainder of the experiment. This location corresponds to 1/8 inch in from the detector housing face and is in agreement with Amptek's detector dimensions (Amptek, 2004: 17).

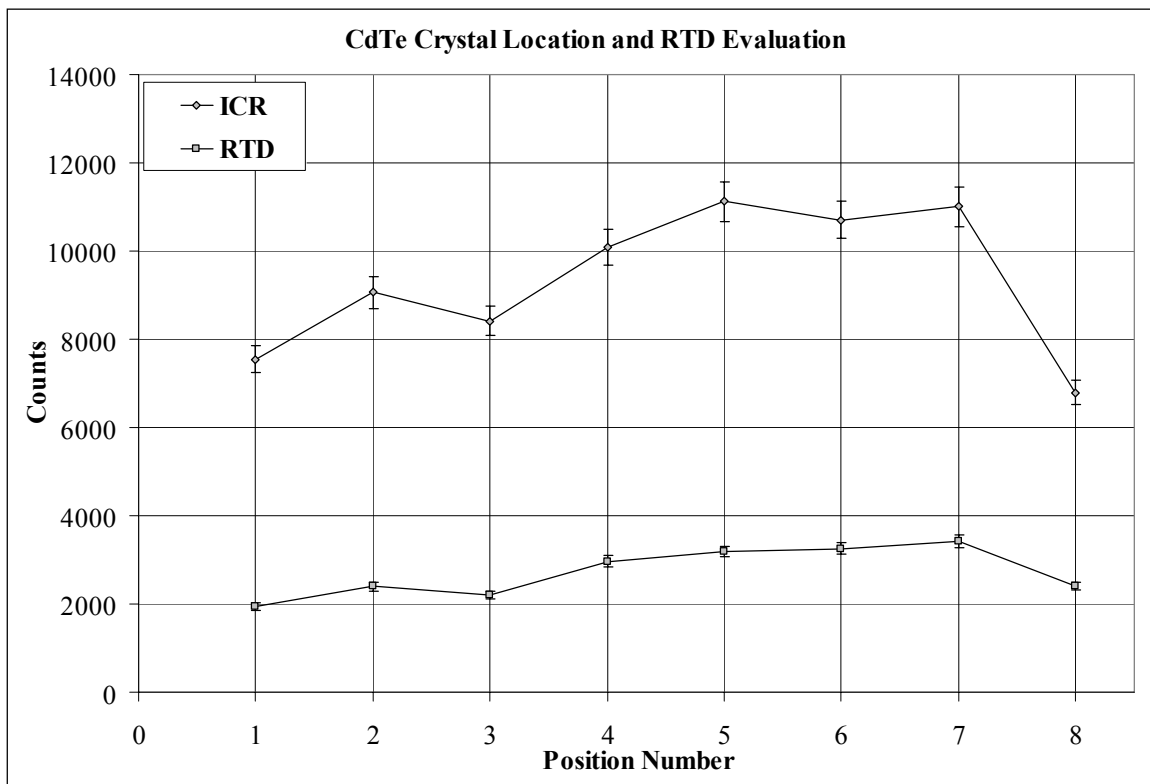


**Figure 36. CdTe crystal location and RTD evaluation; count rate from RTD and ICR as a function of the source alignment with CdTe graduated scale**

The ratio of the count rate from the RTD and the ICR was also used to evaluate the effects of the RTD on the active volume. The results in Figure 37 show the expected increase in the RTD/ICR ratio as the source is moved from position 1 to 8. As the source moves to the front edge of the detector, a higher count rate from the RTD is seen as the ICR begins to decrease. When the source is over position 6 a 70% reduction in detector volume is observed with the RTD active.

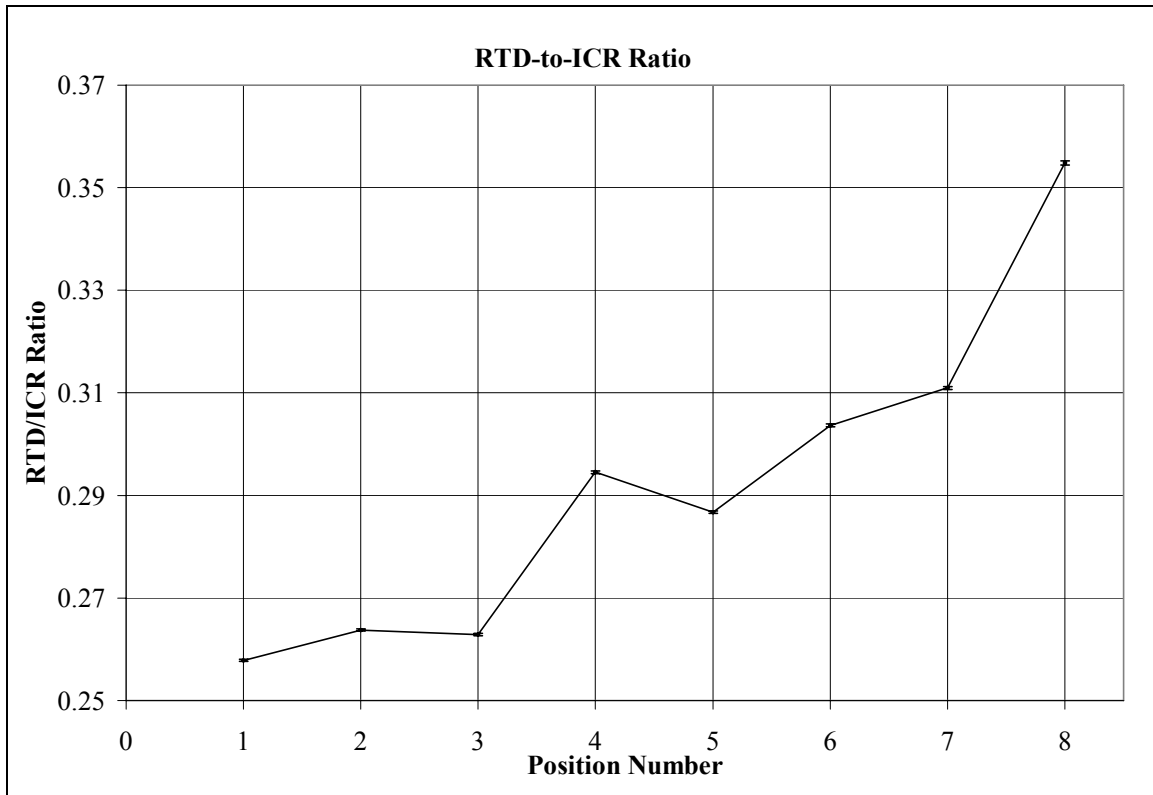


**Figure 37. RTD/ICR Ratio; determination of active RTD on detector volume**

### **Coincidence Electronics Evaluation**

The overlap method of coincidence was setup as follows. First, SCAs were used to produce logic pulses from the CdTe and the NaI(Tl) energy pulses based on their



arrival times as shown Figure 38. These pulses were initially aligned visually using the oscilloscope and the adjustable delay in the SCAs.

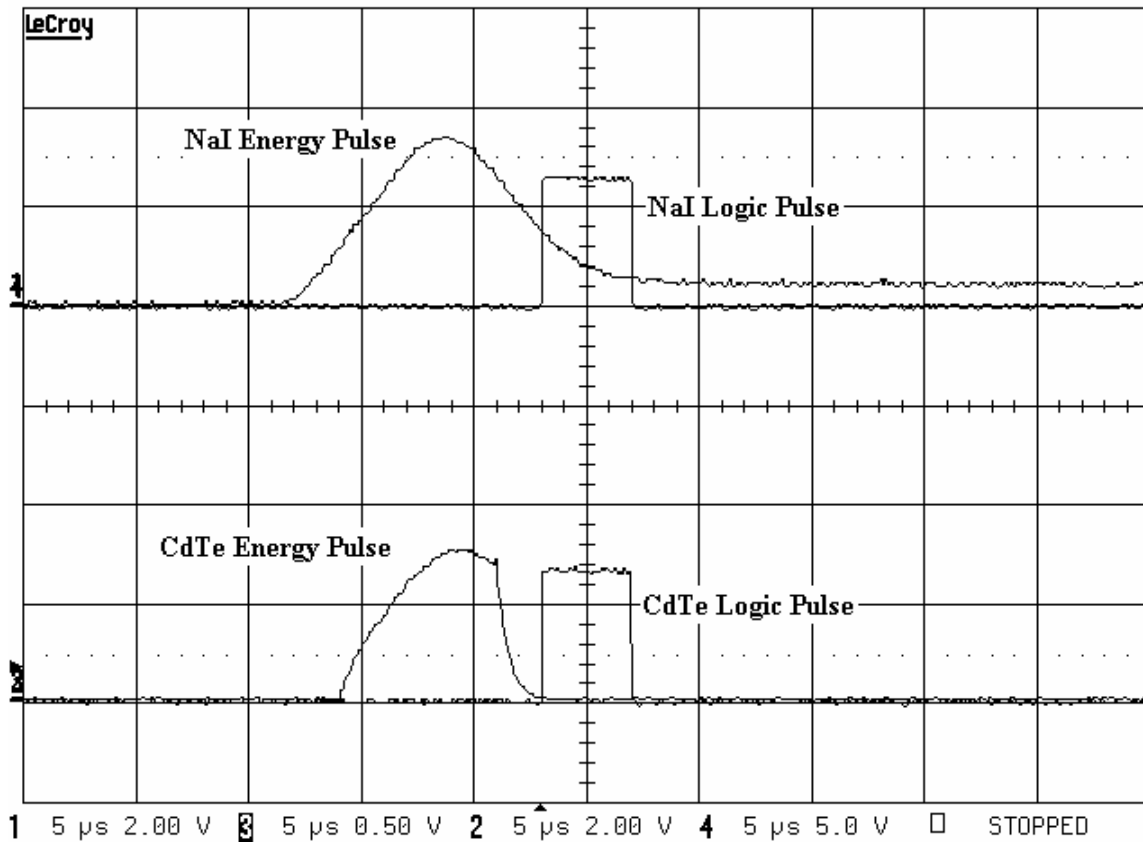


**Figure 38. Oscilloscope output-SCA logic pulse generated from EEA and PEA energy pulses**

These pulses were sent to GDGs for pulse width, height and delay adjustment. The GDGs outputs were then sent to the LGSC. The LGSC uses the pulse overlap method as shown in Figure 39. A logic pulse is produced in the region that the pulses overlap.

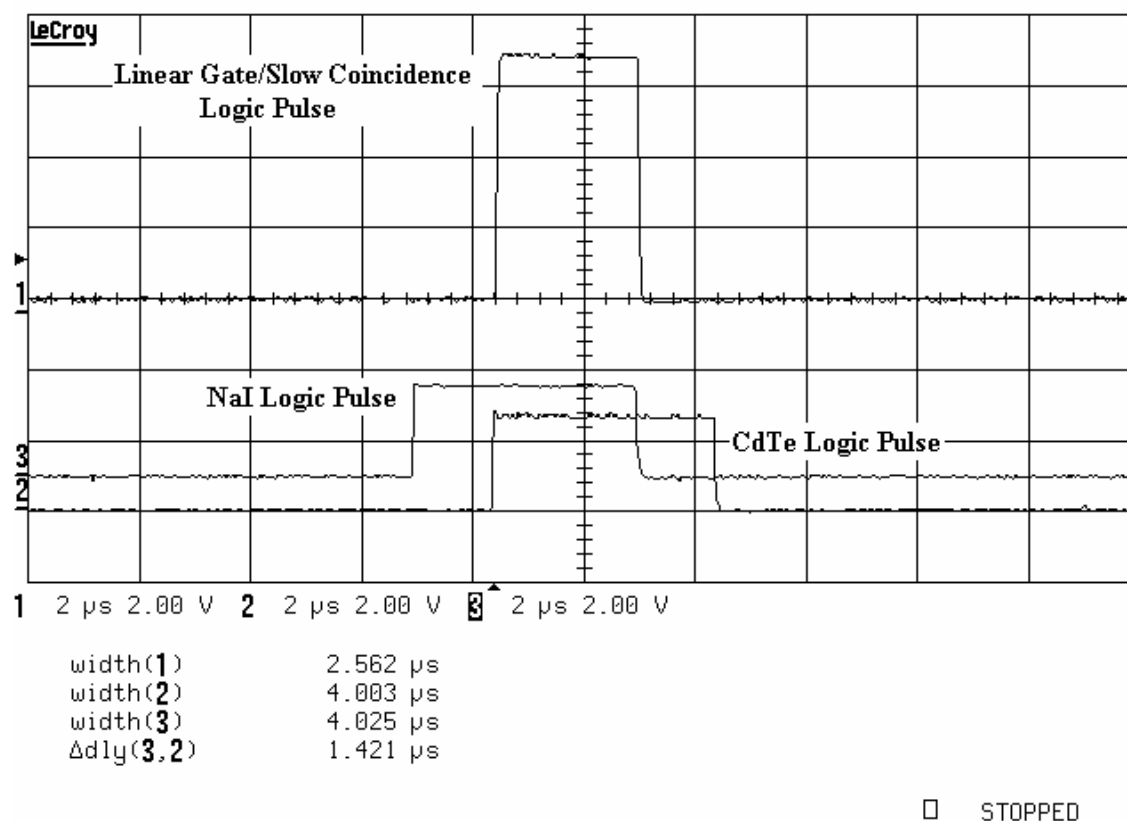
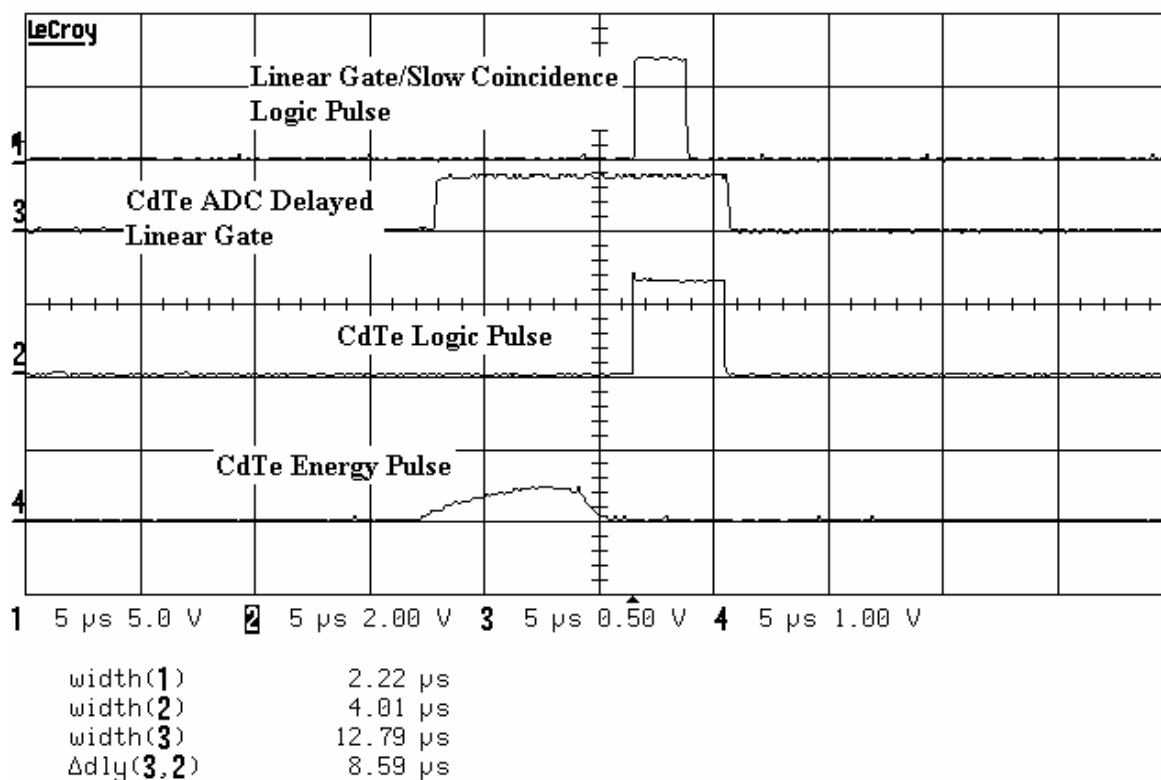


**Figure 39. Oscilloscope output-LGSC logic pulse created by coincident EEA and PEA timing pulses**

The LGSC output is then sent to the gate input of the ADC. The ADC produces a logic acceptance pulse when it receives a pulse to the ADC In. In the delayed mode, the acceptance gate can be extended past the end of the pulse going to the ADC In as shown in Figure 40. In coincidence mode the energy pulse is accepted when the gate in pulse overlaps the ADC delayed linear gate.



□ STOPPED

**Figure 40. Oscilloscope output-ADC delayed linear gate alignment with LGSC output**

The visual alignment was then refined by creating the delay curve shown in Figure 41.

The delay that corresponds to the highest counts is the optimized solution. The very low count rate seen makes the optimization less accurate. A similar process is used to establish the start-stop method.

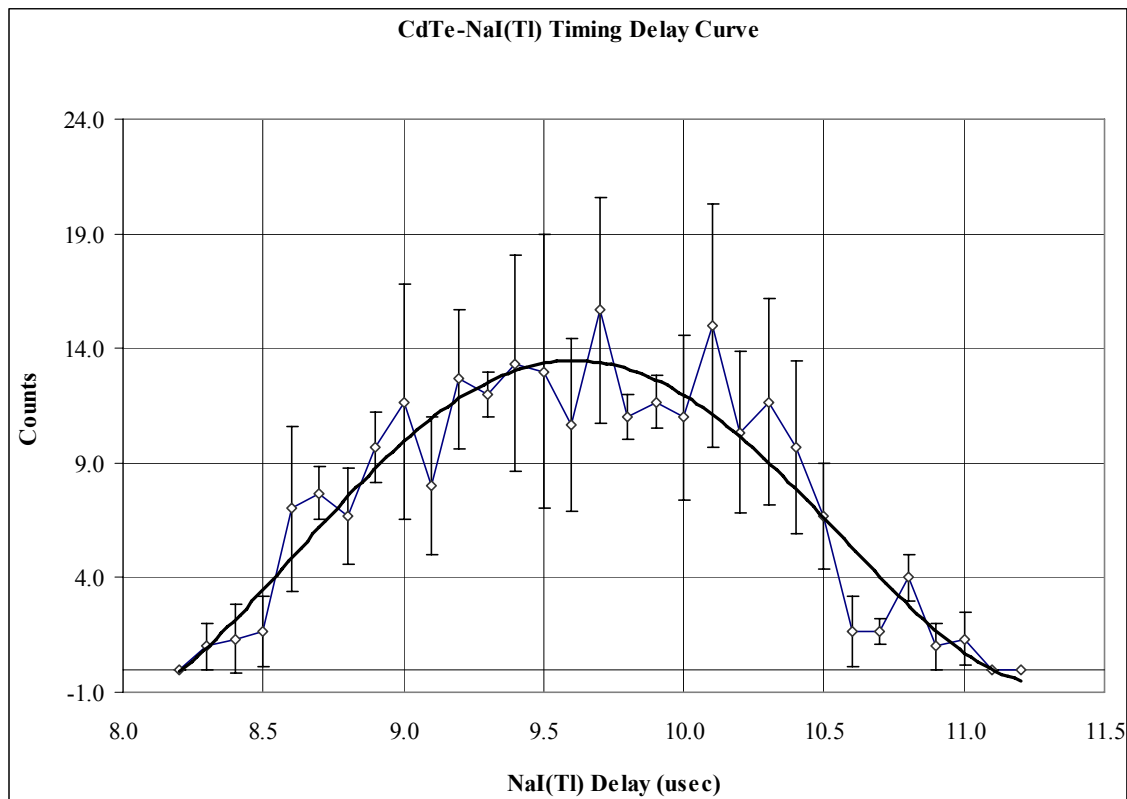


**Figure 41. Delay curve-counts versus adjustable delay to determine optimized alignment**

The TAC method produces a pulse with a voltage proportional to the timing between the EEA and PEA pulses that can be gated using a SCA as shown in Figure 42. The SCA output represents a coincidence event and is sent to the ADC gate in as described above. Because the only pulse timing requirement is the arrival of the stop pulse (PEA) after the start pulse (EEA), the TAC method does not require exact alignment of pulses. Both overlap and start-stop were used in the Compton spectrometer with similar results.

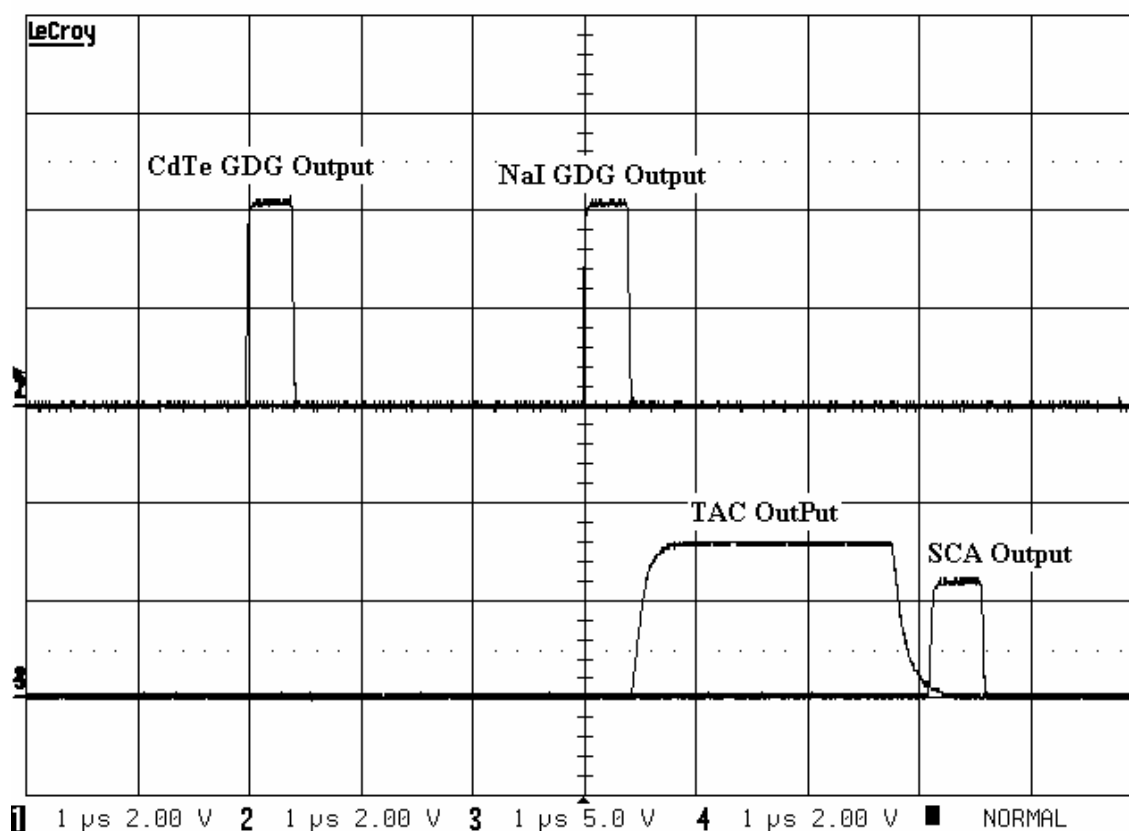


**Figure 42. Oscilloscope output using TAC method; time between CdTe and NaI(Tl) determines TAC output pulse height**

### Experimental Compton Spectrometer Energy Spectra

The experimental Compton spectrometer data collected was not the same as found during the previous research of Capt. Williams. Included for analysis are four spectra; a  $^{137}\text{Cs}$  pulse-overlap method, a  $^{137}\text{Cs}$  start-stop method, a  $^{22}\text{Na}$  start-stop method and the previous  $^{22}\text{Na}$  spectrum “smoothed”, shown in Figure 43, Figure 44, Figure 45 and Figure 46, respectively. The  $^{137}\text{Cs}$  spectra show the majority of counts roughly centered about 100 keV. This suggests that, to some extent, the second collimator is preferential to the scatter gamma rays corresponding to the collimators scatter angle. This is reinforced

with the  $^{22}\text{Na}$  spectrum centered roughly around 61 keV, the expected Compton electron energy from the 551 keV gamma ray. Although the spectra suggest that the counts collected are real, these spectra are in stark disagreement with the previous research which showed a high resolution peak near the expected energy of 100 keV. Although the cause of this discrepancy remains unknown computer simulation has provided some additional information.

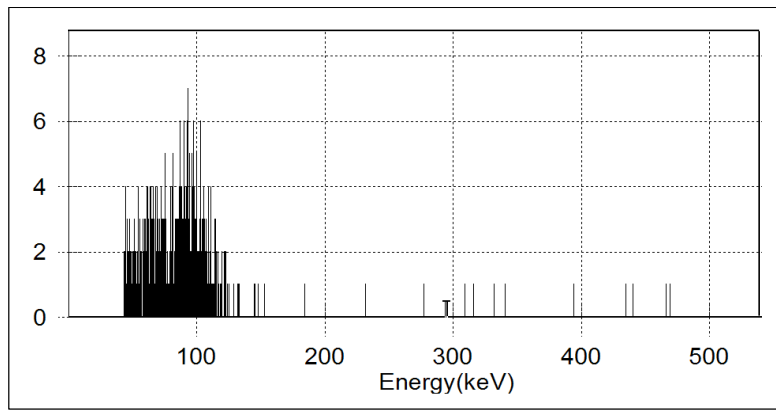


**Figure 43. 10-Hour Compton spectrometer spectrum- $^{137}\text{Cs}$  source using pulse-overlap method**

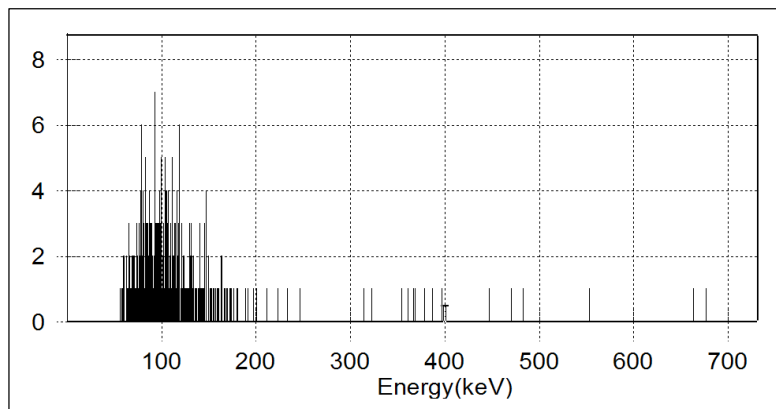


**Figure 44. 10-Hour Compton spectrometer spectrum- $^{137}\text{Cs}$  source using start-stop method**

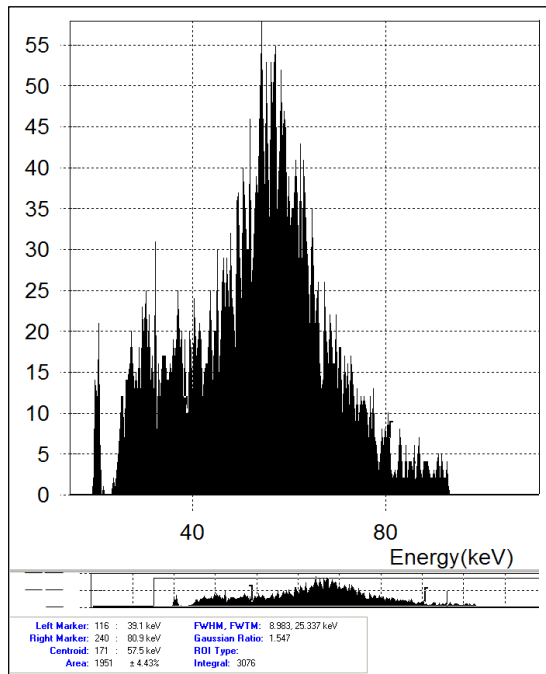


**Figure 45. 74-Hour Compton spectrometer spectrum- $^{22}\text{Na}$  source using start-stop method**

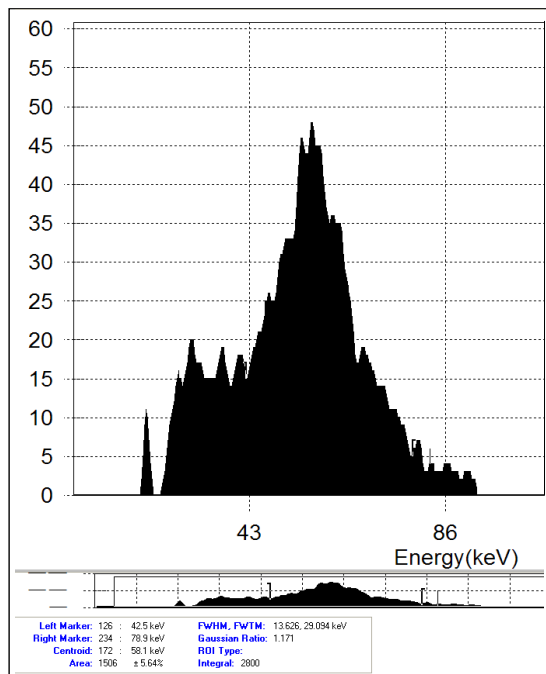


**Figure 46. 13 point smoothed 74-Hour Compton spectrometer spectrum- $^{22}\text{Na}$  source using start-stop method**

## Simulated Compton Spectrometer Energy Spectra

The *Mathematica* code written to simulate the operation of the Compton spectrometer was executed for a wide variety of geometric scenarios for verification of the code's performance, for comparison with experimental data and for determining what geometries would meet the requirements of this project. The geometric parameters analyzed for effects on system resolution and efficiency were the initial collimator radius, the conical collimator gap, and the detector dimensions and location relative to the conical collimator apex.

The simulated spectra below represent counts versus gamma ray energy for 1-hour collections using the combined  $^{137}\text{Cs}$  source. It is also assumed that the NaI(Tl) has a 25% peak intrinsic efficiency which represent the effects of using an energy gate on the PEA since coincident events are counted only if the scattered gamma ray is fully absorbed in the PEA. Although many plots will show very low and often fractional counts, the 1-hour collection time was used throughout to facilitate efficiency comparisons from one system geometry to the next. Because the effects on resolution and efficiency are dependent on the ratios of the geometric parameters, the comparisons below are used to evaluate specific system geometries and attempts only very broad classification of these effects.

First, the simulation verified the expected reduction in the FWHM and efficiency associated with reducing the conical collimator gap. The simulation predicted a 19% reduction in FWHM with an 81% reduction in efficiency with a reduction in the gap from



1.0 mm to 0.5 mm as shown in Figure 47 and Figure 48. This disproportionate reduction shows that the high concentration of available paths through the conical collimator from the apex area is the main contribution to variance in angles and therefore to FWHM. This conclusion is further substantiated when evaluating the variation in detector location relative to the conical collimator apex. Next, the simulated reduction of the initial collimator radius from 1.0 mm to 0.25 mm resulted in a 50% reduction in FWHM and 61% in efficiency. Shown in Figure 49, this significant reduction in initial radius changes the distribution in Figure 34 to a small region of high distribution at the center of the detector face. The predicted FWHM of 4.6 keV demonstrates that reducing the initial collimator alone will not provide the resolution needed. The surprising result of an increased FWHM was found when the detector width was reduced from 0.5 mm to 0.3 mm. The expected result was a reduction in the FWHM because of a decreased scatter angle distribution and a reduced efficiency because of a reduced detector volume. The small increase in the FWHM shown in the comparison of Figure 47 and Figure 50 is a result of a larger relative reduction in efficiency, and consequently a lower half maximum, without a significant reduction in angle distribution. This effect demonstrates the significant dependence on the ratios of the geometric parameters as this effect would not be seen with an initial collimator of a smaller radius.

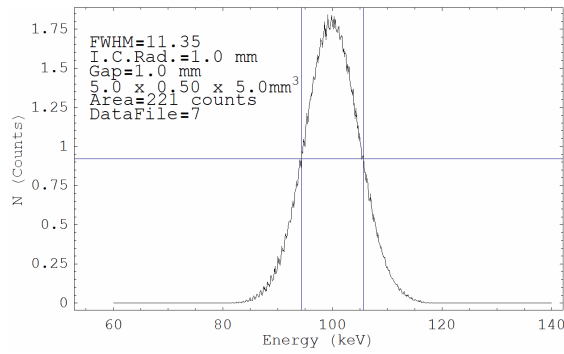


**Figure 47. Simulated Compton spectrometer spectrum - conical collimator gap=1.0 mm**

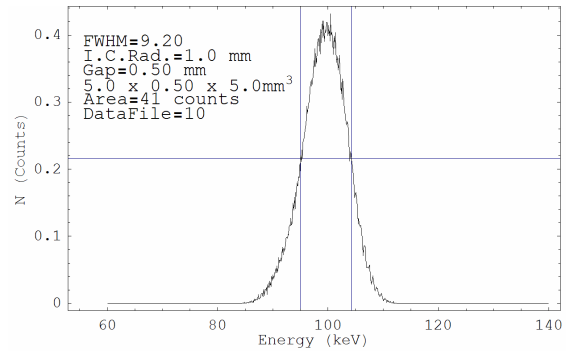


**Figure 48. Simulated Compton spectrometer spectrum - conical collimator gap=0.5 mm**

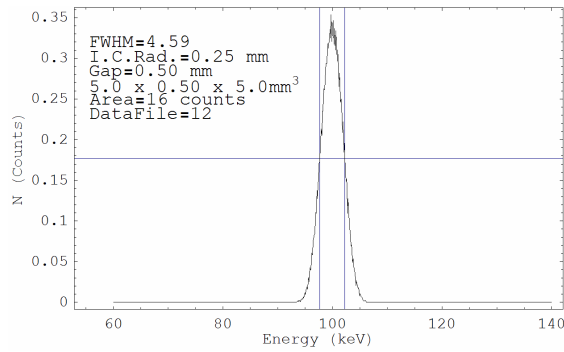


**Figure 49. Simulated Compton spectrometer spectrum - collimator radius=0.25 mm**

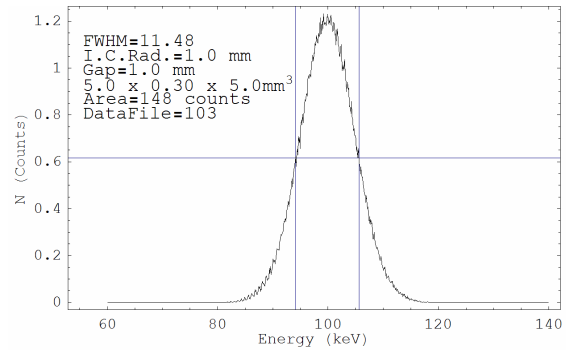


**Figure 50. Simulated Compton spectrometer spectrum - detector width=0.3 mm**

The effects of detector location relative to the conical collimator apex is explored in Figure 51, Figure 52, and Figure 53; representing the apex just above the top of the detector, in the center of the detector and just below detector, respectively. Moving the apex out of the detector volume decreased the FWHM by 50% for both above and below the detector. As mentioned above, the high concentration of available paths through the

conical collimator from the apex area is the main contribution to the FWHM. As the center of the “X” distribution, shown in Figure 35, moves above or below the detector, respectively only the “legs” or “arms” of the distribution remain in the detector volume. These portions of the distribution have a smaller angle variance because they are limited to scattering through only a portion of the collimator. The scatter angles associated with the “legs” are smaller and as expected the peak in Figure 51 is shifted below 100 keV. The “arms”, on the other hand, have larger scatter angles and the peak in Figure 53 is shifted above 100 keV. The predicted results with the apex above and below the detector showed similar reductions in FWHM and efficiency. Therefore moving the apex above the detector would be preferred because of the improved resolution associated with collecting the lower-energy Compton electrons.

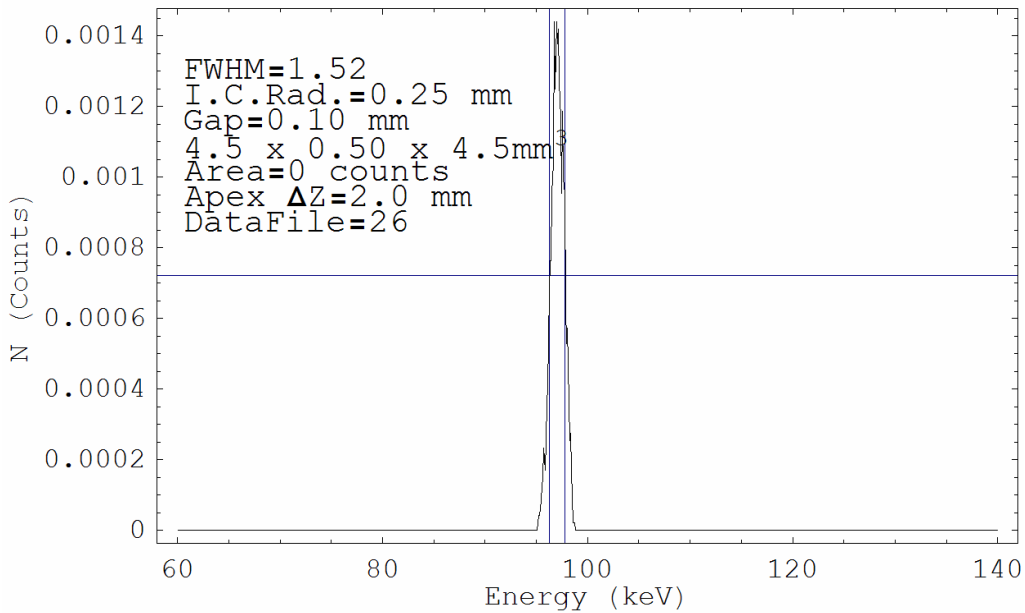


**Figure 51. Simulated Compton spectrometer spectrum - detector location=2.0 mm**

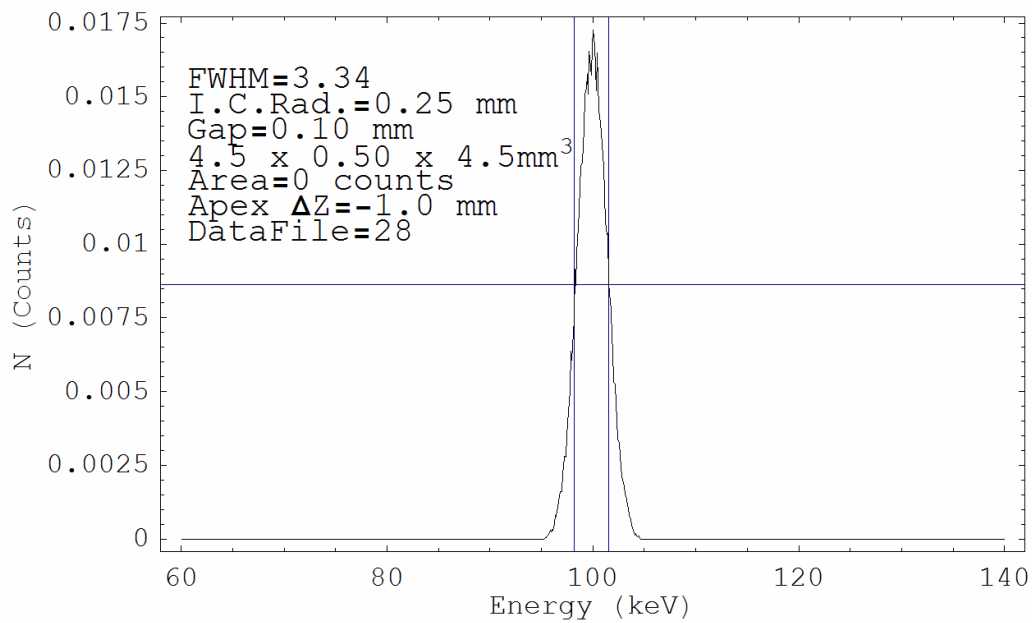


**Figure 52. Simulated Compton spectrometer spectrum - detector location=-1.0 mm**

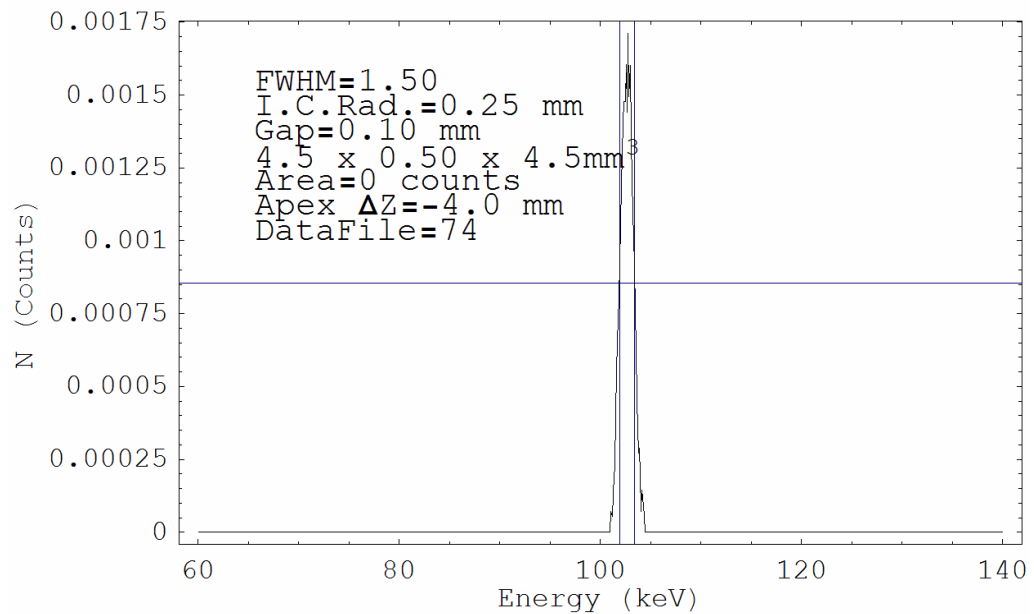


**Figure 53. Simulated Compton spectrometer - detector location=-4.0 mm**

Using the geometry of the experimental system, a FWHM of 13.0 keV was found as shown in Figure 54. This value is approximately 15 keV better than an estimated experimental value from Figure 43 and 12 keV worse than previous research values. The simulated one hour spectrum using the combined  $^{137}\text{Cs}$  source predicted 130 counts under the curve. Current experimental data had 305 counts under the curve in a 10-hour spectrum. Previous experimental data had 435 counts under the curve in a 1-hour spectrum.

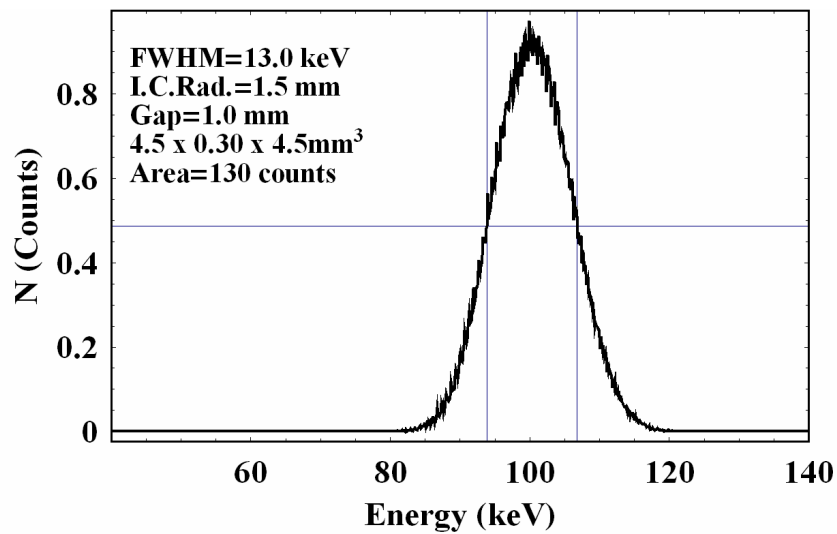


**Figure 54. Simulated 1-hour Compton system spectrum using combined  $^{137}\text{Cs}$  source showing counts versus energy**

The program was also used to produce a 1-hour  $^{22}\text{Na}$  spectrum shown in Figure 55 for comparison with experimental results shown in Figure 45 and Figure 46. First it is important to note that the simulation demonstrated the natural improvement in resolution due to the reduced gamma ray energy of 511 keV. For example, using a range of  $\theta$  as 0.51 to 0.55 radians in Equation 2, the Compton electron energy has a range of 12.5 keV

for an incident gamma ray of 662 keV and only 8.0 keV for a 511 keV incident gamma ray. The *Genie* software found a 9 keV FWHM for the unsmoothed spectrum and 13.6 keV for the 13-point smoothed spectrum compared to the simulation FWHM of 8.3 keV. The small improvement in agreement is attributed to a higher activity source, longer collection time and tighter energy requirements in the PEA. There remains a strong disagreement with predicted and measured efficiencies. The total count measured in a 74-hour period was 3106, while the simulation predicted 23236 in the same amount of time. The disagreement in efficiency is because the simulation does not take into consideration the reduced efficiency of the NaI(Tl) in the Compton spectrometer configuration.

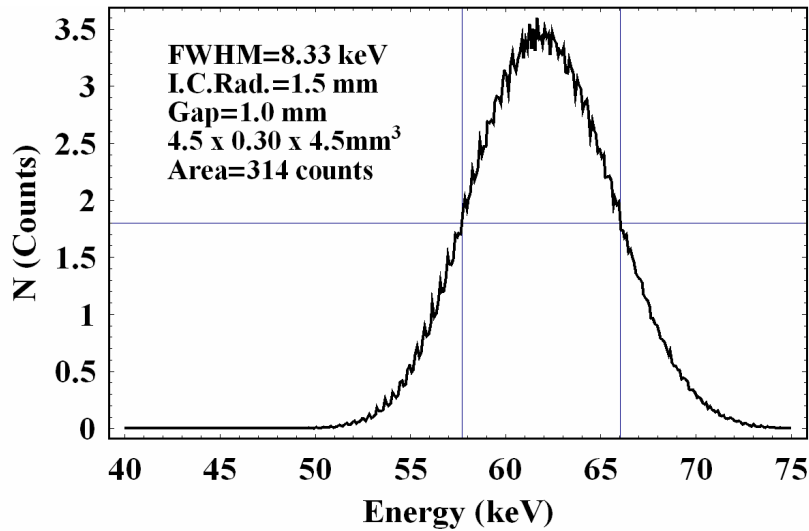


**Figure 55. Simulated 1-hour Compton system spectrum using 60  $\mu$ curie  $^{22}\text{Na}$  source showing counts versus energy**

In the Compton spectrometer configuration only a small portion of the NaI(Tl) crystal is intersected by the path through the conical collimator. In the characterization of

the NaI(Tl) detector a peak efficiency of 25% was found using the entire detector volume with the incident gamma rays nearly normal to the detector face. The resulting linear distance through the detector is approximately three inches. In the Compton spectrometer configuration the gamma rays enter the detector at a  $30^\circ$  angle resulting in a one inch linear distance through the crystal. Because peak events correspond not only to direct photoelectric absorption events but also Compton events followed by photoelectric absorption, it is difficult to accurately estimate the reduction in efficiency based on the linear distance through the crystal. The reduction of Compton events followed by photoelectric absorption will be greater than the reduction in the direct photoelectric events; therefore a one third reduction is conservative. This efficiency correction would decrease the simulation prediction of 23236 counts to less than 7700 counts.

Although simulation and experimental results are not explicitly linked, there remains value in using the program to determine what geometric parameters are needed to achieve the required resolution set forth at the start of this research. A FWHM of 0.533 keV was achieved for a system geometry of 0.25 mm initial collimator radius, 0.10 mm conical collimator gap, detector dimensions of  $4.5 \times 0.3 \times 4.5 \text{ mm}^3$ , and raising the conical collimator 2.5 mm closer to the detector. The spectrum, shown in Figure 56, required a 200 curie source counted for one hour to acquire 150 counts under the curve. This geometry uses the “legs” of the detector volume “X” distribution and therefore the peak is shifted down to approximately 96 keV.

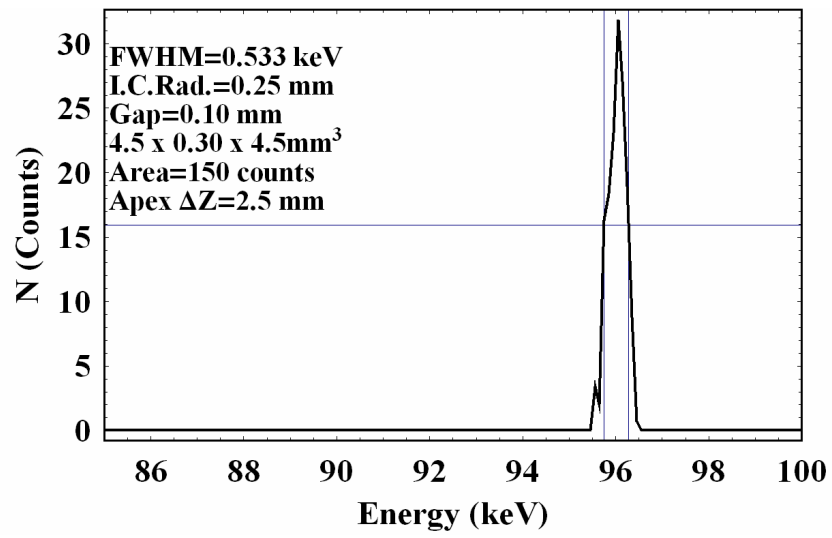


**Figure 56. Simulated 662 keV spectrum with required resolution**



## **VI. Conclusions and Recommendations**

### **Conclusions of Research**

Three investigated questions were used to focus the research of this thesis and are answered here.

1. Can the previous results be reproduced? I was not able to reproduce the results of the previous research. This clearly marks these finding for skepticism and raises many more questions. The important question is which results more closely represent the actual characteristics of the detector system? I start my argument in support of my results based on the simple fact of geometric calculations. The rough, two-dimensional calculations of the system produce a FWHM of approximately 14 keV. This calculation does not take into consideration the contributions to FWHM from the detector and electronics and therefore is a best case scenario. My experimental results, although not decisive, have general characteristics that are similar to those expected. The previous results are significantly better than expectations. There are some possible solutions for this improvement such as a non-perpendicular alignment of the initial collimator to the conical collimator or an improved collimation of the source due to misalignments of the source, initial collimator and/or detector volume. Currently no reason has been verified.

2. How does the energy gating affect the Compton Spectrometer? The main effect of adding the energy gate to the PEA is a further reduction in efficiency. The NaI(Tl) detector is chosen for its very high efficiency to ensure that a minimal number of true coincident events are lost because of failure of the scattered gamma ray to interact in the

PEA. The purpose of the energy gate is to suppress events that are due to other sources outside the energy window of interest and to further reduce accidental coincidence. This requires a better knowledge of the scattered gamma ray energy. The energy gate selects a window around the range of full-energy peaks of the scattered gamma rays of interest. The efficiency of the NaI(Tl) is reduced from its total intrinsic efficiency to the peak intrinsic efficiency. For 662 keV gamma rays this was found to be a reduction from 60% to 25%. The efficiency is further reduced by a factor of at least 1/3 because of the reduction in the amount of NaI(Tl) crystal intersecting the path of the conical collimator.

3. Can modeling the Compton spectrometer help with future design? Yes, modeling of the system is useful for evaluating new system designs before construction. The interdependence of the geometric parameters is not always clear and modeling can identify unexpected geometric dependence before new systems are constructed. With specific resolution and efficiency requirements a system design can be evaluated for feasibility.

### **Recommendations for Action**

Research of the Compton spectrometer should continue for several reasons. First, real world applications require the type of resolution this thesis tried to achieve. The concepts of the system are well understood and there are many alternative designs that can be researched to overcome the major disadvantage of efficiency. Second, the discrepancy with previous experimental data must be further researched to truly evaluate the Compton spectrometer system. Lastly is the educational benefit for future students.

This thesis covered a large portion of the nuclear engineering curriculum and was a great way to tie this educational experience together.

### **Recommendations for Future Research**

As mentioned above, the major disadvantage of the system is efficiency. Further research should focus on overcoming this shortcoming. There are several possible avenues that can be evaluated. The previous research of Capt. Williams used a two-angle collimator to increase efficiency while maintaining only one PEA to collect the scattered gamma rays. Multiplexing the scattered angles is essential to increasing efficiency, but requires a method to distinguish absorption in each angle separately. Conical collimators can be created with scintillation material with each conical volume separated by a reflective material.

The research should also include improving the computer simulation. There are two main areas that can be further developed. First, the fidelity of the simulation is currently limited to the selected “pixel size” of each component. This limitation can be reduced by writing the program in FORTRAN or other similar program with a more advanced compiling system. The simulation could also be easily adapted to a Monte-Carlo method that would not have the dependence on “pixel size.” Second, the program requires the flexibility to evaluate off-alignment system configurations. Currently, the program is written so that changes to geometric parameters do not affect the vertical alignment of the system. Off-alignment simulations would be valuable to assess the sensitivity of that parameter and determine design specifications.

## Appendix A: $^{239}\text{Pu}$ and $^{240}\text{Pu}$ Spectra

The following energy spectra demonstrate the complex characteristics of plutonium samples. The plots were produced by the Idaho National Engineering and Environmental Gamma Ray Spectrometry Center's Online Catalogue (IINEE).

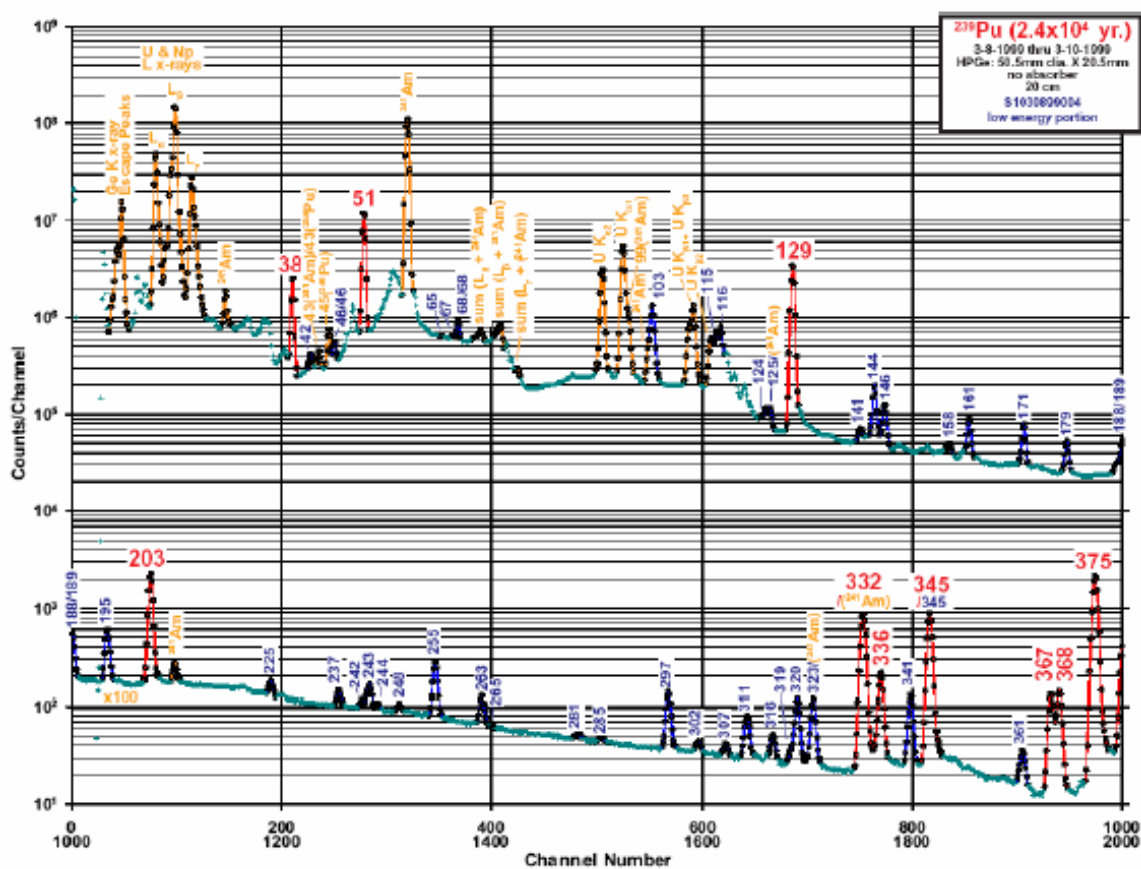


Figure 57.  $^{239}\text{Pu}$  Energy spectrum 0-400 keV, (INEE,1999)

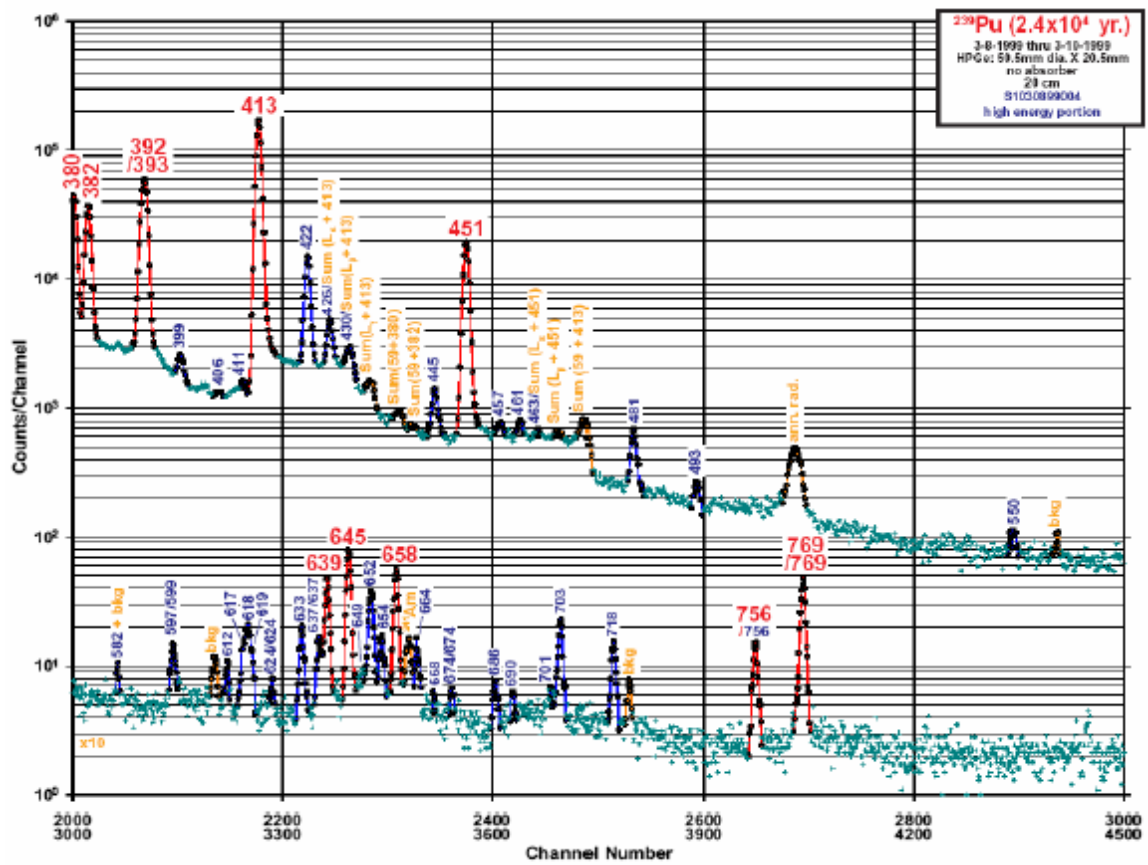
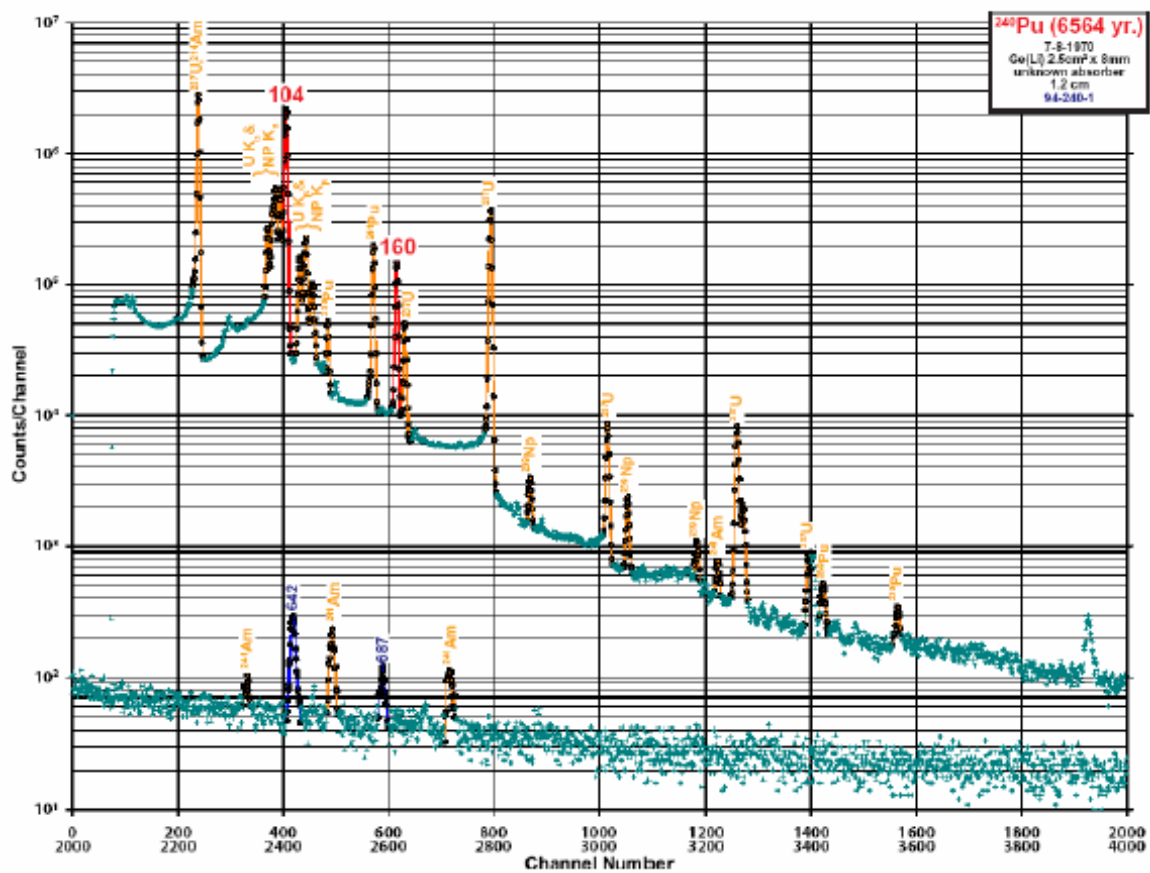


Figure 58.  $^{239}\text{Pu}$  Energy spectrum, 400-800 keV (INEE,1999)



## Appendix B: Summary of Previous Experimental Findings

The following provides a summary of Capt. Williams' experimental findings published in *Plutonium Isotopic Ratio Determination Using Compton Spectrometer System*.

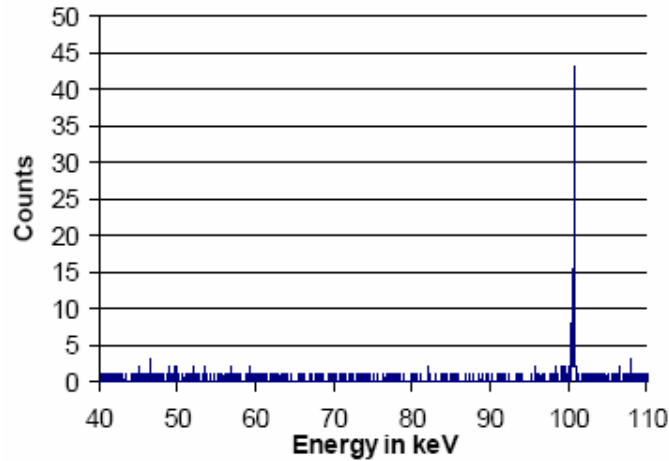
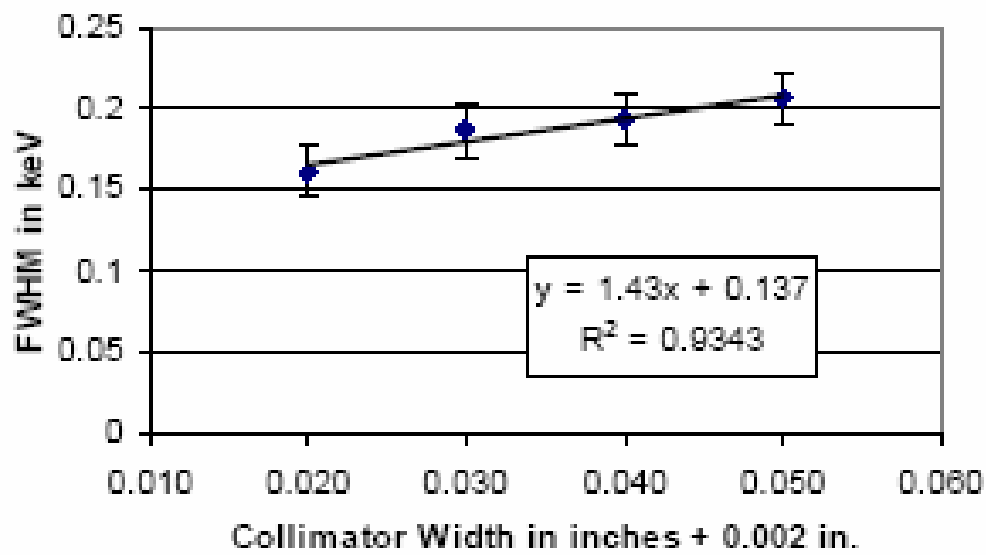


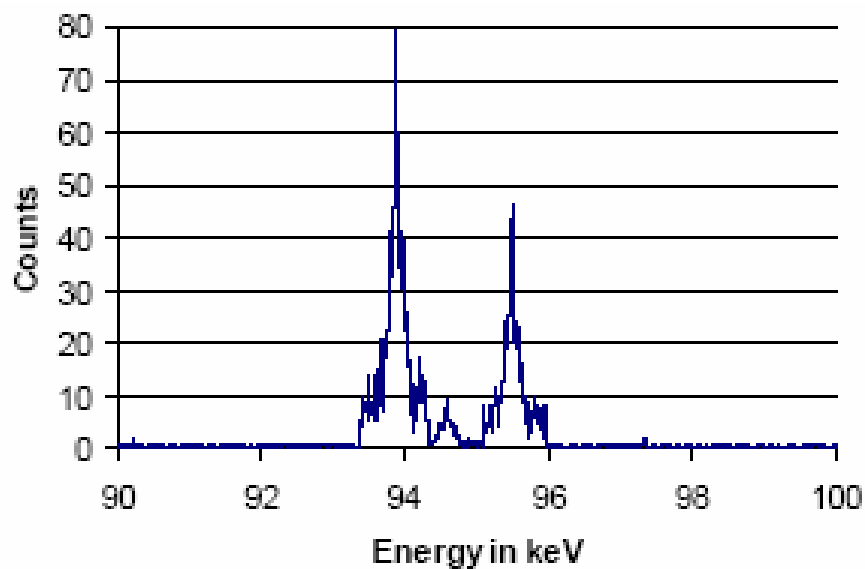
Figure 60. One-hour single collimator Compton spectrometer spectrum, channel width  $0.050 \pm 0.002$  inch (Williams, 2003: 80)

Table 9. Spectral data from Compton spectrometer (Williams, 2003: 81)

Collimator	Geometry	Max Counts	Channel Number	Energy in keV	Area Counts	Integral Counts	FWHM in keV	FWTM in keV
Single Angle Channel in inches	$0.050 \pm .002$	43	6526	100.753	$481 \pm 23.7$	514	0.194	0.629
	$0.050 \pm .002$	48	6530	100.831	$499 \pm 24.5$	552	0.213	0.644
	$0.050 \pm .002$	44	6525	100.734	$530 \pm 25.5$	578	0.213	0.648
	$0.040 \pm .002$	38	6535	100.928	$439 \pm 23.5$	491	0.194	0.638
	$0.040 \pm .002$	32	6530	100.831	$425 \pm 21.1$	432	0.194	0.622
	$0.040 \pm .002$	37	6536	100.947	$442 \pm 22.1$	502	0.194	0.644
	$0.030 \pm .002$	34	6526	100.753	$263 \pm 22.3$	386	0.213	0.622
	$0.030 \pm .002$	33	6526	100.753	$367 \pm 21.8$	423	0.174	0.621
	$0.030 \pm .002$	31	6529	100.811	$389 \pm 20.2$	473	0.174	0.638
	$0.020 \pm .002$	28	6530	100.831	$277 \pm 22.7$	365	0.136	0.644
	$0.020 \pm .002$	31	6527	100.773	$255 \pm 23.5$	301	0.174	0.638
	$0.020 \pm .002$	27	6529	100.811	$298 \pm 26.1$	381	0.174	0.638



**Figure 61. Plot of average FWHM from 100 keV peak using Compton spectrometer (Williams, 2003: 85)**



**Figure 62. Simulated wgPu spectrum using Compton spectrometer (Williams, 2003: 96)**



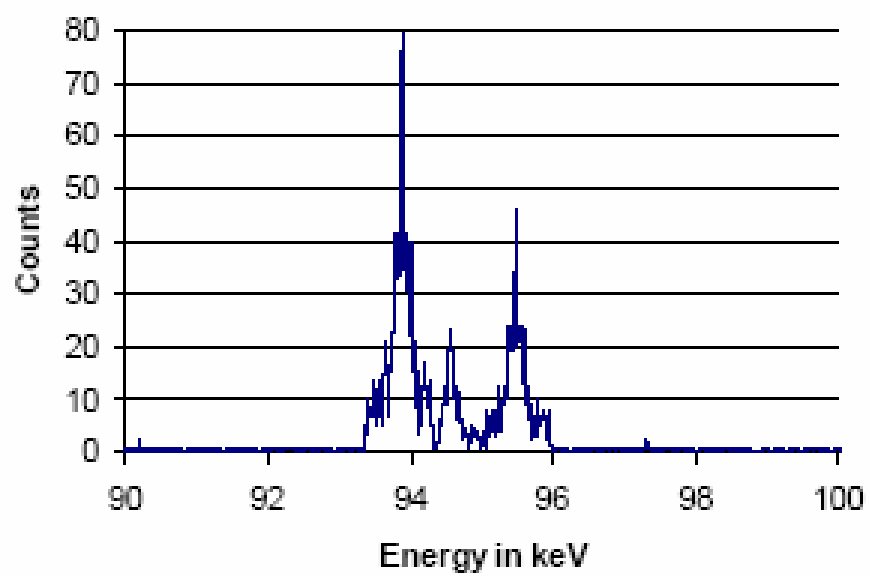


**Figure 63. Simulated rgPu spectrum using Compton spectrometer (Williams, 2003: 96)**

## Appendix C: Klein-Nishina Approximation Evaluation

The Klein-Nishina formula is used in the system simulation code to determine scatter probabilities inside the EEA; therefore an understanding of the limitations of this approximation is necessary. Comparison calculations of the Klein-Nishina formula to an empirical formula (Massaro and Matt, 1986: 545-547) and to XMuDat (Nowotny, 1998) follow.

Klein-Nishina calculations:

```

ACd = 112.411 ;
ATe = 127.60 ;
ZCdTe = 100 ;
ρCdTe = 6.06 (*Density from Knoll *) ;
NCdTe =  $\frac{6.02214 \times 10^{23}}{(A_{Cd} + A_{Te})}$  ;
r0 = 100 * 2.817940285 * 10-15;
KN[θ-, z-, hv-] =
  z r02  $\left( \frac{1}{1 + \alpha[hv] (1 - \cos[\theta])} \right)^2 \left( \frac{1 + \cos[\theta]^2}{2} \right) \left( 1 + \frac{\alpha[hv]^2 (1 - \cos[\theta])^2}{(1 + \cos[\theta]^2) (1 + \alpha[hv] (1 - \cos[\theta]))} \right)$ ;
CdTe_KNDat = TableForm [Table [{x, NCdTe 2 π NIntegrate [KN[θ, ZCdTe, x] * Sin[θ], {θ, 0, π}]}],
  {x, 10, 1000, 10}], TableHeadings → {None, {"γ (keV)", "σ (cm2/g)"}]}

γ (keV)      σ (cm2/g)
100           0.123636
200           0.101991
300           0.0886846
400           0.0794585
500           0.0725551
600           0.0671181
700           0.062678

```

Empirical formula calculations (Massaro and Matt, 1986: 545-547):

$$p[Z_] = Z \cdot 6652 \cdot 10^{-28};$$

$$a_1 = 2.0603;$$

$$a_2 = 1.1691 \cdot 10^{-1};$$

$$b_1 = 5.9973;$$

$$b_2 = 2.9267;$$

$$b_3 = 8.2038 \cdot 10^{-2};$$

$$c_1 = \frac{61.74 + 65.174}{2}; \quad (*cd: 61.714, Te: 65.174 *)$$

$$c_2 = \frac{7.7822 \cdot 10^2 + 5.5160 \cdot 10^2}{2}; \quad (* Cd: 7.7822 \cdot 10^2, Te: 5.5160 \cdot 10^2 *)$$

$$K = \frac{32.736 + 35.66}{2}; \quad (* Cd: 32.736, Te: 35.660 *)$$

$$cs[EE_, Z_] = p[Z] \frac{1 + a_1 EE + a_2 EE^2}{1 + b_1 EE + b_2 EE^2 + b_3 EE^3} - \frac{K}{1 + c_1 EE + c_2 EE^2};$$

$$CdTe_{NewApp} = TableForm \left[ Table \left[ \left\{ 10 x, 2. N_{CdTe} 10^{-24} cs \left[ \frac{x}{100.}, 50.18 \right] \right\}, \{x, 1, 70, 10\} \right], \right. \\ \left. TableHeadings \rightarrow \{None, \{"\gamma \text{ (keV)}", "\sigma \text{ (cm}^2/\text{g)}"\}\} \right]$$

$\gamma$ (keV)	$\sigma$ (cm <sup>2</sup> /g)
10	0.0603566
110	0.110636
210	0.0968713
310	0.0859079
410	0.0776953
510	0.0713328
610	0.0662274

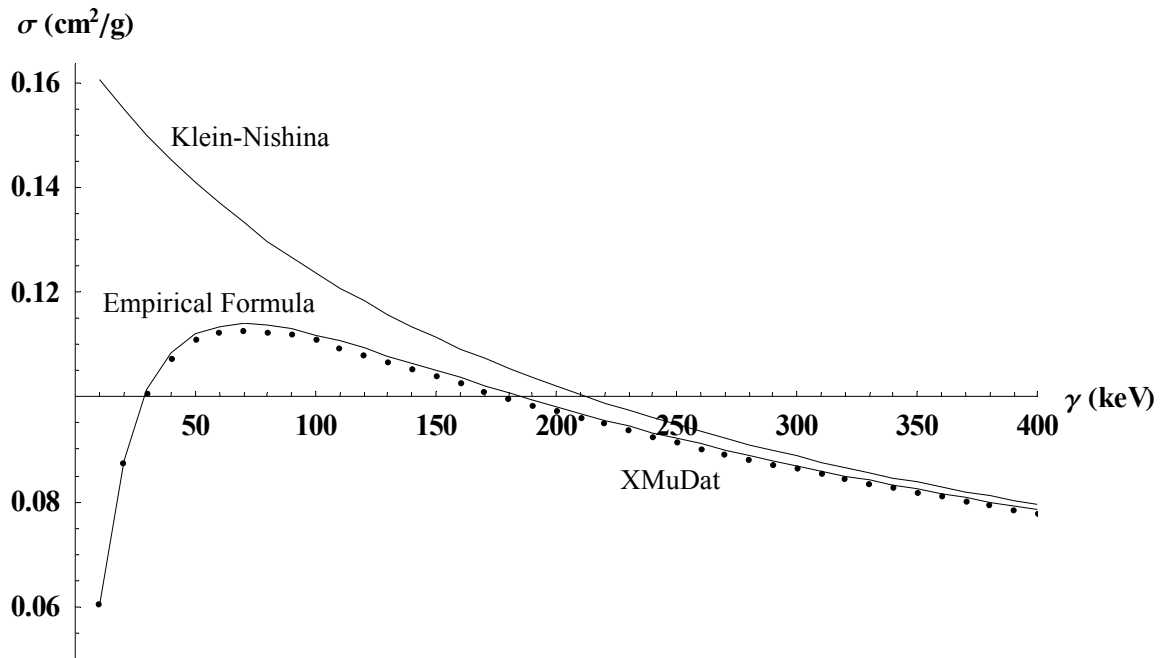


**Figure 64. Comparison plot of Klein-Nishina formula, an empirical formula (Massaro and Matt, 1986: 545-547) and XMuDat (Nowotny, 1998)**

## Appendix D: Compton Relation Calculations

The following calculations, produced in *Mathematica*® demonstrate the relation between the resolution achieved in collecting the Compton electron in the EEA and the calculated gamma ray full-energy peak resolution. The calculations are performed for 200-700 keV gamma rays with Compton scatter angles of 0.4, 0.53, 0.6, and 0.7 radians.

Formulas used:

$$m_0 = 511;$$

$$\text{ComptElect}[\theta\_ , x\_ ] := x - \frac{x}{1 + \frac{x}{m_0} (1 - \text{Cos}[\theta])} ;$$

$$\gamma[\theta\_ , \text{CE}\_] = \frac{1}{2 (1 - \text{Cos}[\theta])} \left( \text{CE} - \text{CE} \text{Cos}[\theta] - \sqrt{\text{CE}} \sqrt{-1 + \text{Cos}[\theta]} \sqrt{-\text{CE} + \text{CE} \text{Cos}[\theta] - 4 m_0} \right) ;$$

$$\text{ComptFWHM}[\text{New}\theta\_ , \text{FWHM}\_] =$$

$$\text{Re} \left[ \gamma[\text{New}\theta, \left( \text{ComptElect}[\text{New}\theta, \Gamma] + \frac{\text{FWHM}}{2.} \right)] \right] - \text{Re} \left[ \gamma[\text{New}\theta, \left( \text{ComptElect}[\text{New}\theta, \Gamma] - \frac{\text{FWHM}}{2.} \right)] \right] ;$$

**Table 10. Compton electron energy as a function of incident gamma ray energy and scatter gamma ray angle (in radians)**

Incident Gamma Ray (keV)	Compton Electron (keV) $\theta=.4$	Compton Electron (keV) $\theta=.53$	Compton Electron (keV) $\theta=.6$	Compton Electron (keV) $\theta=.7$
200	6.0	10.2	12.8	16.9
300	13.3	22.4	27.9	36.4
400	23.3	38.8	48.1	62.2
500	35.9	59.2	73.0	93.5
600	50.9	83.2	102.1	129.8
700	68.3	110.7	135.1	170.6

**Table 11. Compton Electron FWHM vs. Incident Gamma Ray FWHM ( $\gamma=200$  keV)**

EEA FWHM (keV)	FEP FWHM ( $\theta=.4$ )	FEP FWHM ( $\theta=.53$ )	FEP FWHM ( $\theta=.6$ )	FEP FWHM ( $\theta=.7$ )
0.1	1.694	1.007	0.8072	0.6194
0.2	3.388	2.014	1.614	1.239
0.3	5.082	3.021	2.422	1.858
0.4	6.776	4.027	3.229	2.477
0.5	8.470	5.034	4.036	3.097
0.6	10.17	6.042	4.844	3.716
0.7	11.86	7.049	5.651	4.336
0.8	13.56	8.056	6.459	4.955
0.9	15.25	9.064	7.266	5.575
1.	16.95	10.07	8.074	6.194
1.1	18.65	11.08	8.881	6.814
1.2	20.35	12.09	9.689	7.433
1.3	22.05	13.10	10.50	8.053
1.4	23.75	14.10	11.31	8.673

**Table 12. Compton Electron FWHM vs. Incident Gamma Ray FWHM ( $\gamma=300$  keV)**

EEA FWHM (keV)	FEP FWHM ( $\theta=.4$ )	FEP FWHM ( $\theta=.53$ )	FEP FWHM ( $\theta=.6$ )	FEP FWHM ( $\theta=.7$ )
0.1	1.154	0.6967	0.5638	0.4388
0.2	2.309	1.393	1.128	0.8776
0.3	3.463	2.090	1.691	1.316
0.4	4.618	2.787	2.255	1.755
0.5	5.773	3.484	2.819	2.194
0.6	6.927	4.181	3.383	2.633
0.7	8.082	4.877	3.947	3.072
0.8	9.237	5.574	4.511	3.510
0.9	10.39	6.271	5.075	3.949
1.	11.55	6.968	5.638	4.388
1.1	12.70	7.665	6.202	4.827
1.2	13.86	8.362	6.766	5.266
1.3	15.01	9.059	7.330	5.704
1.4	16.17	9.756	7.894	6.143

**Table 13. Compton Electron FWHM vs. Incident Gamma Ray FWHM ( $\gamma=400$  keV)**

EEA FWHM (keV)	FEP FWHM ( $\theta=.4$ )	FEP FWHM ( $\theta=.53$ )	FEP FWHM ( $\theta=.6$ )	FEP FWHM ( $\theta=.7$ )
0.1	0.8849	0.5419	0.4423	0.3487
0.2	1.770	1.084	0.8846	0.6975
0.3	2.655	1.626	1.327	1.046
0.4	3.540	2.167	1.769	1.395
0.5	4.425	2.709	2.212	1.744
0.6	5.310	3.251	2.654	2.092
0.7	6.195	3.793	3.096	2.441
0.8	7.080	4.335	3.538	2.790
0.9	7.965	4.877	3.981	3.139
1.	8.850	5.419	4.423	3.487
1.1	9.735	5.961	4.865	3.836
1.2	10.62	6.502	5.308	4.185
1.3	11.50	7.044	5.750	4.534
1.4	12.39	7.586	6.192	4.882

**Table 14. Compton Electron FWHM vs. Incident Gamma Ray FWHM ( $\gamma=500$  keV)**

EEA FWHM (keV)	FEP FWHM ( $\theta=.4$ )	FEP FWHM ( $\theta=.53$ )	FEP FWHM ( $\theta=.6$ )	FEP FWHM ( $\theta=.7$ )
0.1	0.7233	0.4490	0.3695	0.2949
0.2	1.447	0.8981	0.7391	0.5898
0.3	2.170	1.347	1.109	0.8846
0.4	2.893	1.796	1.478	1.180
0.5	3.616	2.245	1.848	1.474
0.6	4.340	2.694	2.217	1.769
0.7	5.063	3.143	2.587	2.064
0.8	5.786	3.592	2.956	2.359
0.9	6.510	4.041	3.326	2.654
1.	7.233	4.490	3.695	2.949
1.1	7.956	4.939	4.065	3.244
1.2	8.679	5.389	4.434	3.539
1.3	9.403	5.838	4.804	3.833
1.4	10.13	6.287	5.173	4.128

**Table 15. Compton Electron FWHM vs. Incident Gamma Ray FWHM ( $\gamma=600$  keV)**

EEA FWHM (keV)	FEP FWHM ( $\theta=.4$ )	FEP FWHM ( $\theta=.53$ )	FEP FWHM ( $\theta=.6$ )	FEP FWHM ( $\theta=.7$ )
0.1	0.6156	0.3873	0.3211	0.2591
0.2	1.231	0.7745	0.6423	0.5182
0.3	1.847	1.162	0.9634	0.7774
0.4	2.462	1.549	1.285	1.036
0.5	3.078	1.936	1.606	1.296
0.6	3.693	2.324	1.927	1.555
0.7	4.309	2.711	2.248	1.814
0.8	4.924	3.098	2.569	2.073
0.9	5.540	3.485	2.890	2.332
1.	6.156	3.873	3.211	2.591
1.1	6.771	4.260	3.532	2.850
1.2	7.387	4.647	3.854	3.109
1.3	8.002	5.034	4.175	3.369
1.4	8.618	5.422	4.496	3.628

**Table 16. Compton Electron FWHM vs. Incident Gamma Ray FWHM ( $\gamma=700$  keV)**

EEA FWHM (keV)	FEP FWHM ( $\theta=.4$ )	FEP FWHM ( $\theta=.53$ )	FEP FWHM ( $\theta=.6$ )	FEP FWHM ( $\theta=.7$ )
0.1	0.5387	0.3432	0.2866	0.2337
0.2	1.077	0.6864	0.5733	0.4674
0.3	1.616	1.030	0.8599	0.7010
0.4	2.155	1.373	1.147	0.9347
0.5	2.693	1.716	1.433	1.168
0.6	3.232	2.059	1.720	1.402
0.7	3.771	2.402	2.007	1.636
0.8	4.309	2.746	2.293	1.869
0.9	4.848	3.089	2.580	2.103
1.	5.387	3.432	2.866	2.337
1.1	5.925	3.775	3.153	2.571
1.2	6.464	4.118	3.440	2.804
1.3	7.003	4.462	3.726	3.038
1.4	7.541	4.805	4.013	3.272



## Appendix E: CdTe Detector Systems and Supporting Electronics

A total of seven XR-100T-CdTe detectors with associated PX2T power supply/shaping amplifier were purchased from Amptek, Inc. System 7 was the original detector system used by Capt. Williams. This system's PX2T was modified for a variable high voltage bias listed below.

**Table 17. List of CdTe components**

<b>CdTe Detector Systems (EEA)</b>			
System #	XR-100T Serial Number	PX2T Serial Number	Manufacture's FWHM (122 keV)
1	03772	2316	1.145
2	03754	2346	1.319
3	03764	2343	1.24
4	03760	2280	1.427
5	03710	2317	1.239
6	03750	2306	1.084
7	03712	2283	1.181
<b>Additional Electronics</b>			
3125	Canberra Dual HVPS		1Z029517

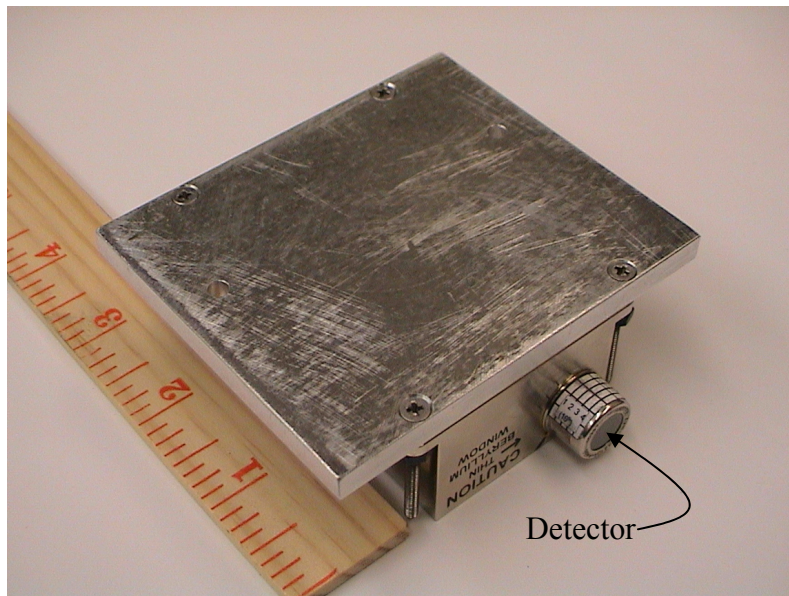


**Figure 65. Photograph of XR-100T-CdTe detector with housing removed**



**Figure 66. Photograph of PX2T-CdTe power supply and shaping amplifier**

## Appendix F: Attenuation Calculations

The following attenuation calculations were conducted to analyze the effects of the incident gamma rays entering the CdTe through the aluminum detector housing versus the beryllium window. The mass attenuation coefficients and densities used below were obtained from XMuDat (Nowotny, 1998).

(\*

Beryllium Data

\*)

$$\rho_{\text{Be}} = 1.848 \frac{\text{Gram}}{(\text{Centi Meter})^3};$$

$$\mu_{\text{MassBe}} = .06945 \frac{(\text{Centi Meter})^2}{\text{Gram}};$$

$$\mu_{\text{Be}} = \mu_{\text{MassBe}} \rho_{\text{Be}};$$

$$\text{BeAtten} = (1 - e^{-\mu_{\text{Be}} \text{ Convert [10. Mil, Centi Meter]}}) * 100. \% "$$

$$\underline{0.325462 \%}$$

(\*

Aluminum Data

\*)

$$\rho_{\text{Al}} = 2.699 \frac{\text{Gram}}{(\text{Centi Meter})^3};$$

$$\mu_{\text{MassAl}} = .07566 \frac{(\text{Centi Meter})^2}{\text{Gram}};$$

$$\mu_{\text{Al}} = \mu_{\text{MassAl}} \rho_{\text{Al}};$$

$$\text{AlAtten} = (1 - e^{-\mu_{\text{Al}} \text{ Convert [10. Mil, Centi Meter]}}) * 100. \% "$$

$$\underline{0.517341 \%}$$

## Appendix G: NaI(Tl) Detector and Supporting Electronics

Three NaI(Tl) detectors with integrated photomultiplier tubes and detachable preamplifiers were purchased for this project from Saint-Gobain, Inc. To operate the PEA the high voltage supply and amplifier listed below were used.

**Table 18. List of NaI(Tl) components**

<b>NaI(Tl) Detectors (PEA)</b>				
Detector #	Detector Serial Number	Photomultiplier Tube Serial Number	Preamplifier PA-14 Serial Number	Manufacturer's Resolution (662 keV)
1	60004-00024-I	75-4353	70004-0063	7.0%
2	60004-00025-I	75-4317	70004-0064	7.2%
3	60004-00026-I	75-4314	70004-0065	6.9%
<b>Additional Electronics</b>				
Model 9645	Canberra High Voltage Power Supply			08027948
Model 672	ORTEC Spectroscopy Amplifier			329



**Figure 67. Photograph of NaI(Tl) detector**





**Figure 68. NaI(Tl) in detector housing inside lead cave**

## **Appendix H: Coincidence Electronics**

Two methods were tested for determining coincidence, the start-stop method and the pulse overlap method. Photographs and lists of electronics follow.

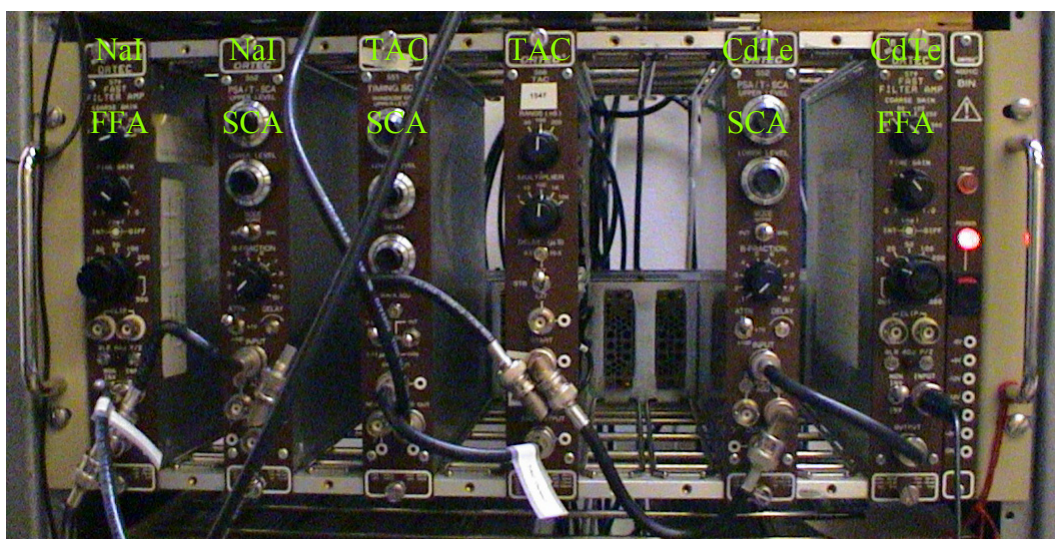


**Figure 69. Photograph of start-stop coincidence electronics**

**Table 19. Electronics used for start-stop coincidence technique**

TAC Coincidence Electronics			
Model	Component	Quantity	Serial Numbers
Model 566	ORTEC Time-to-Amplitude Converter/SCA	1	1547
Model 551	ORTEC Timing SCA	1	3880
Model 579	ORTEC Fast-Filter Amplifier	2	582/599
Model 552	ORTEC Pulse-Shape Analyzer/Timing SCA	2	1166/1163
Model 427A	ORTEC Delay Amplifier	3	4369/3703/3441

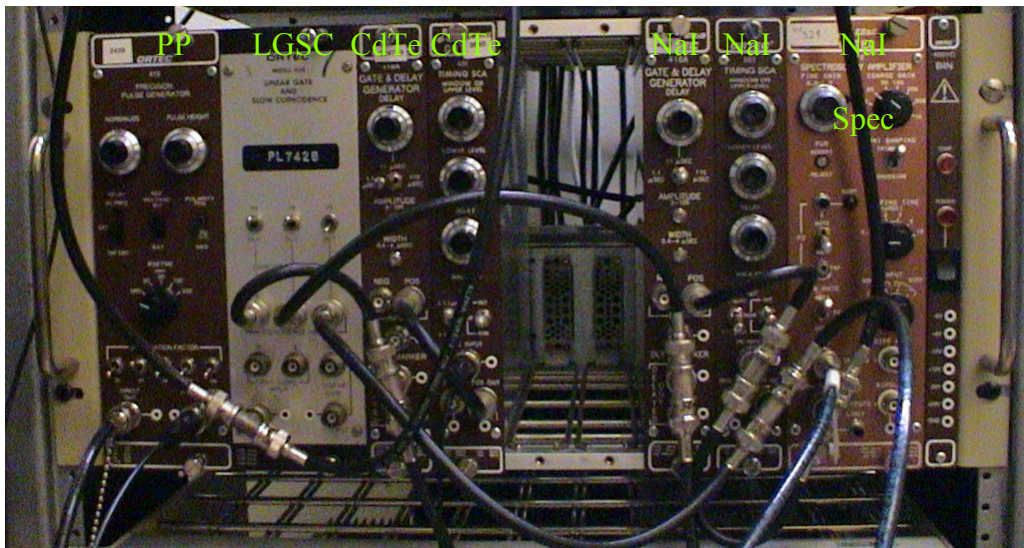


**Figure 70. Photograph of pulse overlap coincidence electronics**

**Table 20. Electronics used for pulse overlap technique**

LGSC Coincidence Electronics			
Model	Component	Quantity	Serial Numbers
Model 409	ORTEC Linear Gate Slow Coincidence	1	467
Model 551	ORTEC Timing SCA	2	3645/3957
Model 416A	ORTEC Gate and Delay Generator	2	004743/004397
Model 427A	ORTEC Delay Amplifier	3	4369/3703/3441

## **Appendix I: Initial Collimator**

Two initial collimators were used to collimate the sample source to the EEA; a manufactured hexagonal cross section collimator and a locally fabricated circular cross section collimator. The first collimator was used during Capt. Williams' research. Both were modified to include a source holder for source placement reproducibility.

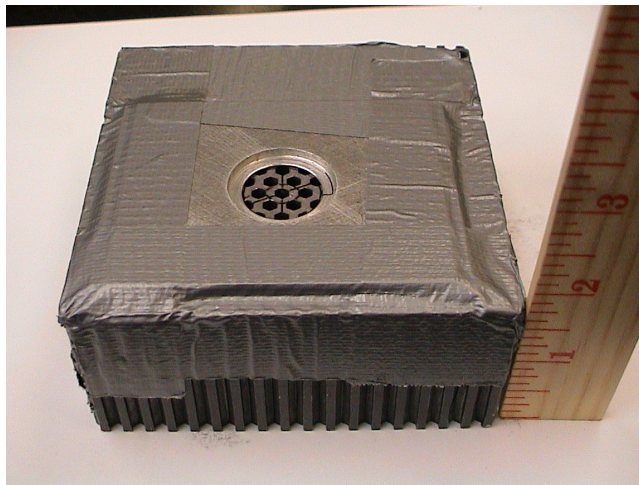


**Figure 71. Photograph of hexagonal cross section collimator**

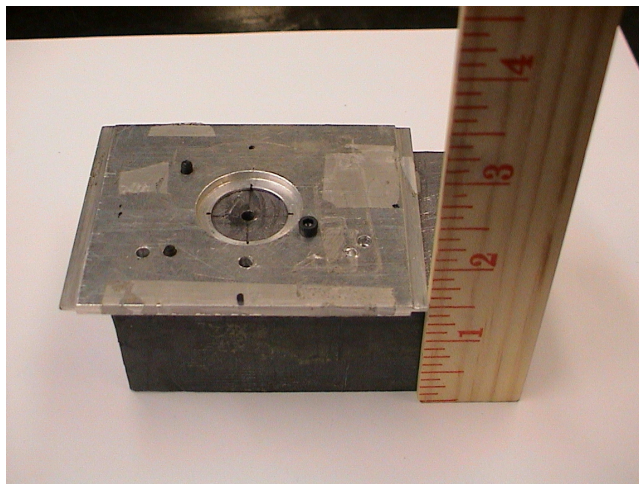


**Figure 72. Photograph of circular cross section collimator**



## **Appendix J: Conical Collimator**

The conical collimator used was fabricated by Capt. Williams (Williams, 2003: 122-123).



**Figure 73. Photograph of conical collimator with alignment grid in center**



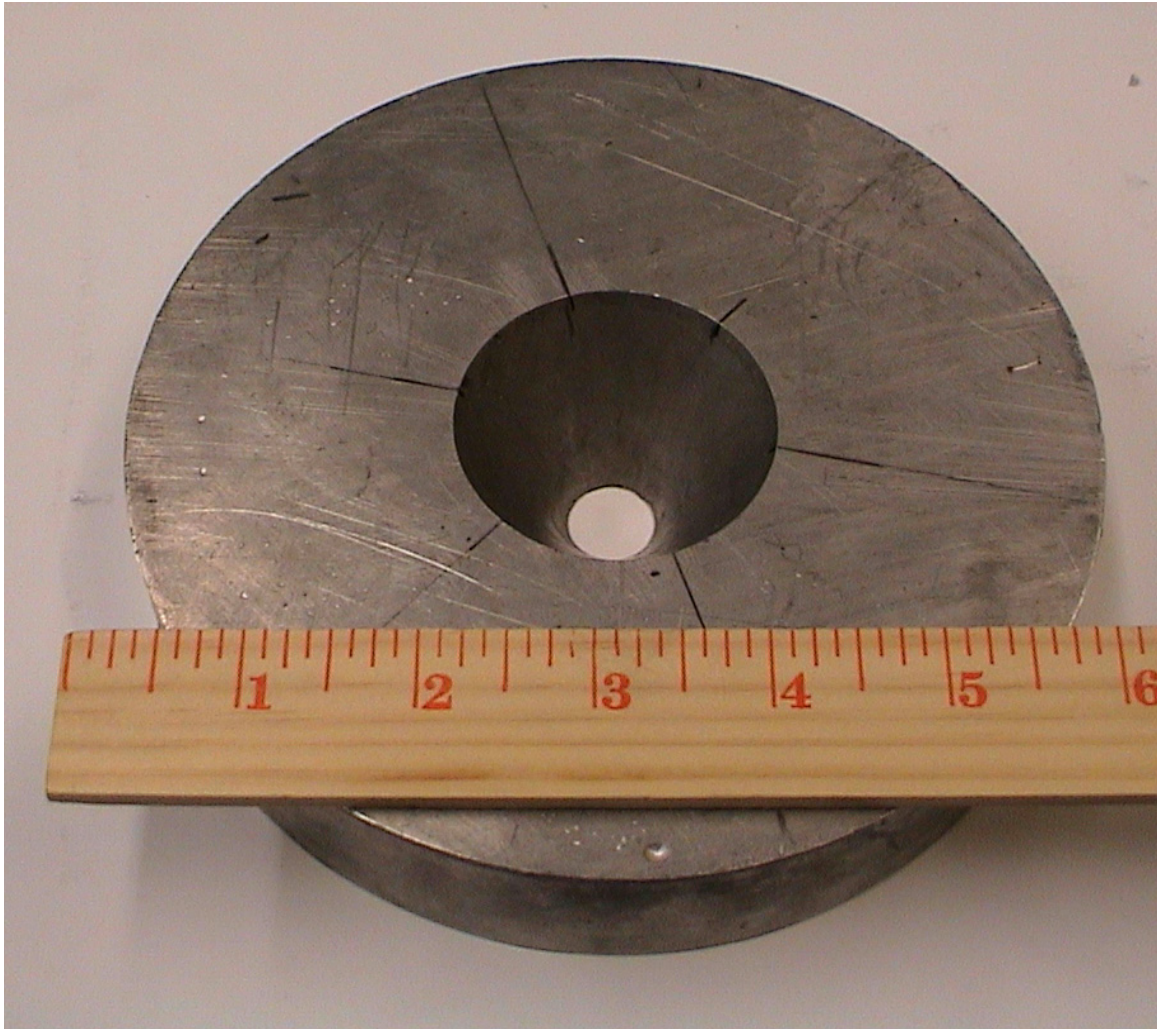


**Figure 74. Photograph of conical collimator without center cone**

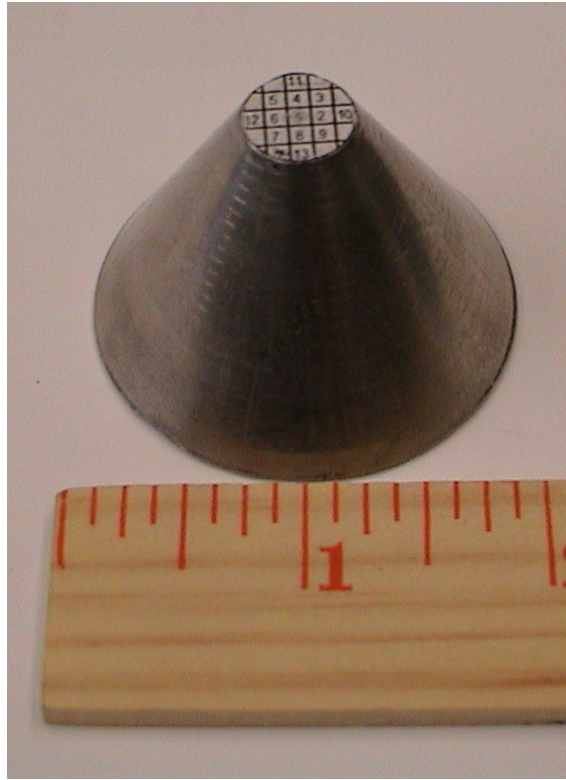


**Figure 75. Photograph of conical collimator inside cone with alignment grid**

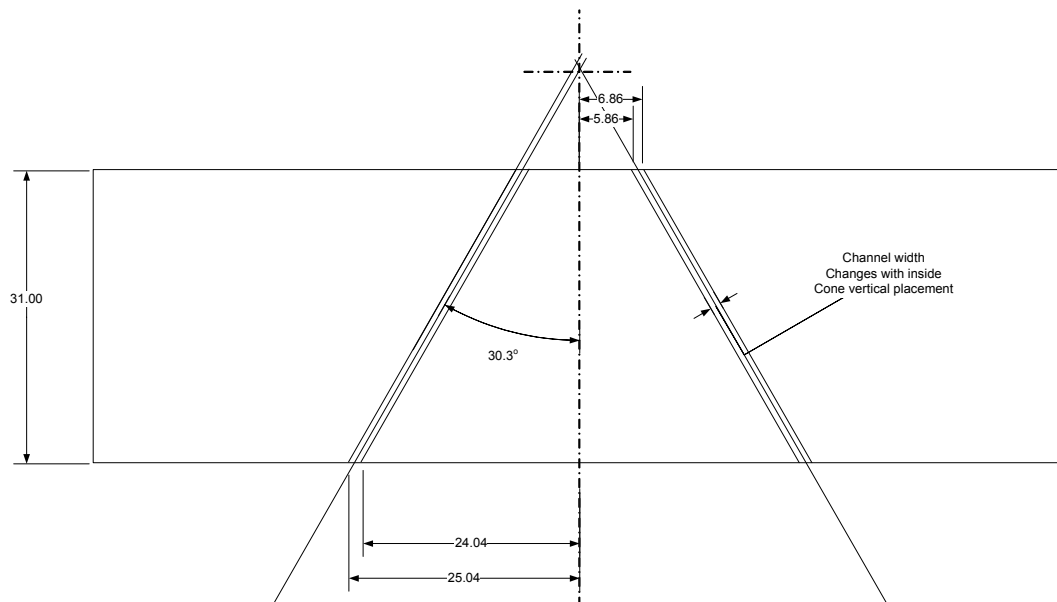


**Figure 76. Dimensions of conical collimator**

## Appendix K: Radioactive Sources

The list below contains all sources used during this thesis.

**Table 21. Radioactive sources**

<b>Source</b>	<b>ID #</b>	<b>Manf.</b>	<b>Ref Date</b>	<b>Initial Activity</b>	<b>Uncert.</b>	<b>Active Diam.</b>
Cs-137	T-083	IPL*	15-Jul-1998	326.7 kBq	±3.0 %	3 mm
Cs-137	T-084	IPL*	15-Jul-1998	375.2 kBq	±3.0 %	3 mm
Co-57	T-085	IPL*	15-Aug-1998	3479 kBq	±3.0 %	3 mm
Cs-137	T-089	IPL*	1-Aug-1998	370.7 kBq	±3.1 %	3 mm
Multinuclide	T-103	IPL*	15-Mar-2001	58.20 kBq	±3.0 %	5 mm
Multinuclide	T-105	IPL*	1-Nov-2002	190.3 kBq	±3.1 %	5 mm
Na-22	T-106	IPL*	15-Feb-2003	32.87 kBq	±3.1 %	3 mm
Na-22	T-107	IPL*	15-Feb-2003	32.55 kBq	±3.1 %	3 mm
Multinuclide	T-108	IPL*	15-Jul-2004	37.67 kBq	±3.4 %	5 mm
Multinuclide	T-109	IPL*	15-Jul-2004	37.37 kBq	±3.1 %	5 mm
Eu-152	T-110	IPL*	15-Dec-2004	375.2 kBq	±3.0 %	5 mm
Na-22	T-111	IPL*	1-Jan-2005	1997 kBq	±3.0 %	3 mm
*IPL-Isotope Product Laboratories						

## Appendix L: Sample Calculation of Activity Adjustment for Current Date

Standard radioactive decay formula:

$$A[t\_ , Nuclide\_ ] = A_{0,Nuclide} e^{-\frac{\text{Log}[2.]}{T_{Nuclide}} t} ;$$

$$\gamma[t\_ , Nuclide\_ ] = BR_{Nuclide} A[t, Nuclide] \left( \frac{1 * 10^{-6} 3.7 * 10^{10}}{\text{Micro Curie Second}} \right) ;$$

Certificate information for multinuclide sample T-105:

```
(* Multinuclide T105 *)
RefDateT105 = {2002, 11, 1};
A0,Am241 = 0.1522 Micro Curie;
TAm241 = Convert[432.17 Year, Day];
BRAm241 = .36;
A0,Cd109 = 1.4 Micro Curie;
TCd109 = 462.6 Day;
BRCd109 = .0363;
A0,Co57 = 0.05457 Micro Curie;
TCo57 = 271.79 Day;
BRCo57 = .856;
A0,Tel23m = 0.06895 Micro Curie;
TTel23m = 119.7 Day;
BRTel23m = .84;
A0,Cr51 = 1.836 Micro Curie;
TCr51 = 27.706 Day;
BRCr51 = .0986;
A0,Sn113 = 0.2530 Micro Curie;
TSn113 = 115.09 Day;
BRSn113 = .6489;
A0,Sr85 = 0.3509 Micro Curie;
TSr85 = 64.849 Day;
BRSr85 = .984;
A0,Cs137 = 0.2365 Micro Curie;
TCs137 = Convert[30.17 Year, Day];
BRCs137 = .851;
A0,Y88 = 0.5066 Micro Curie;
TY88 = 106.63 Day;
BRY88 = .94;
A0,Co60 = 0.2840 Micro Curie;
TCo60 = Convert[5.272 Year, Day];
BRCo60 = .9986;
```

SampleDate = {2004, 7, 28};

DecayTime = DaysBetween[RefDate<sub>T105</sub>, SampleDate] Day;

A[DecayTime, Am241]

A[DecayTime, Cd109]

γ[DecayTime, Am241]

γ[DecayTime, Cd109]

Am241 current activity= 0.151776 Curie Micro

Cd109 current activity= 0.540644 Curie Micro  
2021.66

Am241 intensity=  $\frac{\text{Second}}{726.139}$

Cd109 intensity=  $\frac{\text{Second}}{726.139}$

$$A[t\_ , SId\_ , Nuclide\_ ] = A_{0,SId} e^{-\frac{\text{Log}[2.]}{T_{\text{Nuclide}}} t} ;$$

$$\gamma[t\_ , SId\_ , Nuclide\_ ] = BR_{\text{Nuclide}} A[t, SId, Nuclide] \left( \frac{1 * 10^{-6} 3.7 * 10^{10}}{\text{Micro Curie Second}} \right) ;$$

RefDate<sub>T083</sub> = {1998, 07, 15};

RefDate<sub>T084</sub> = {1998, 07, 15};

RefDate<sub>T089</sub> = {1998, 08, 01};

A<sub>0,T083</sub> = Convert[326.7 Kilo Becquerel, Micro Curie];

A<sub>0,T084</sub> = Convert[375.2 Kilo Becquerel, Micro Curie];

A<sub>0,T089</sub> = Convert[370.7 Kilo Becquerel, Micro Curie];

T<sub>Cs137</sub> = Convert[30.17 Year, Day];

BR<sub>Cs137</sub> = .851;

SampleDate = {2004, 10, 28};

DecayTime[SId\_] = DaysBetween[RefDate<sub>SId</sub>, SampleDate] Day;

A[DecayTime[T083], T083, Cs137] +

A[DecayTime[T084], T084, Cs137] +

A[DecayTime[T089], T089, Cs137]

γ[DecayTime[T083], T083, Cs137] +

γ[DecayTime[T084], T084, Cs137] +

γ[DecayTime[T089], T089, Cs137]

25.096 Curie Micro

790199.

$\frac{\text{Second}}{790199.}$

## **Appendix M: Simulated System Computer Code**

The *Mathematica* program attached below was written to simulate the Compton spectrometer and create a Compton electron energy spectrum as seen in the EEA. The program analyzes the effects of varying geometric parameters on the resolution and efficiency of the Compton spectrometer system. An iterative method is used to step through a finite number a three-point combinations, see Figure 77, representing a gamma ray emitted from an incremental source area then Compton scattered in an incremental EEA detector volume and passing through an incremental area at the bottom of the conical collimator where it is absorbed in the PEA. If the photon is not geometrically blocked by any collimator material the energy of the resulting Compton electron and the probability of that three-point combination occurring are determined.

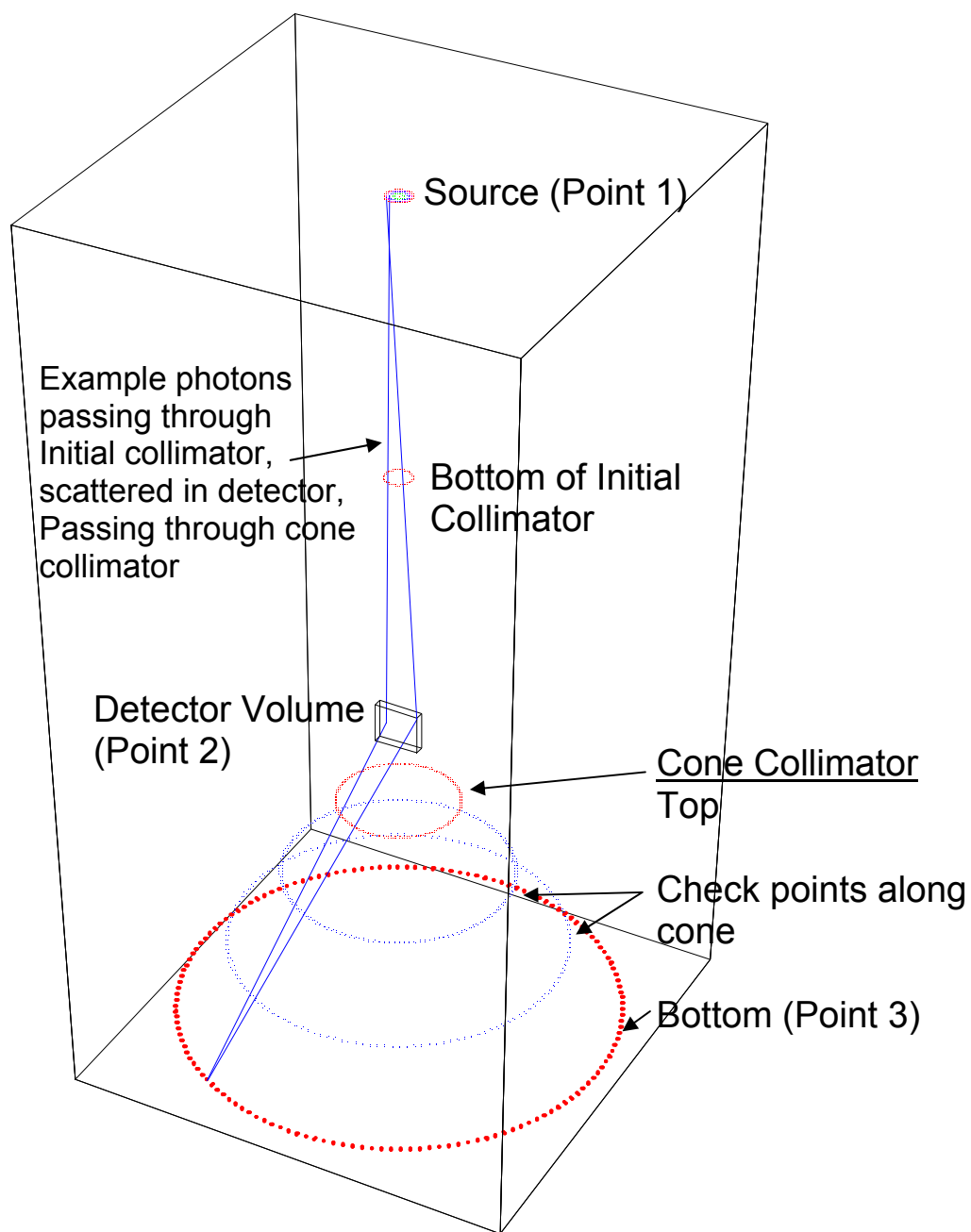


**Figure 77. Code Simulation geometry**

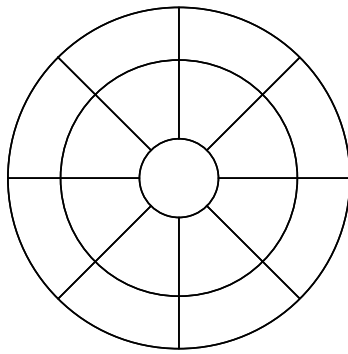


**Figure 78. Example of incremental source areas. Radius pixel set to 3 and angle pixel set to 8.**

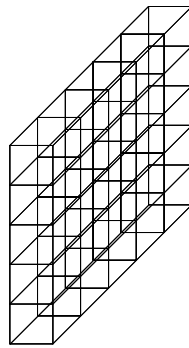


**Figure 79. Example of incremental EEA volumes.  $5 \times 5 \times 1 \text{ mm}^3$  with proportional pixel set to 1.**

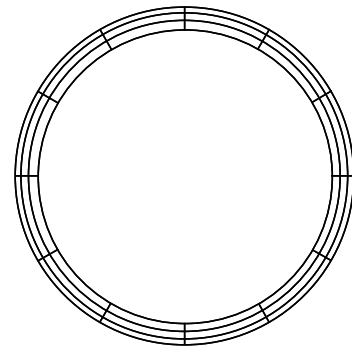


**Figure 80. Example of incremental areas of bottom conical collimator gap. Radius pixel set to 3 and angle pixel set to 12.**

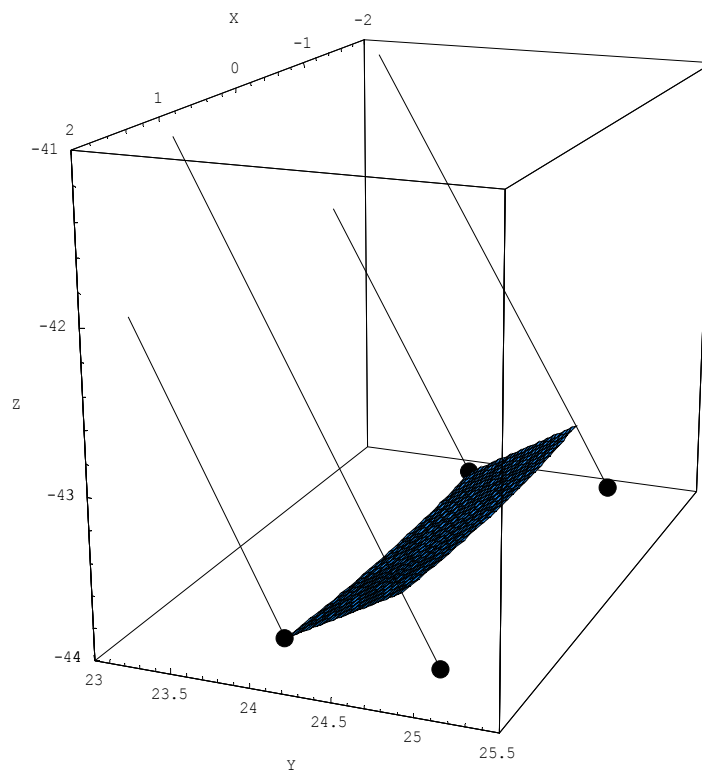


**Figure 81. Example geometry used to calculate Compton electron energies and Compton scatter probabilities.**



The energy of the Compton electron is calculated using the Compton relation described in Equation 2 and an estimated scatter angle created by the three-point combination. Four scatter angles are calculated for each three-point combination using the center point of the incremental source area, the center point of the incremental detector volume and the four corners of the incremental area at the bottom of the conical collimator as shown in Figure 81. The average of these four scatter angles is then used to calculate the Compton electron energy. Similar to an analog to digital converter (ADC), the probability of this combination is collected in an “energy bin” based on the Compton electron energy calculated and the energy versus probability spectrum shown in Figure 82 is produced.

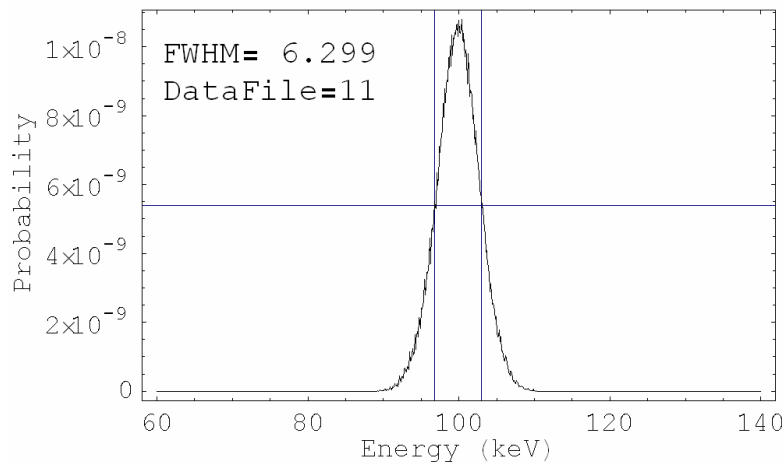


**Figure 82. Example output of simulation showing Compton electron energy versus probability spectrum.**

The probability of the three-point combination occurring is the product of the probability that the incremental area of the isotropic source emits a gamma ray into the top area of the incremental detector volume and the probability that the gamma ray will

Compton scatter from the incremental detector volume into the incremental area at the bottom of the conical collimator. Treating the incremental source area as a point, Equation 14 is used to determine the solid angle subtended by the incremental detector volume. To calculate the scatter probability Equation 6 is used with  $x_1$  and  $x_2$  determined by the incremental detector volume depth and  $\mu$  calculated using the Klein-Nishina formula shown in Equation 4. The formula is modified for the solid angle integration over  $d\theta$  and  $d\phi$  and the limits of the integration change for each three-point combination. The scatter angles calculated to determine the Compton electron energy are used for the  $d\theta$  limits and the arc size of the conical collimator pixel is used for the  $d\phi$  limits.

A source activity and collection time can be included to produce the typical Compton electron energy versus counts spectrum as shown in Figure 83. The incremental source areas are created equal therefore the activity is distributed evenly over the entire source area.

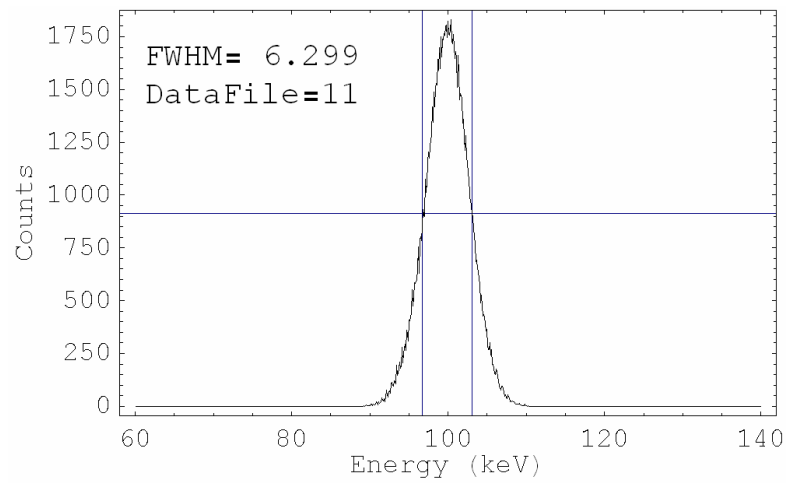


**Figure 83. Example output of simulation showing Compton electron energy versus counts spectrum.**

```

<< Graphics`ArgColors`;
<< Graphics`Graphics3D`;
<< Graphics`Shapes`;
<< LinearAlgebra`MatrixManipulation`;
<< Miscellaneous`Units`
Needs["Miscellaneous`RealOnly`"];
Off[General::"spell1"];
Off[General::"spell"];

ComptSpect =
Compile[{collz, CollGap, ZSource, ZBotInitColl, {SourceAnglePix, _Integer}, {SourceRadPix, _Integer},
  {CollAnglePix, _Integer}, {CollRadPix, _Integer},
  {PropPix, _Integer}, {CheckPoints, _Integer},  $\gamma$ , DetWidthX, DetWidthY, DetWidthZ, SourceRad,
  InitCollRad},
(* ***** Initial set up of variables ***** *)
Act = (800 * 1000) * (3600 * 1.) / ((SourceAnglePix(SourceRadPix - 1)) + 1.);
DetPixX = PropPix DetWidthX;
DetPixY = PropPix DetWidthY;
DetPixZ = PropPix DetWidthZ;
dDT =  $\frac{\text{DetWidthZ}}{2. \text{DetPixZ}}$ ;
ZTopInitColl = ZSource;
EnergyLower = 60.;
EnergyUpper = 140.;
EnergyBinSize = .1;
EnergyBins = IntegerPart[(EnergyUpper - EnergyLower) / EnergyBinSize];
Do[En[i] = 0, {i, 1, EnergyBins}];
Do[NoProbEn[i] = 0, {i, 1, EnergyBins}];
TopOuterConeCollRad = 6.86;
BotOuterConeCollRad = 25.04;
TopInnerConeCollRad = TopOuterConeCollRad - CollGap;
BotInnerConeCollRad = BotOuterConeCollRad - CollGap;
ZTopConeColl = -12.9 + collz;
ZBotConeColl = ZTopConeColl - 31.0;

```

```

(* ***** Create Source Radii ***** *)
Clear[SourceR];
Clear[TempR];
TempR[0] = 0.;
TempR[SourceRadPix] = SourceRad;
TempRad = Table[0, {i, 1, 2}, {j, 1, 2}];
Area = SourceRad2 / ((SourceAnglePix(SourceRadPix - 1)) + 1.);
TempRad = Solve[Area == TempR[1]2, TempR[1]];
TempR[1] = TempR[1] /. TempRad[[2, 1]];
SourceR[1] = 0.;
Do[TempRad = Solve[Area == (TempR[i]2 - TempR[i - 1]2) / SourceAnglePix, TempR[i]];
  TempR[i] = TempR[i] /. TempRad[[2, 1]];
  SourceR[i] = Sqrt[ $\left(\frac{1}{2} (\text{TempR}[i]^2 + \text{TempR}[i - 1]^2)\right)$ ],
  {i, 2, SourceRadPix - 1}];
SourceR[SourceRadPix] = Sqrt[ $\left(\frac{1}{2} (\text{TempR}[\text{SourceRadPix}]^2 + \text{TempR}[\text{SourceRadPix} - 1]^2)\right)$ ];

(* ***** Create Source Radii ***** *)
(* ***** Create Bottom Collimator Radii ***** *)
Clear[TempR];
Clear[BottomCollR];
TempR[0] = BotInnerConeCollRad;
TempR[CollRadPix] = BotOuterConeCollRad;
Area =  $\frac{1}{\text{CollRadPix}}$  (BotOuterConeCollRad2 - BotInnerConeCollRad2);
Do[TempRad = Solve[Area == TempR[i]2 - TempR[i - 1]2, TempR[i]];
  TempR[i] = TempR[i] /. TempRad[[2, 1]];
  BottomCollR[i] = TempR[i],
  {i, 1, CollRadPix - 1}];
BottomCollR[0] = BotInnerConeCollRad;
BottomCollR[CollRadPix] = BotOuterConeCollRad;

(* ***** Create Bottom Collimator Radii ***** *)
(* ***** Klein-Nishina Formula ***** *)
ACd = 112.411;
ATe = 127.60;
ZCdTe = 100; (* Electros per CdTe *)
ρCdTe = 6.06; (* Density from Knoll *)
NCdTe =  $\frac{6.02214 \times 10^{23}}{(A_{Cd} + A_{Te})}$ ;
α[hv_] =  $\frac{h\nu}{511}$ ;
r0 = 100 * 2.817940285 * 10-15;
(* Note: Z is the number of electrons *)

```

```

KN[θ_, Z_, hv_] = Z r0^2 (1 / (1 + α[hv] (1 - Cos[θ])))^2  $\left( \frac{1 + \text{Cos}[\theta]^2}{2} \right)$ 
(1 + (α[hv]^2 (1 - Cos[θ])^2) / ((1 + Cos[θ]^2) (1 + α[hv] (1 - Cos[θ]))));
(* ***** Klein–Nishina Formula ***** *)
(* ***** END Initial set up of variables ***** *)

(* ***** Start Calculations ***** *)
a = 0;
(* Detector Z *) Do[
(* Detector Y *) Do[
(* Detector X *) Do[
(* ***** Create ConeCollTestData Array ***** *)
(* Collimator Angle *) Do[
(* Collimator Radius *) Do[
XSlope =  $\left( \text{BottomCollR}[\text{CollRadIndex}] \cos \left[ \frac{2\pi}{\text{CollAnglePix}} (\text{CollAngleIndex} - 1) \right] \right) - \text{dp}x;$ 
YSlope =  $\left( \text{BottomCollR}[\text{CollRadIndex}] \sin \left[ \frac{2\pi}{\text{CollAnglePix}} (\text{CollAngleIndex} - 1) \right] \right) - \text{dp}y;$ 
ZSlope = ZBotConeColl - dpz;

Do[(*Test points in channel*)
ZCheck = ZTopConeColl + (ZBotConeColl - ZTopConeColl) / (CheckPoints + 1) k;
RCheckMin = TopInnerConeCollRad + (BotInnerConeCollRad - TopInnerConeCollRad) / (CheckPoints + 1) k;
RCheckMax = TopOuterConeCollRad + (BotOuterConeCollRad - TopOuterConeCollRad) / (CheckPoints + 1) k;
tt =  $\frac{Z\text{Check} - \text{dp}z}{Z\text{Slope}};$ 
(*Print[tt," ",RCheckMax^2," ",RTest," ",RCheckMin^2];*)
RTest = (dpX + XSlope tt)^2 + (dpY + YSlope tt)^2;
If[
RTest ≤ RCheckMax^2 && RTest ≥ RCheckMin^2,
(* True *)
ConeTest = 1,
(* False *)
ConeTest = 0.,
Print[{"Cone Collimator Test Failed", RCheckMax, RCheckMin, RTest}];
ConeTest = 0.
];
If[ConeTest == 0, Break[]],
{k, 0, CheckPoints}];

```

```

ConeCollTestData[CollRadIndex, CollAngleIndex] = ConeTest;
, {CollRadIndex, 0, CollRadPix}];
, {CollAngleIndex, 1, CollAnglePix}];
Do[ConeCollTestData[CollRadIndex, CollAnglePix + 1] = ConeCollTestData[CollRadIndex, 1],
{CollRadIndex, 0, CollRadPix}];
(* ***** Create ConeCollTestData Array ***** *)
(* ***** Test ConeCollTestData Array Create ConeCollTest Array ***** *)
Do[If[ConeCollTestData[CollRadIndex, CollAngleIndex] == 1 &&
ConeCollTestData[CollRadIndex + 1, CollAngleIndex] == 1 &&
ConeCollTestData[CollRadIndex, CollAngleIndex + 1] == 1 &&
ConeCollTestData[CollRadIndex + 1, CollAngleIndex + 1] == 1, CollConeTest[CollRadIndex, CollAngleIndex] = 1,
CollConeTest[CollRadIndex, CollAngleIndex] = 0];
(*Print[ConeTest[CollRadIndex, CollAngleIndex]]*)
, {CollRadIndex, 0, CollRadPix - 1}, {CollAngleIndex, 1, CollAnglePix}];

(* ***** Test ConeCollTestData Array Create ConeCollTest Array ***** *)

(* Collimator*)Do[
(* Source Radius *)Do[
If[CollConeTest[CollRadIndex, CollAngleIndex] == 0, Break[]];
(* Source Angle *)
Do[
If[CollConeTest[CollRadIndex, CollAngleIndex] == 0, Break[]];
(*Initial Collimator Test *)
spx = SourceR[SourceRadIndex] Cos[SourceAng];
spy = SourceR[SourceRadIndex] Sin[SourceAng];
XSlope = spx - dpx;
YSlope = spy - dpy;
ZSlope = ZSource - dpz;
tt =  $\frac{ZBotInitColl - dpz}{ZSlope}$ ;
RTest = (dpx + XSlope tt)2 + (dpy + YSlope tt)2;
If[RTest ≤ InitCollRad2,

a = a + 1;
(* ***** Distance traveled in CdTe ***** *)
ttDetTop =  $\frac{0. - dpz}{ZSlope}$ ;
DT = Sqrt[(XSlope ttDetTop)2 + (YSlope ttDetTop)2 + dpz2];
(* ***** Distance traveled in CdTe ***** *)

```

(\* \*\*\*\*\* Solid Angle: From Source Subtended by Detector \*\*\*\*\* \*)

SolidAngle =

$$\begin{aligned}
 & \text{ArcTan} \left[ \left( \left( \left( \text{dpx} + \frac{\text{DetWidthX}}{2 \cdot \text{DetPixX}} \right) - \text{spx} \right) \left( \left( \text{dpy} + \frac{\text{DetWidthY}}{2 \cdot \text{DetPixY}} \right) - \text{spy} \right) \right) / \right. \\
 & \quad \left. \left( (Z\text{Source} - \text{dpz}) \left( \left( \left( \text{dpx} + \frac{\text{DetWidthX}}{2 \cdot \text{DetPixX}} \right) - \text{spx} \right)^2 + \left( \left( \text{dpy} + \frac{\text{DetWidthY}}{2 \cdot \text{DetPixY}} \right) - \text{spy} \right)^2 + (Z\text{Source} - \text{dpz})^2 \right)^{\frac{1}{2}} \right) \right] - \\
 & \text{ArcTan} \left[ \left( \left( \left( \text{dpx} - \frac{\text{DetWidthX}}{2 \cdot \text{DetPixX}} \right) - \text{spx} \right) \left( \left( \text{dpy} + \frac{\text{DetWidthY}}{2 \cdot \text{DetPixY}} \right) - \text{spy} \right) \right) / \right. \\
 & \quad \left. \left( (Z\text{Source} - \text{dpz}) \left( \left( \left( \text{dpx} - \frac{\text{DetWidthX}}{2 \cdot \text{DetPixX}} \right) - \text{spx} \right)^2 + \left( \left( \text{dpy} + \frac{\text{DetWidthY}}{2 \cdot \text{DetPixY}} \right) - \text{spy} \right)^2 + (Z\text{Source} - \text{dpz})^2 \right)^{\frac{1}{2}} \right) \right] - \\
 & \text{ArcTan} \left[ \left( \left( \left( \text{dpx} + \frac{\text{DetWidthX}}{2 \cdot \text{DetPixX}} \right) - \text{spx} \right) \left( \left( \text{dpy} - \frac{\text{DetWidthY}}{2 \cdot \text{DetPixY}} \right) - \text{spy} \right) \right) / \right. \\
 & \quad \left. \left( (Z\text{Source} - \text{dpz}) \left( \left( \left( \text{dpx} + \frac{\text{DetWidthX}}{2 \cdot \text{DetPixX}} \right) - \text{spx} \right)^2 + \left( \left( \text{dpy} - \frac{\text{DetWidthY}}{2 \cdot \text{DetPixY}} \right) - \text{spy} \right)^2 + (Z\text{Source} - \text{dpz})^2 \right)^{\frac{1}{2}} \right) \right] + \\
 & \text{ArcTan} \left[ \left( \left( \left( \text{dpx} - \frac{\text{DetWidthX}}{2 \cdot \text{DetPixX}} \right) - \text{spx} \right) \left( \left( \text{dpy} - \frac{\text{DetWidthY}}{2 \cdot \text{DetPixY}} \right) - \text{spy} \right) \right) / \right. \\
 & \quad \left. \left( (Z\text{Source} - \text{dpz}) \left( \left( \left( \text{dpx} - \frac{\text{DetWidthX}}{2 \cdot \text{DetPixX}} \right) - \text{spx} \right)^2 + \left( \left( \text{dpy} - \frac{\text{DetWidthY}}{2 \cdot \text{DetPixY}} \right) - \text{spy} \right)^2 + (Z\text{Source} - \text{dpz})^2 \right)^{\frac{1}{2}} \right) \right];
 \end{aligned}$$

(\* \*\*\*\*\* Solid Angle: From Source Subtended by Detector \*\*\*\*\* \*)

(\* \*\*\*\*\* Calculate scatter angles \*\*\*\*\* \*)

SP = {spx, spy, ZSource};

DP = {dpx, dpy, dpz};

$$\text{CP1} = \left\{ \text{BottomCollR}[\text{CollRadIndex}] \cos \left[ \frac{2\pi}{\text{CollAnglePix}} (\text{CollAngleIndex} - 1) \right], \right.$$

$$\left. \text{BottomCollR}[\text{CollRadIndex}] \sin \left[ \frac{2\pi}{\text{CollAnglePix}} (\text{CollAngleIndex} - 1) \right], \text{ZBotConeColl} \right\};$$

$$\text{CP2} = \left\{ \text{BottomCollR}[\text{CollRadIndex} + 1] \cos \left[ \frac{2\pi}{\text{CollAnglePix}} (\text{CollAngleIndex} - 1) \right], \right.$$

$$\left. \text{BottomCollR}[\text{CollRadIndex} + 1] \sin \left[ \frac{2\pi}{\text{CollAnglePix}} (\text{CollAngleIndex} - 1) \right], \text{ZBotConeColl} \right\};$$

$$\text{CP3} = \left\{ \text{BottomCollR}[\text{CollRadIndex}] \cos \left[ \frac{2\pi}{\text{CollAnglePix}} (\text{CollAngleIndex}) \right], \right.$$

$$\left. \text{BottomCollR}[\text{CollRadIndex}] \sin \left[ \frac{2\pi}{\text{CollAnglePix}} (\text{CollAngleIndex}) \right], \text{ZBotConeColl} \right\};$$



```

CP4 = {BottomCollR[CollRadIndex + 1] Cos[ $\frac{2\pi}{\text{CollAnglePix}}$  (CollAngleIndex)],
      BottomCollR[CollRadIndex + 1] Sin[ $\frac{2\pi}{\text{CollAnglePix}}$  (CollAngleIndex)], ZBotConeColl};

ScatAngle1 = ( $\pi$  - ArcCos[
  Dot[SP - DP, CP1 - DP] / (Sqrt[Dot[SP - DP, SP - DP]] Sqrt[Dot[CP1 - DP, CP1 - DP]])]);
ScatAngle2 = ( $\pi$  - ArcCos[
  Dot[SP - DP, CP2 - DP] / (Sqrt[Dot[SP - DP, SP - DP]] Sqrt[Dot[CP2 - DP, CP2 - DP]])]);
ScatAngle3 = ( $\pi$  - ArcCos[
  Dot[SP - DP, CP3 - DP] / (Sqrt[Dot[SP - DP, SP - DP]] Sqrt[Dot[CP3 - DP, CP3 - DP]])]);
ScatAngle4 = ( $\pi$  - ArcCos[
  Dot[SP - DP, CP4 - DP] / (Sqrt[Dot[SP - DP, SP - DP]] Sqrt[Dot[CP4 - DP, CP4 - DP]])]);

(* ***** Calculate scatter angles ***** *)
(* ***** Calculate Compton Cross Sections ***** *)

lft = NIntegrate[NCdTe KN[ $\theta$ , ZCdTe, 662.] * Sin[ $\theta$ ], { $\theta$ , ScatAngle3, ScatAngle4}, { $\phi$ , 0,  $\frac{2\pi}{\text{CollAnglePix}}$ }]];

rt = NIntegrate[NCdTe KN[ $\theta$ , ZCdTe, 662.] * Sin[ $\theta$ ], { $\theta$ , ScatAngle1, ScatAngle2}, { $\phi$ , 0,  $\frac{2\pi}{\text{CollAnglePix}}$ }]];

 $\mu = \frac{\text{lft} + \text{rt}}{2}$ ;

(* ***** Calculate Compton Cross Sections ***** *)
(* ***** Calculate Compton Scatter Probability ***** *)

ScatProb =  $e^{-\mu \rho_{\text{CdTe}} \left(\frac{\text{DT}-\text{dDT}}{10.}\right)} - e^{-\mu \rho_{\text{CdTe}} \left(\frac{\text{DT}+\text{dDT}}{10.}\right)}$ ;

(* ***** Calculate Compton Scatter Probability ***** *)
(* ***** Calculate Compton Electron Energy ***** *)

ScatterAngle =  $\frac{1}{4.}$  (ScatAngle1 + ScatAngle2 + ScatAngle3 + ScatAngle4);

EnergyDeposited =  $\gamma - \gamma / \left(1 + \frac{\gamma}{511.} (1 - \text{Cos}[\text{ScatterAngle}])\right)$ ;

EnIndex = IntegerPart[ $\frac{\text{EnergyDeposited} - \text{EnergyLower}}{\text{Energy BinSize}}$ ];

En[EnIndex] = En[EnIndex] + (ScatProb * SolidAngle);
NoProbEn[EnIndex] = NoProbEn[EnIndex] + 1.;

(* ***** Calculate Compton Electron Energy ***** *)];

```

```

If[SourceRadIndex == 1, Break[], {SourceAng  $\frac{\pi}{\text{SourceAnglePix}}$ ,  $\left(2.\pi - \frac{\pi}{\text{SourceAnglePix}}\right)$ ,
 $\frac{2.\pi}{\text{SourceAnglePix}}$  }];
, {SourceRadIndex, 1, SourceRadPix}];

, {CollRadIndex, 0, CollRadPix - 1}, {CollAngleIndex, 1, CollAnglePix}];

, {dpx,  $-\frac{\text{DetWidthX}}{2.} + \frac{\text{DetWidthX}}{2.\text{DetPixX}}$ ,  $\frac{\text{DetWidthX}}{2.}$ ,  $\frac{\text{DetWidthX}}{\text{DetPixX}}$  }];
, {dpy,  $-\frac{\text{DetWidthY}}{2.} + \frac{\text{DetWidthY}}{2.\text{DetPixY}}$ ,  $\frac{\text{DetWidthY}}{2.}$ ,  $\frac{\text{DetWidthY}}{\text{DetPixY}}$  }];
Print[dpz];
, {dpz,  $-\frac{\text{DetWidthZ}}{2.\text{DetPixZ}}$ ,  $-\text{DetWidthZ}$ ,  $-\frac{\text{DetWidthZ}}{\text{DetPixZ}}$  }];
];

```

## Appendix N: CdTe Spectra

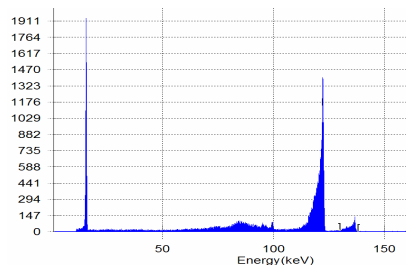


**Figure 84.  $^{57}\text{Co}$  spectrum using CdTe detector (RTD off, Position 1, Figure 20)**

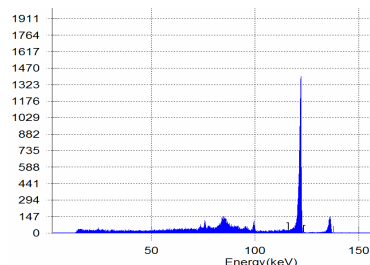


**Figure 87.  $^{57}\text{Co}$  spectrum using CdTe detector (RTD on, Position 2)**

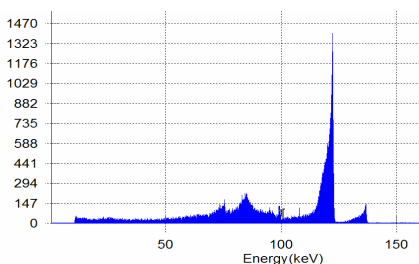


**Figure 85.  $^{57}\text{Co}$  spectrum using CdTe detector (RTD off, Position 2)**

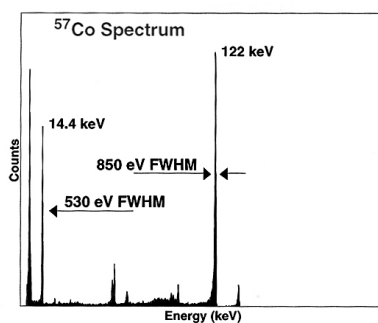


**Figure 88.  $^{57}\text{Co}$  spectrum using CdTe detector provided by Amptek (Amptek, 2004: 25)**

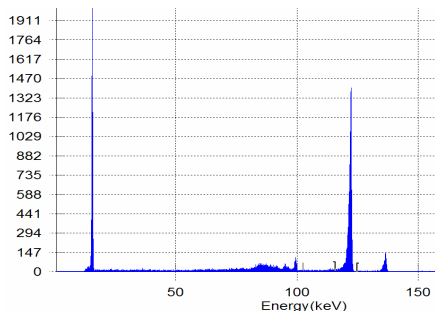


**Figure 86.  $^{57}\text{Co}$  spectrum using CdTe detector (RTD on, Position 1)**

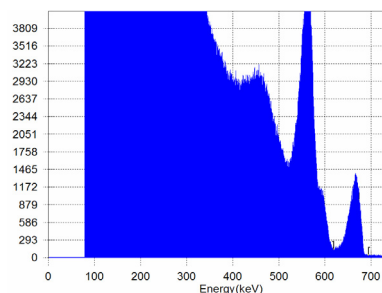


**Figure 89.  $^{137}\text{Cs}$  spectrum using CdTe detector (RTD off, Position 1)**

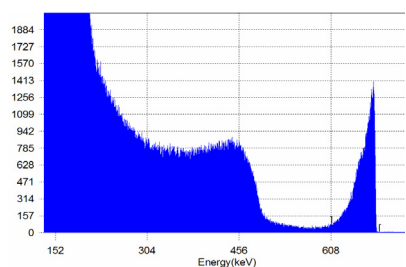


**Figure 90.**  $^{137}\text{Cs}$  spectrum using CdTe detector (RTD off, Position 2)

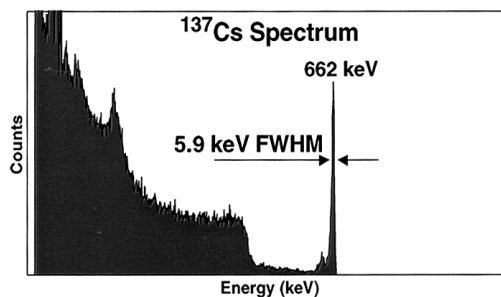


**Figure 93.**  $^{137}\text{Cs}$  spectrum using CdTe detector provided by Amptek (Amptek, 2004: 28)

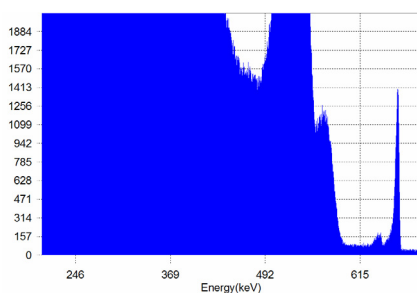


**Figure 91.**  $^{137}\text{Cs}$  spectrum using CdTe detector (RTD on, Position 1)

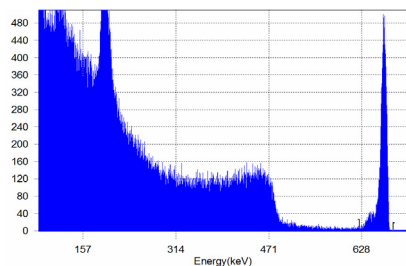


**Figure 92.**  $^{137}\text{Cs}$  spectrum using CdTe detector (RTD on, Position 2)

### Appendix O: NaI(Tl) Spectra

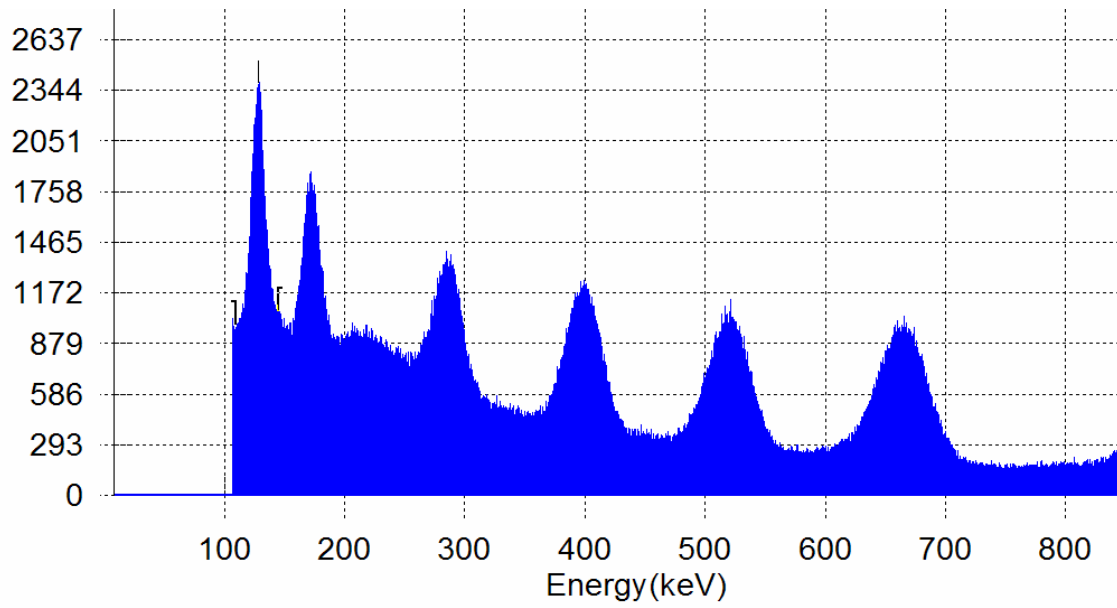


**Figure 94. Multinuclide (T108) spectrum using NaI(Tl) detector**

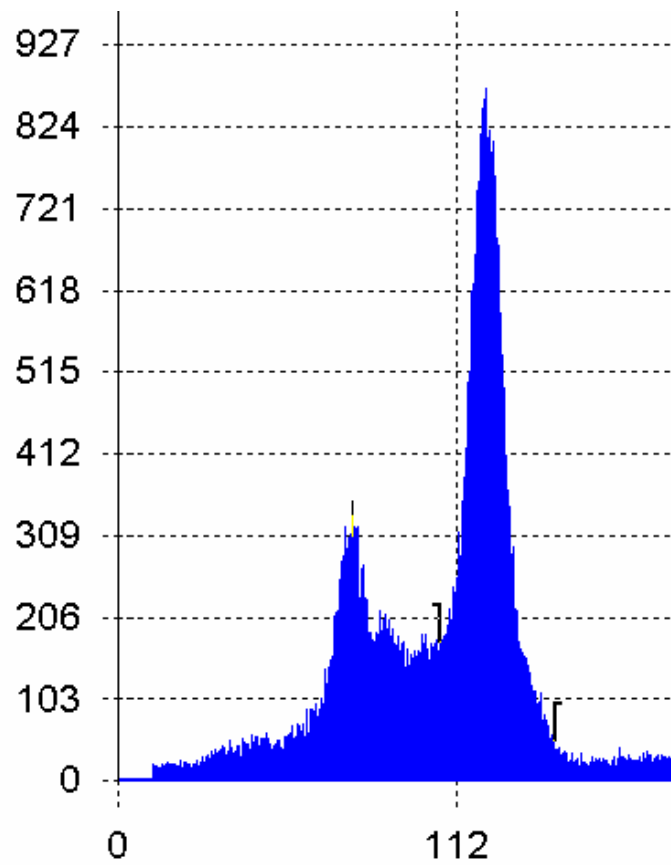


**Figure 95. NaI(Tl) detector characterization spectrum;  $^{57}\text{Co}$**

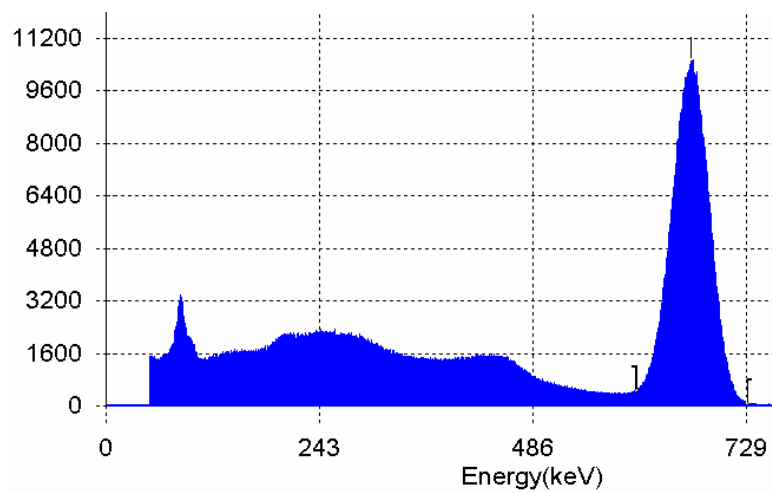


**Figure 96. NaI(Tl) detector characterization spectrum;  $^{137}\text{Cs}$**

## Appendix P: CdTe Detector Diagram

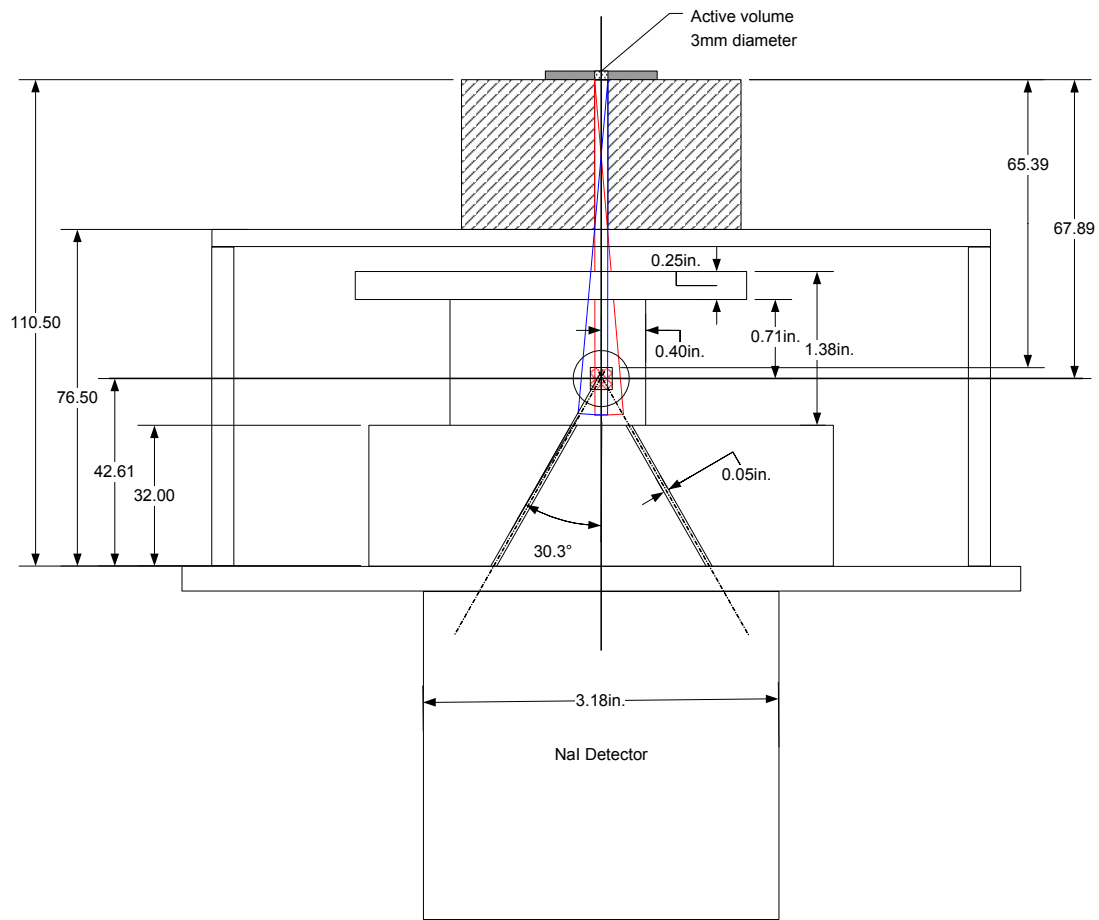


**Figure 97. Compton Detector System Geometry**

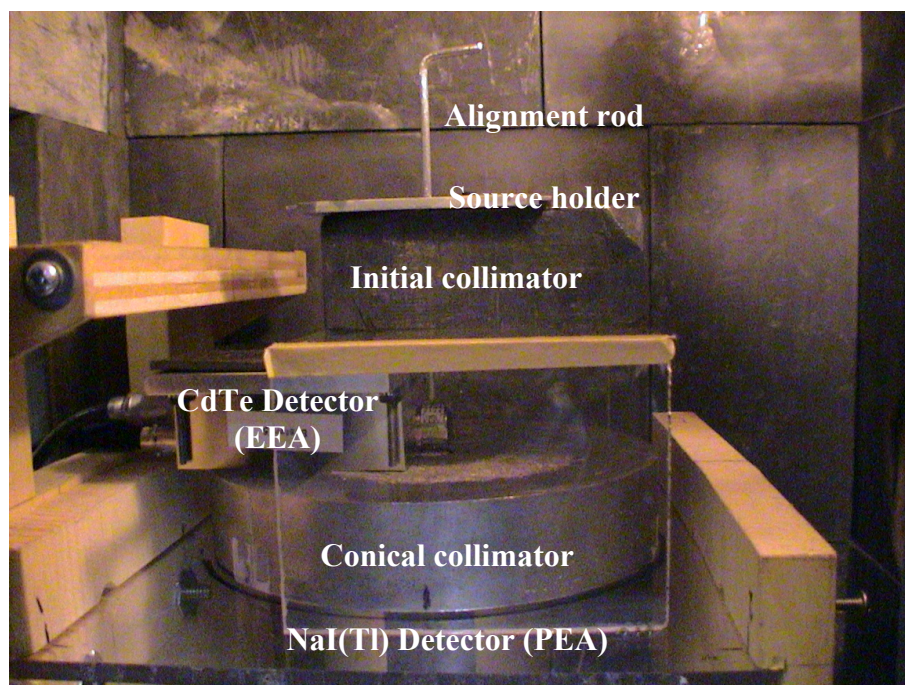


**Figure 98. Photograph of Compton spectrometer in situ**



## Bibliography

- Alley, Michael, *The Craft of Scientific Writing*, 3<sup>rd</sup> edition (New York: Springer, 1995).
- Amptek, Inc. *Operating Manual XR-10T-CdTeX-Ray and Gamma Ray Detector System and Px2T Power Supply/Shaping Amplifier* (October 200).
- Barnaby, Frank, *How to Build a Nuclear Bomb and Other Weapons of Mass Destruction* (New York: Nation Books, 2004).
- Butler, Richard, *Fatal Choice, Nuclear Weapons and the Illusion of Missile Defense* (Colorado: Westview Press, 2001).
- Debertin, Klaus and Helmer, Richard G., *Gamma- and x-Ray Spectrometry with Semiconductors Detectors* (Amsterdam: Elsevier Science B.V., 2001).
- Defense Threat Reduction Agency, *Weapons of Mass Destruction Terms Reference Handbook* (Alexandria, VA, DTRA, 2001).
- Genie 2000 Operations Manual*. Canberra Industries, Inc., 2001.
- Gotoh, H. and Yagi, H. *Solid Angle Subtended by a Rectangular Slit* (North-Holland Nuclear Instruments and Methods 96, 1971).
- Graham Jr., Thomas and LaVera, Damien J., *Cornerstones of Security-Arms Control Treaties in the Nuclear Age* (Seattle: University of Washington Press, 2003).
- Hays, Peter L., Jodoin, Vincent J. and Van Tassel, Alan R., *Countering the Proliferation and Use of Weapons of Mass Destruction* (New York: McGraw-Hill, 1998).
- Knoll, Glenn F., *Radiation Detection and Measurement*, 3<sup>rd</sup> Edition (New York: John Wiley & Sons, Inc., 2000).
- Massaro, Enrico and Matt, Giorgio, *A Simple Approximation for Incoherent Scattering Cross Section of X and Gamma Rays*, (Amsterdam: Instruments and Methods in Physics Research, A251 1986).
- Nelson, Michael B., *Detection of Special Nuclear Material with High Purity Germanium (HPGe) and Mercuric Iodide (HgI<sub>2</sub>) Gamma Detectors*, MS Thesis, AFIT/GNE/ENP/03-07 (WPAFB: Graduate School of Engineering and Management, Air Force Institute of Technology (AU), 2003).
- Nowotny, R., *XMudat: Photon Attenuation Data (v.1.0.1)*, (Austria, University of Vienna, 1998).
- ORTEC Modular Pulse Processing Catalog*. PerkinElmer Instruments (Received 2004).

- Takahashi, Tadayuki, Wantanabe, Shin, Kouda, Manabu, Sato, Goro, Okado, Yuu, Kubo, Shi, Kuroda, Yoshikatsu, Onishi, Mitsunobu, and Ohno, Ryoichi, *High Resolution CdTe Detector and Applications to Imaging Devices*, 2 November 2000.
- Tsoufpananidis, Nicholas, *Measurement and Detection of Radiation* (Washington, DC: Taylor & Francis, 1995).
- Turner, James E., *Atoms, Radiation, and Radiation Protection*, 2<sup>nd</sup> edition (New York: John Wiley & Sons, Inc., 1995).
- Williams, Christopher S., *Plutonium Isotopic Ratio Determination Using Compton Spectrometer System*, MS Thesis, AFIT/GNE/ENP/04-08 (WPAFB: Graduate School of Engineering and Management, Air Force Institute of Technology (AU), 2004).

REPORT DOCUMENTATION PAGE				Form Approved OMB No. 074-0188	
<p>The public reporting burden for this collection of information is estimated to average 1 hour per response, including the time for reviewing instructions, searching existing data sources, gathering and maintaining the data needed, and completing and reviewing the collection of information. Send comments regarding this burden estimate or any other aspect of the collection of information, including suggestions for reducing this burden to Department of Defense, Washington Headquarters Services, Directorate for Information Operations and Reports (0704-0188), 1215 Jefferson Davis Highway, Suite 1204, Arlington, VA 22202-4302. Respondents should be aware that notwithstanding any other provision of law, no person shall be subject to a penalty for failing to comply with a collection of information if it does not display a currently valid OMB control number.</p> <p><b>PLEASE DO NOT RETURN YOUR FORM TO THE ABOVE ADDRESS.</b></p>					
<b>1. REPORT DATE (DD-MM-YYYY)</b> 21-03-2005		<b>2. REPORT TYPE</b> Master's Thesis		<b>3. DATES COVERED (From – To)</b> Jun 2004 – Mar 2005	
<b>4. TITLE AND SUBTITLE</b>  Feasibility Analysis of a Compton Spectrometer System for Identification of Special Nuclear Material				<b>5a. CONTRACT NUMBER</b>	
				<b>5b. GRANT NUMBER</b>	
				<b>5c. PROGRAM ELEMENT NUMBER</b>	
<b>6. AUTHOR(S)</b>  Schools, Chad C., Major, USA				<b>5d. PROJECT NUMBER</b>	
				<b>5e. TASK NUMBER</b>	
				<b>5f. WORK UNIT NUMBER</b>	
<b>7. PERFORMING ORGANIZATION NAMES(S) AND ADDRESS(S)</b> Air Force Institute of Technology Graduate School of Engineering and Management (AFIT/EN) 2950 Hobson Way WPAFB OH 45433-7765				<b>8. PERFORMING ORGANIZATION REPORT NUMBER</b>  AFIT/GNE/ENP/05-12	
<b>9. SPONSORING/MONITORING AGENCY NAME(S) AND ADDRESS(ES)</b> DTRA/TDND (Bob Kolterman)      AFTAC/TMAT (Capt Ty Miller) 8725 John J. Kingman Rd      1030 S. HWY A1A Ft. Belvoir, VA 22060-6201      Patrick AFB, FL 32925-3002				<b>10. SPONSOR/MONITOR'S ACRONYM(S)</b>	
				<b>11. SPONSOR/MONITOR'S REPORT NUMBER(S)</b>	
<b>12. DISTRIBUTION/AVAILABILITY STATEMENT</b> APPROVED FOR PUBLIC RELEASE; DISTRIBUTION UNLIMITED.					
<b>13. SUPPLEMENTARY NOTES</b>					
<b>14. ABSTRACT</b> <p>Current operational needs require the deployment of radiation detection equipment with the ability to accurately and reliably identify special nuclear materials and their byproducts without dependence on cryogenics. This requires a resolution of 0.5% or less over a range of 200 to 700 keV. The feasibility of a Compton spectrometer to achieve this resolution is examined.</p> <p>The Compton spectrometer system used consists of two detectors. The Compton scatter event occurs in a CdTe detector where the Compton electron energy is collected. Gamma rays scattered out of the CdTe at an angle determined by a conical collimator, are collected in a NaI(Tl) detector. Coincidence electronics determine correlated events and allow the Compton electron and scattered gamma ray energy spectra to be collected.</p> <p>Experimental and modeling techniques are used to evaluate the system's resolution and efficiency and provided reasonable agreement. Expected experimental results based on previous work were not reproduced and the source of the difference remains unknown. Results suggested strict requirements of collimation will make some low areal count rate applications impossible.</p>					
<b>15. SUBJECT TERMS</b> Gamma Ray Spectroscopy, Nuclear Radiation Detection, Special Nuclear Material, Compton Scattering, Cadmium Telluride, CdTe, Compton Spectrometer					
<b>16. SECURITY CLASSIFICATION OF:</b>			<b>17. LIMITATION OF ABSTRACT</b>  UU	<b>18. NUMBER OF PAGES</b>  147	<b>19a. NAME OF RESPONSIBLE PERSON</b> Larry W. Burggraf, PhD, (ENP)
<b>REPORT</b> U	<b>ABSTRACT</b> U	<b>c. THIS PAGE</b> U			<b>19b. TELEPHONE NUMBER (Include area code)</b> (937) 255-6565, ext 4507; e-mail: Larry.Burggraf@afit.edu